UNIVERSITÀ DEGLI STUDI DI ROMA TOR VERGATA
MACROAREA DI SCIENZE MATEMATICHE, FISICHE E NATURALI

MASTER'S DEGREE IN PHYSICS

Curriculum in Astrophysics and Space Science

TITLE
The evolution of the Main Sequence of star-forming galaxies from JWST deep fields

Supervisor:
Prof. Francesco Tombesi

Candidate:
Matricola: 0344031
Bozhidara Nikolova Stoyanova

Co-Supervisors:
Dr. Paola Santini
Prof. Médéric Boquien

Anno Accademico 2024/2025

MASTER IN ASTROPHYSICS AND SPACE SCIENCE

Erasmus Mundus Master
in Astrophysics and Space Science

Master Thesis

The evolution of the Main Sequence of star-forming galaxies from JWST deep fields

Supervisors

Dr. Paola Santini
INAF Osservatorio di Roma

Prof. Médéric Boquien
Université Cote d'Azur

Prof. Francesco Tombessi
Tor Vergata University of Rome

Author

Bozhidara Stoyanova

Academic Year 2024/2025

TOR VERGATA UNIVERSITÀ DEGLI STUDI DI ROMA · UNIVERSITY OF BELGRADE · University of Bremen · UNIVERSITÉ CÔTE D'AZUR · Co-funded by the European Union

This Master thesis is submitted in partial fulfillment of the requirements for the degree Laurea Magistrale in Fisica / Master in Physics, Curriculum ErasmusMundus MASS as part of a multiple degree awarded in the framework of the Erasmus Mundus Joint Master in Astrophysics and Space Science −− MASS jointly delivered by a Consortium of four Universities: Tor Vergata University of Rome, University of Belgrade, University of Bremen, and Université Cote d'Azur, regulated by the MASS Consortium Agreement and Co-funded by the EU under the call ERASMUS-EDU-2021-PEX-EMJM-MOB.

Contents

1 Introduction **1**
- 1.1 Basics of galaxy formation . . . 1
- 1.2 Star Formation . . . 2
  - 1.2.1 Star formation tracers . . . 3
- 1.3 The cosmic Star Formation Rate Density . . . 3
- 1.4 The Star-Forming Main Sequence . . . 5
  - 1.4.1 Parameterizations of the SFMS . . . 7
- 1.5 AGN-galaxy co-evolution . . . 8
- 1.6 Little Red Dots . . . 8
- 1.7 The James Webb Space Telescope (JWST) . . . 9

2 Spectral Energy Distribution modeling **11**
- 2.1 Basics of SED fitting . . . 11
- 2.2 Components . . . 11
  - 2.2.1 Stars . . . 12
    - Star formation History (SFH) . . . 12
    - Initial Mass Function (IMF) . . . 15
    - Stellar Population Synthesis models . . . 15
  - 2.2.2 Nebular emission . . . 17
  - 2.2.3 Dust . . . 17
  - 2.2.4 AGN . . . 17
- 2.3 Fitting methods . . . 18
- 2.4 Code Investigating GALaxy Emission (CIGALE) . . . 19

3 Data and Methods **22**
- 3.1 Dataset . . . 22
- 3.2 Sample selection . . . 23
  - 3.2.1 Detection completeness limits . . . 23
  - 3.2.2 Finding reliable photometric redshifts . . . 23
  - 3.2.3 The final sample . . . 26
- 3.3 SED fitting of our sample . . . 27
  - 3.3.1 Star Formation History assumptions . . . 27
  - 3.3.2 Stellar population . . . 29
  - 3.3.3 Nebular emission . . . 29
  - 3.3.4 Dust attenuation . . . 29
  - 3.3.5 Fitting the AGN component . . . 29
- 3.4 Mass completeness . . . 30
- 3.5 Fitting the SFMS . . . 32
  - 3.5.1 Fitting in redshift bins . . . 32
  - 3.5.2 Time dependent fit . . . 33

4 Results **34**
4.1 Impact of Star Formation History assumptions 34
4.2 The SFMS in the seven different fields 37
4.3 The MS for the whole sample 40
4.3.1 Fits in redshift bins 40
4.3.2 Time dependent fit of the MS 40
4.4 Fitting the AGN 43

Conclusions **47**

Bibliography **49**

Acknowledgments **57**

A Different SFH modules in the JADES-GS field **58**

B Direct comparisons between SFR and $M_\star$ with different SFH **60**

C The SFMS in each field **66**

Abstract

This thesis investigates the redshift evolution of the star-forming main sequence (SFMS) from $z = 4$ to $z = 12$ using deep field observations from JWST and HST. Physical properties of a sample of 12 514 galaxies across seven fields were derived through spectral energy distribution (SED) fitting with the CIGALE code, enabling a systematic analysis of how different assumptions on star formation histories (SFHs) affect the inferred SFMS. Four SFH models were tested, with results showing that the choice of SFH primarily impacts the slope of the SFMS, while the intercept and scatter remain consistent within uncertainties. The slope displays a modest evolution, increasing slightly from $z \sim 4$ to $z \sim 5 - 6$, and then settles to a value around unity. Field-by-field fits and combined-sample analyses were performed. A preliminary investigation into the position of active galactic nuclei (AGN) within the SFR–$M_\star$ relation yielded inconclusive results, highlighting the need for more robust fitting methods and improved datasets. Overall, this work provides new constraints on the high-redshift SFMS and demonstrates the sensitivity of its derived parameters to SFH modeling assumptions.

Chapter 1

Introduction

The first time an object was confirmed to be extragalactic was exactly a century ago in 1925 when Edwin Hubble published his estimates of the distance to NGC 6822 (Hubble, 1925). Those estimates were based on the newly discovered at the time relationship between the luminosity and period of Cepheid variables discovered by Leavitt and Pickering (1912) and refined and published by Shapley (1918).

In this fairly short period of 100 years the field of extragalactic astrophysics has developed at an impeccable pace going hand in hand with the huge advancements in instrumentation (e.g. the first space telescopes, adaptive optics, etc.). The latest generation of instrumentation specifically attuned to study galaxies (e.g. HST over the past few decades and recently JWST) has been allowing us to probe parts of the universe that were previously unreachable.

This thesis is focused precisely on this – studying the most distant corners of the universe with data from state-of-the-art instrumentation. I this thesis I explore the relationship between two physical galaxy properties – the stellar mass and the star formation rate – and how it evolves through cosmic time from JWST deep fields.

In this chapter I will present an overview of the topic at hand starting from the basics of galaxy formation, the cosmic star formation rate density, the star-forming main sequence, and the AGN-galaxy co-evolution. In Chapter 2 I present an overview of the SED fitting technique, in Chapter 3 I present the dataset used and the methodology of this work, in Chapter 4 I present my results, and I summarize this work and present my conclusions in Chapter Conclusions.

1.1 Basics of galaxy formation

Currently the ΛCDM model is the most widely recognized and accepted cosmological model. In this thesis I will not go into details on it but I will go over a short and qualitative description of galaxy formation in this framework. The following subsection is based on the text by Mo, Bosch, and White (2010).

Currently, the most widely accepted theories of structure formation revolve around a very intuitive idea, broadly speaking:

1. After the Big Bang there are quantum fluctuations that we observe in the cosmic microwave background.

2. These small fluctuations give rise to over-dense regions that start gravitationally growing and eventually collapsing. Here is a good point to mention that dark and baryonic matter collapse differently, as dark matter is not collisional and it collapses to form a dark matter halo. Baryonic matter is however collisional, meaning that as it collapses it experiences friction and shocks, heating up to virial temperatures.

3. Hot gas cannot form galaxies yet, which is why gas cooling processes are incredibly important for this stage. There are multiple gas cooling processes that can be relevant here, depending on the size of the halo (different virial temperatures) – bremsstrahlung from free electrons, different excitation and de-excitation processes that also depend on the chemical composition, etc. Generally speaking, the gas cooling stage leads to the segregation of the dark and baryonic matter, as the gas accretes to the central region of the dark matter halo.

4. Typically halos have a small angular momentum at this stage, which leads the gas to settle in the shape of a disc. This is how the first disc galaxies are formed.

5. The gas can now collapse under its own gravity, continue cooling, and eventually starts fragmenting and forming stars.

This is a very brief overview of how an individual, disc galaxy can form but what about the rest? Galaxies do not evolve in a vacuum separated from one another but indeed interact quite often. The first galaxies are assumed to have been small as spatially smaller over-densities are observed to have higher amplitudes meaning that small dark matter halos are easier to form in the very early universe. From then on, however, they start merging with each other and progressively growing. This is called the bottom-up (or hierarchal) scenario of galaxy formation and evolution and is currently the most widely accepted one. Merger events can then explain the formation of elliptical galaxies as well as disc galaxies with bulges.

1.2 Star Formation

Star formation is the process of turning gas into stars in galaxies and is the main focus of this thesis. It is one of the main processes shaping galaxies and is absolutely crucial to our understanding of galaxy evolution.

As briefly mentioned in the previous section, star formation can occur in the presence of cold, dense gas, mainly in Giant Molecular Clouds (GMCs). The star formation can, however, be impacted by various other processes both positively and negatively. For example the energy released by a supernova explosion can heat up the surrounding gas, temporarily slowing down the star formation (Supernova feedback). Some processes can fully quench the star formation of a source such as quasar-mode AGN feedback (Kormendy and Ho, 2013) in which galaxy is stripped from its available gas reservoir or strangulation in which the supply of cold gas to the galaxy is halted (Peng, Maiolino, and Cochrane, 2015). Some processes can also have positive impact of the SFR, for example merger events can onset star burst episodes.

Since stars form in GMCs, that contain gas but also dust, one issue in observing the star formation of galaxies arises. Star formation is often obscured by the dust in a galaxy since dust grains absorb more in the UV light, obscuring mostly the young, bright stellar populations.

1.2.1 Star formation tracers

There are multiple, often complimentary, ways to measure the ongoing star formation rate (SFR) of a galaxy and here I will discuss some of them with their main features.

- **Rest-frame ultraviolet light** – The UV continuum of a galaxy is a very direct measure of the ongoing star formation as it is dominated by the emission from O and B type stars. Those types of stars have very short main-sequence lifetimes ($\sim$ tens of Myrs) meaning that probing their population is a direct probe of the recent star formation of a galaxy. Converting the UV luminosity of a source to a star formation rate is usually done through conversion factors that depend on the assumed initial mass function stellar, population model and metallicity (Madau and Dickinson, 2014).

- **Rest-frame infrared light** – One concern about using only UV tracers is the problem of dust obscuration. Stars form in GMCs of gas and dust and dust has a property of absorbing UV light and re-emitting it in the IR part of the spectrum. This poses an issue as star formation can be heavily obscured depending on the dust content of a galaxy but it also means that measuring the rest-frame IR emission can probe ongoing star formation. A conversion factor can be estimated as for the UV (Madau and Dickinson, 2014). Some issues with this tracer are the complexity of IR measurements and that it overlooks the unobscured SFR, providing an underestimate for it. For this reason often both UV and IR tracers are used in a composite manner to estimate the total SFR of a source.

- **Hα** – This indicator, much like the previous two, probes the population of very massive, luminous stars that have short main-sequence lives. It is an important estimator as it works on a shorter timescale compared to the UV and IR tracers ($\sim$ 10 Myrs) (Clarke et al., 2024). An issue in this case is the required observational time for spectroscopic measurements.

- **Spectral Energy Distribution (SED) fitting** – SED fitting is not a direct SFR indicator but rather a technique to estimate various physical properties from the given data, including the SFR. This is the method used to infer SFRs in this thesis and is described in detail in Chapter 2.

1.3 The cosmic Star Formation Rate Density

The star formation rate per unit volume (Star Formation Rate Density, or SFRD) and its evolution through cosmic time has been extensively studied as it provides important information for galaxy evolution models and describes the evolution of galaxies through cosmic times. It is a key component in constraining models describing many processes related to star formation and galaxy growth – gas cooling and accretion, merger events, black hole-galaxy co-evolution, feedback

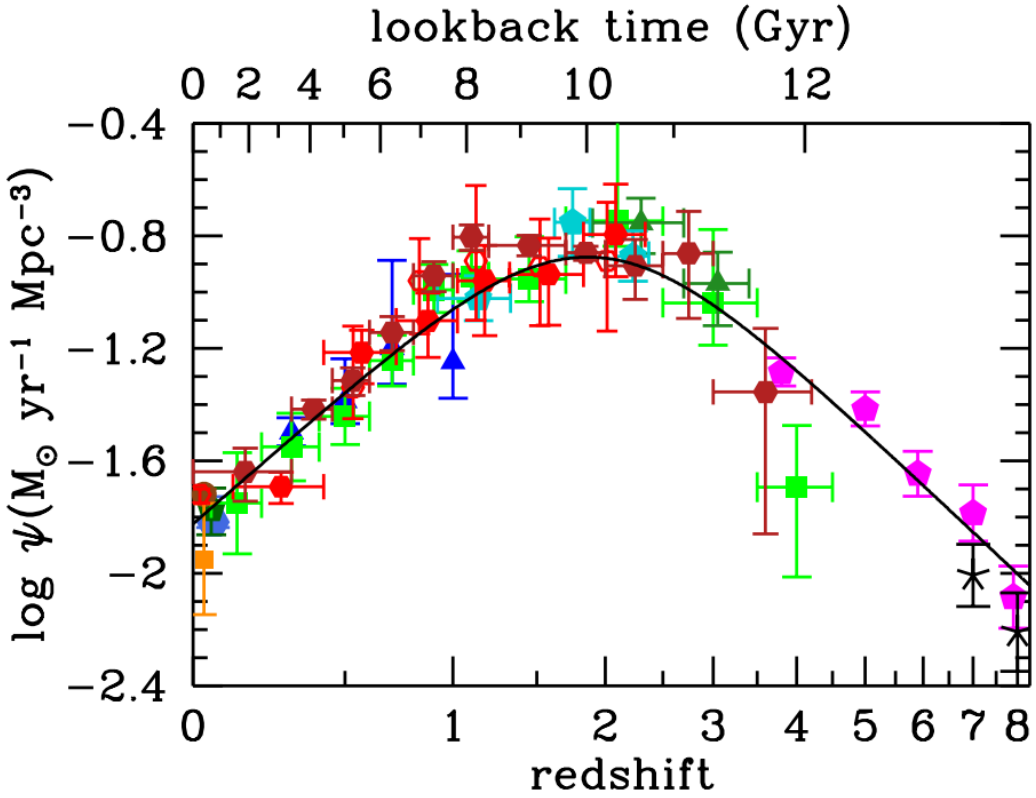

Figure 1.1: The evolution of the SFRD with redshift from multiple studies and using different SFR indicators (see Madau and Dickinson, 2014, and references therein). The figure is the left panel from Figure 9 in Madau and Dickinson (2014)

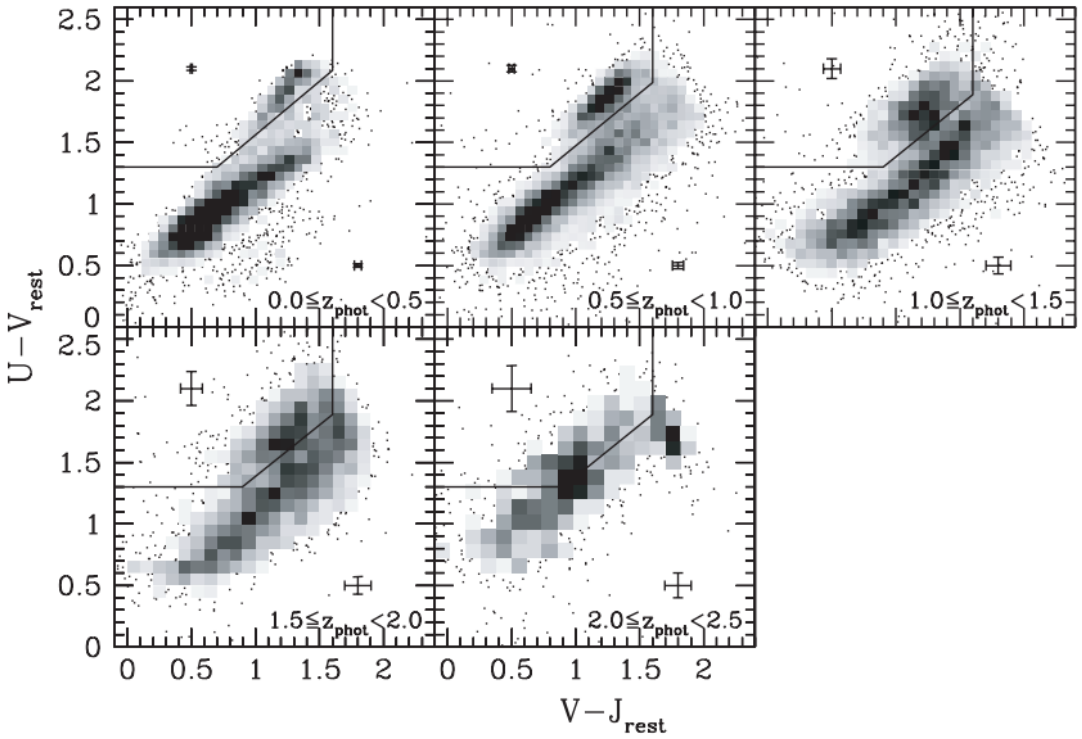

Figure 1.2: Rest-frame U-V vs. V-J colors for a large sample of galaxies. This is Figure. from Williams et al. (2009)

processes, etc. One of the most influential works on the topic is the review by Madau and Dickinson (2014). They combine data from multiple UV and IR studies to build an extensive picture of the evolution of the SFRD and obtain one of the lines in the plot shown in Figure 1.1. There we can clearly see that the SFRD in the universe peaked at $z \sim 2$. This period in the history of the universe is known as "Cosmic noon". The figure also includes results from multiple other studies and was taken from a more recent paper by Katsianis et al. (2016).

The main contributor to the high SFRD at cosmic noon are known to be galaxies lying on a tight SFR-$M_\star$ relation (Rodighiero et al., 2011; Rodighiero et al., 2015), discussed in the next section. In Madau and Dickinson (2014) the authors conclude that the smooth evolution of the SFRD implies that the evolution of the cosmic SFH is mainly driven by the balance between gas accretion and feedback rather than stochastic processes such as mergers.

1.4 The Star-Forming Main Sequence

In color-color diagrams of large samples of galaxies, two distinct groups of objects can be seen, as shown in Figure. 1.2 (Labbe et al., 2005; Wuyts et al., 2007; Williams et al., 2009).

After studying the physical properties of these two groups it becomes apparent that they also occupy two distinct regions on a SFR-$M_\star$ diagram. The relationship followed by the larger of the two groups (the star forming galaxies) was named "the main sequence" by Noeske et al. (2007) and has been extensively studied (e.g.

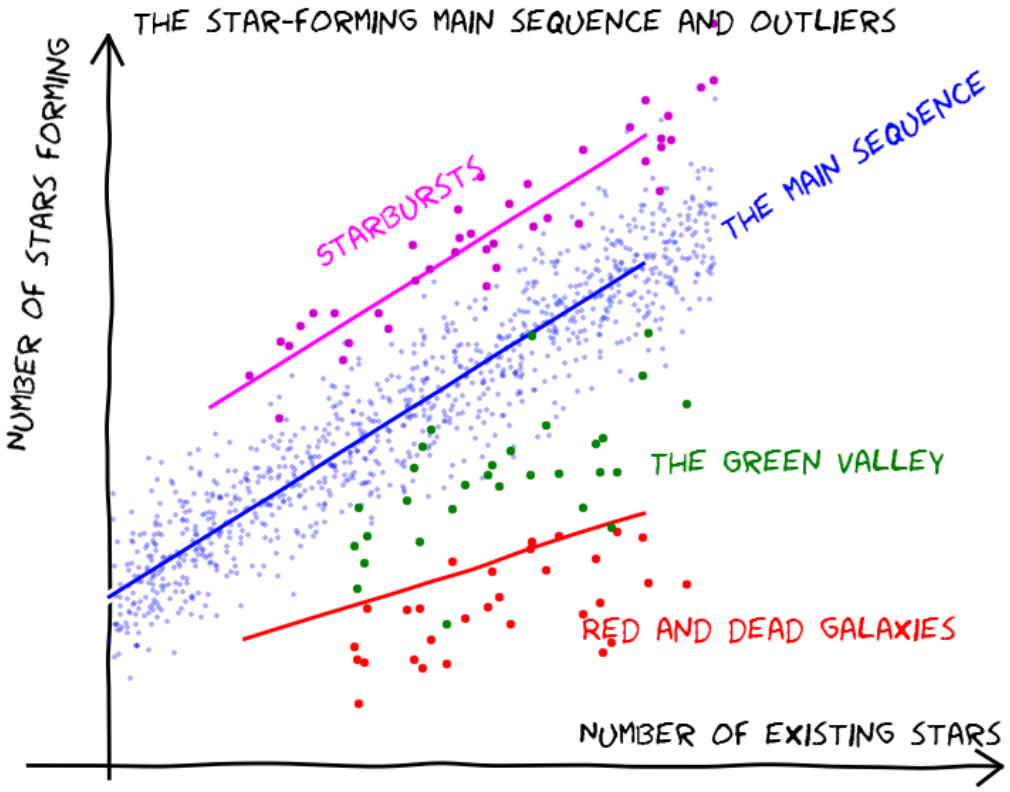

Figure 1.3: An illustration explaining SFR-$M_\star$ diagrams and the SFMS. Posted by Harry Ferguson on the CANDELS blog.

Brinchmann et al., 2004; Elbaz et al., 2007; Daddi et al., 2007; Speagle et al., 2014; Santini et al., 2017; Popesso et al., 2023; Clarke et al., 2024; Cole et al., 2025).

Broadly on such a diagram we can distinguish four types of objects as follows:

- Most galaxies lye around a line in log-space, called the Star Forming Main Sequence (SFMS). These galaxies appear blue, are usually spiral, and show moderate amounts of current star formation.
- Distinctly bellow this star-forming strip there are the red, quiescent, usually elliptical galaxies that exhibit little to no star formation.
- In between the previous two groups there is an underpopulated region called "The Green Valley" where interestingly enough the Milky Way and Andromeda are situated.
- Galaxies substantially above the SFMS are the so called Starburst (SB) galaxies that exhibit an episode of a very high SFR, usually merger induced.

Locally, the first two groups are the largest and most prevalent. With increasing the redshift red and passive galaxies become rarer. An illustration with these types of galaxies and their positions on the SFR-$M_\star$ diagram is shown in Figure. 1.3 and an example of the SFMS fit at different redshifts from literature is shown in Figure 1.4.

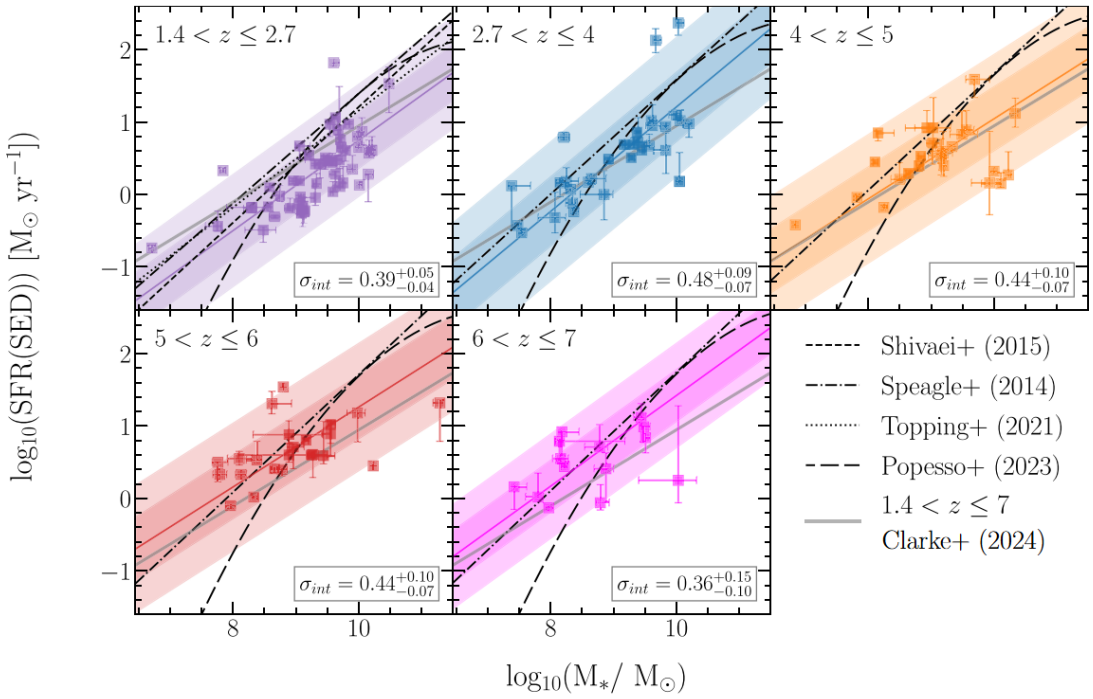

Figure 1.4: The SFMS with SFR inferred from SED fitting in redshift bins. Adapted from Clarke et al. (2024). Includes the SFMS from Shivaei et al. (2015), Speagle et al. (2014), Topping et al. (2021), and Popesso et al. (2023).

The relationship is known to evolve with redshift as well, raising the question of its form in SFR-M$_\star$-z space.

The SFMS is one of the most fundamental observables in the field of galaxy evolution as it directly probes the relationship between two very fundamental physical parameters and the two sides of the same process – turning cold gas into stars. SFR is a parameter describing the current rate at which this process is happening while the stellar mass is the direct result of the integrated SFR throughout the history of any given galaxy. The normalization of the SFMS is known to rise with redshift which is related to higher accretion rates in the early universe, while the slope has been shown to stay somewhat stable (Santini et al., 2017). The scatter of the SFMS is another parameter that is very interesting to study as its low value ($\sigma \sim 0.25-0.4$) suggests that star-forming galaxies follow a similar path in their star-formation history (Santini et al., 2017, and references therein). The evolution with redshift of the (intrinsic) scatter is a probe into the stochasticity of star-formation histories at different redshifts.

1.4.1 Parameterizations of the SFMS

There are multiple ways to parametrize the SFMS where the most common one is a straight line in log-log space (or a power law) as this is a straightforward and very effective way to fit the data that still produces a tight relationship with $\sigma \sim 0.3$.

$$\log[\mathrm{SFR}] = \alpha \times \log[M_\star] + \beta, \tag{1.1}$$

where α is the slope of the SFMS and β is the intercept, that is commonly evaluated at the median stellar mass for the sample. This parametrization has been widely

used in literature alongside variations of it that include the intrinsic scatter as a fit parameter as well (e.g. Santini et al., 2017; Clarke et al., 2024; Cole et al., 2025).

At high stellar masses ($10^{10} - 10^{11}$ $M_{\odot}$), however, the SFMS has been observed to have a turnover at some characteristic stellar mass. This mass increases with redshift and the SFMS flattens to a lesser extent (Lee et al., 2015; Tomczak et al., 2016; Whitaker et al., 2014; Schreiber et al., 2017). There are parametrization that try to account for this using different approaches, e.g. one early approach was to fit a broken power law to the data effectively fitting the low and high mass regions separately (Whitaker et al., 2014). Other approaches include fitting polynomial functions in redshift bins, fitting a function in SFR-$M_{\star}$-z space and others (Magnelli et al., 2014; Schreiber et al., 2017; Speagle et al., 2014; Popesso et al., 2023).

One possible parametrization is that used in Equations 10 in Popesso et al. (2023):

$$\log[\mathrm{SFR}] = (a_1 t + b_1)\log[M_{\star}] + b_2 \left(\log[M_{\star}]\right)^2 + (b_0 + a_0 t), \tag{1.2}$$

where t is the cosmic time and is related to the redshift through the cosmological parameters and a_1, b_1, b_2, b_0, a_0 are free parameters of the fit.

1.5 AGN-galaxy co-evolution

Active Galactic Nuclei (AGN) originate their observed luminosity from an accreting the super massive lack hole (SMBH) in the center of the galaxy. It has been established that SMBHs and their host galaxies co-evolve, specifically through observing multiple tight correlations between properties of the galaxy and the SMBH, the tightest of which is the $M_{BH} - \sigma$ relationship (Kormendy and Ho, 2013; Mountrichas, 2023), where M_{BH} is the black hole mass and σ is the velocity dispersion of stars in the galaxy bulge. One piece of evidence for the co-evolution of black holes and their host galaxies is the similarity in the growth history of black holes and the evolution of the SFRD, discussed in Madau and Dickinson (2014).

AGN feedback is one of the main ways an AGN and its host galaxy co-evolve. AGN feedback is specifically related to regulating star formation processes in massive galaxies and especially at high redshifts. There are two main regimes in which AGN feedback can quench star formation (or help maintain an already quiescent galaxy in that same state). Quasar-mode feedback is a process in which an AGN emits a large amount of energy, either radiatively or mechanically, that can strip the host galaxy of its gas reservoir and rapidly quench star formation. Maintenance-mode AGN feedback is when the energy emitted from the AGN does not strip the host of its gas but it maintains the gas hot, preventing it from collapsing and forming stars (Kormendy and Ho, 2013). This directly relates AGN activity to the star formation history of a galaxy.

1.6 Little Red Dots

Little Red Dots (LRDs) are a completely new class of objects discovered in the first JWST data (e.g. Labbé et al., 2023; Kocevski et al., 2023; Harikane et al., 2023).

Their name was given by Matthee et al. (2024) and their properties have been puzzling astrophysicist in the last couple of years. These objects, as their name implies, look red in color and are quite compact. They are more common at very high redshifts with their number density increasing at $z < 8$ and dropping bellow $z = 4$ (Kocevski et al., 2025a).

Another key observational characteristic of these objects is their V-shaped spectrum, blue in the UV and red in the optical parts of the spectrum. Initially, they were suspected to be AGN, as they exhibit broad Balmer lines. The AGN hypothesis can also explain their optical red colors but it struggles with the lack of X-ray emission in most LRDs. Only two of them have been identified to show X-ray emission, confirming the presence of AGN activity (Kocevski et al., 2025b). They have been hypothesized to be AGN in their very first stages of growth (Inayoshi, 2025).

Currently a few other hypotheses of the the nature of these objects are also being discussed, one of them being the hypothesis that they are supermassive Population III stars at a late stage in their evolution (Nandal and Loeb, 2025). Population III stars are a hypothesized population of very early stellar objects with virtually no metallicity, and potential progenitors of supermassive black holes.

Other, more extravagant, hypothesis also have been proposed such as quasi-stars – objects having a black hole as a core and a gaseous envelope surrounding it (Begelman and Dexter, 2025). In any case, those objects are still quite mysterious and hard to model and fit as their nature is still unclear.

1.7 The James Webb Space Telescope (JWST)

All data used in this thesis was obtained with the Hubble Space Telescope (HST) or the JWST, specifically with the NIRCam instrument. In this section I will present a summary on why the JWST data in particular is incredibly pivotal to all studies of high redshift galaxies.

The JWST has two main advantages compared to any space based instrument seen before – it has a much larger mirror than Spitzer (previous generation IR space telescope that was deactivated in 2020 (Werner et al., 2004)) and it is an infrared telescope unlike the HST. This is crucial for studying high redshift galaxies, e.g the 4000 Åbreak (a result of closely spaced metal absorption lines), is observed up to $z \sim 10$ in NIRCam. In Figure 1.5 a plot of the transmission curves of all filters used in this work – HST and JWST– is shown. The wavelength range covered by the NIRCam instrument is 0.6 - 6 µm (Rieke et al., 2023). On the other considerable advantage, JWST has a 6.6 m in diameter mirror while Spitzer had a mirror with a diameter of only 85 cm. This makes the light collecting area of JWST drastically larger, making it much more sensitive to faint sources.

This is to say that the JWST is allowing us to probe the rest-frame optical emission of faint sources at very high redshifts allowing us to reliably measure their stellar masses and therefore study the star-forming main sequence at such early stages of the universe for the first time.

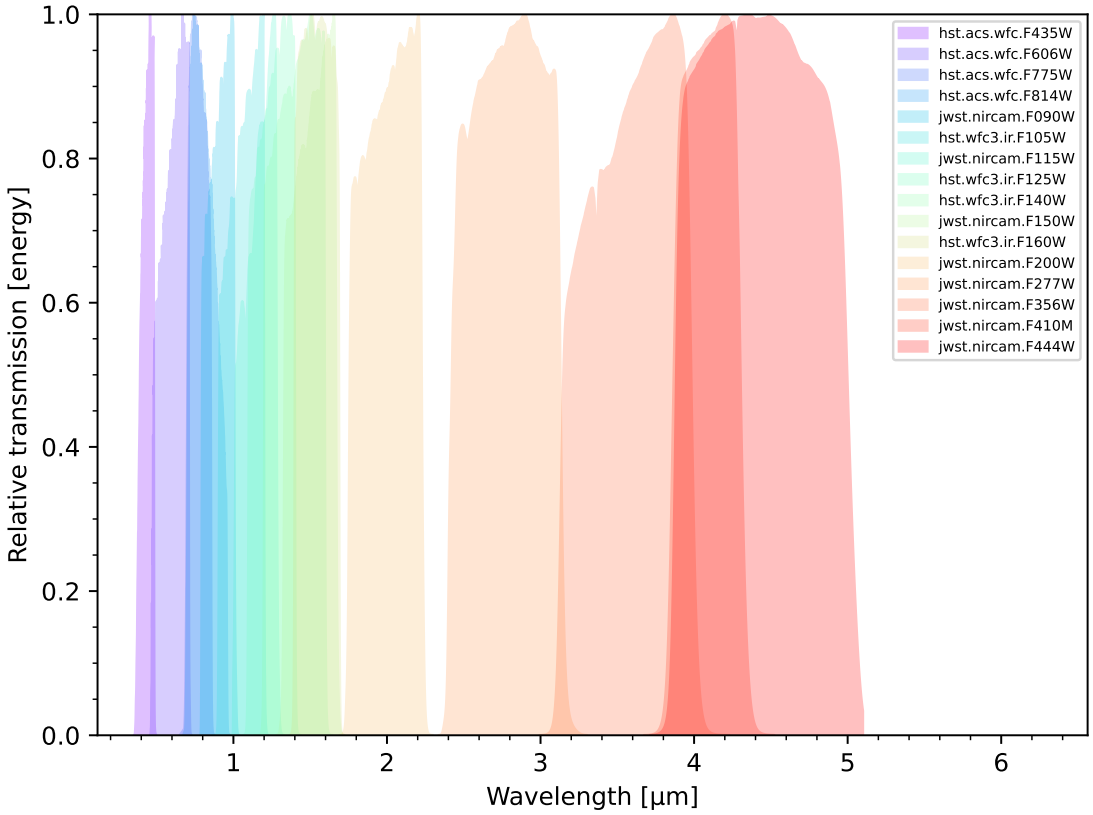

Figure 1.5: Plot of the transmission curves of all filters used in this work from both HST and JWST. The plot was generated using CIGALE.

Chapter 2

Spectral Energy Distribution modeling

In this chapter I present the technique of Spectral Energy Distribution (SED) modeling. First, I will go through the basic ideas behind it, then through the different components and models that make up the full SED of a galaxy, and lastly through the workings of the specific software I used for this work.

2.1 Basics of SED fitting

The Spectral Energy Distribution (SED) of a galaxy is shows the flux per unit wavelength (or frequency) as a function of the wavelength. SED fitting is a powerful method for deriving the physical properties of galaxies, especially at high redshifts where obtaining spectroscopic data for large datasets over a broad range of wavelength is expensive and time consuming. The basic principle SED fitting relays on is that the different physical properties of a galaxy leave a mark in its detailed spectrum. This means that, in principle, if we have the full SED of a galaxy we can infer all of its physical properties. SED fitting is the an attempt to model the full SED of a source to reproduce its observed emission based on whatever information we have – whether it is a few photometric points or a more sophisticated spectrophotometric dataset. In this way multiple physical properties can be constrained.

2.2 Components

SEDs are complex and involve contributions from the various components of a galaxy. This makes modelling them a complicated procedure. A diagram of the SED of a typical galaxy in a broad rest-frame wavelength range is shown in Figure 2.1. The contributions of the main components is clearly shown giving insight into which components dominate in different wavelength ranges.

In this section I will discuss the main components - stars, gas, dust, and, in some cases, AGN.

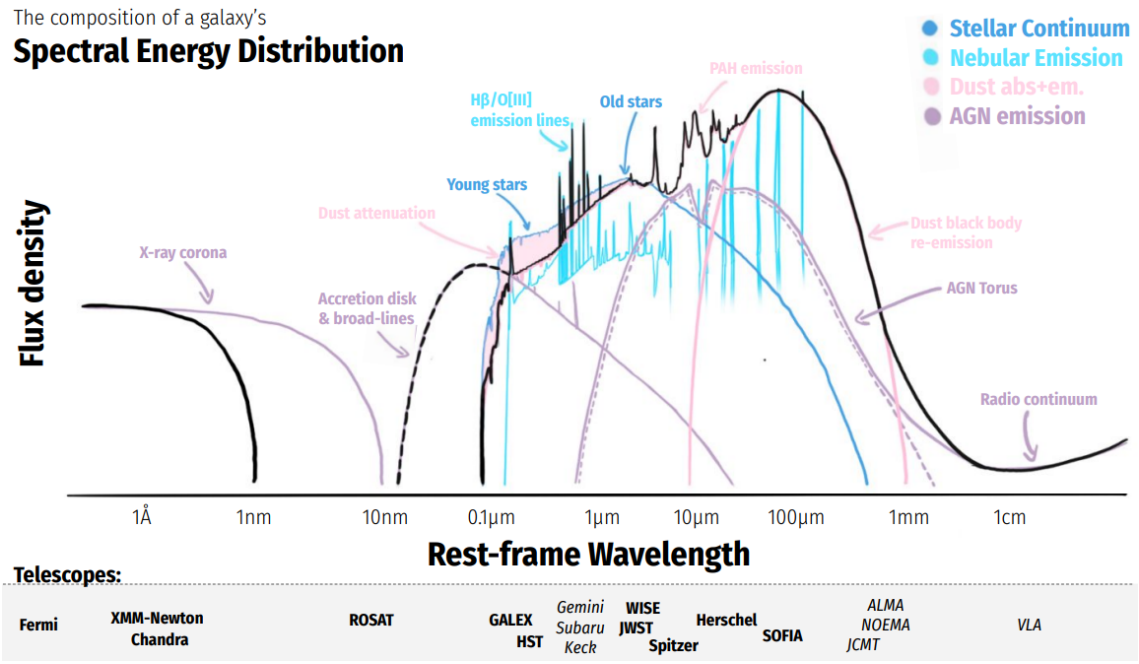

Figure 2.1: Figure 2 from Iyer et al. (2025). A diagram of the pan-chromatic SED of a galaxy and its main components.

2.2.1 Stars

Stars are the main contributors to the optical, UV and NIR SED of a galaxy. Accurately modelling their combined spectra is of utmost importance and is not an easy feat. This is done in a few different steps. First is modelling the Single Stellar Population (SSP) that describes the contributions of a single population of stars of the same age and metallicity. The SSP itself is dependent on a few key assumptions such as the initial mass function (IMF), the metallicity and the age of the population. This interplay between the various aspects of the SSP is described by the equation:

$$f_{\lambda}^{SSP}(t, Z) = \int_{M_{\min}}^{M_{\max}} \phi(m) f_{\lambda}(m, t, Z)\, dm, \tag{2.1}$$

where $\phi(m)$ is the IMF, i.e. the mass distribution of stars at birth, $f_{\lambda}(m, t, Z)$ is the stellar spectrum of a star of a given mass, age, and metallicity.

To construct the Composite Stellar Populations (CSP) that is also weighted by the Star Formation History (SFH) the following equation is used:

$$f_{\lambda}^{gal}(t, Z) = \int_{0}^{t} f_{\lambda}^{SSP}(t - t', Z)\, SFH(t')\, dt'. \tag{2.2}$$

In the following subsections I will discuss more in detail the building blocks of the combined stellar SED of a galaxy.

Star formation History (SFH)

The first component that I will discuss is the Star Formation History (SFH) of a galaxy. The SFH is simply the amount of stars formed per year as a function of time. That is an essential component in SED modeling as stellar spectra change with their age making understanding the age of the different stellar populations in

a galaxy vital for its SED.

There are two main types of SFH models - parametric and non-parametric. Both of these broad categories have a few widely used variations. The following list is a (non exhaustive) review of the most common ones, with an emphasis on the ones used for this work.

- **Parametric models** are models that describe the SFH of a galaxy by some analytic function, easily parametrized by an equation and a few parameters. These models are approximations and can be quite unrealistic but are straightforward and not computationally demanding.
  - **Exponentially declining (τ-models)** - These models provide the simplest and very widely used way to parametrize a galaxy's SFH. They assume that the SFR of a galaxy starts from a maximum value at some time T_0 and from then onward it exponentially declines with a timescale τ_0. These models are, however, especially unreliable at high redshifts due to the lack of a rising SFR phase.

$$\mathrm{SFR}(t) \propto \begin{cases} e^{-\frac{t-T_0}{\tau}}, & t > T_0 \\ 0, & t < T_0. \end{cases} \tag{2.3}$$

  - **Delayed exponential** - These are some of the models used in this work. They are very similar to the τ-models but in them a rising SFR stage is introduced by multiplying the expression for $\mathrm{SFR}(t)$ with the time since star formation started (in this case T_0 is not the time at maximum SFR). This simple modification creates much more realistic models where there is a rising SFR phase in the galaxy's SFH, followed by an exponential decline.

$$\mathrm{SFR}_{\mathrm{delayed}}(t) \propto \begin{cases} (t - T_0)e^{-\frac{t-T_0}{\tau}}, & t > T_0 \\ 0, & t < T_0. \end{cases} \tag{2.4}$$

    - **Delayed exponential + constant burst or quench** (Ciesla, Elbaz, and Fensch, 2017). This is a variation on the delayed exponential that introduces a short phase of a constant burst or quench, described by the parameter r_SFR, in the recent history of the galaxy. This model allows for more flexibility in the SFH while still keeping the number of parameters low.

$$\mathrm{SFR} \propto \begin{cases} \mathrm{SFR}_{\mathrm{delayed}}, & t < t_{\mathrm{burst}} \\ r_{\mathrm{SFR}} \times \mathrm{SFR}(t = t_{\mathrm{burst}}), & t > t_{\mathrm{burst}} \end{cases} \tag{2.5}$$

    - **Delayed exponential + exponential burst.** This is a modification to the delayed exponential model that adds a second component with recent exponentially declining burst in SFR. It is described by the following equation

$$\mathrm{SFR}(t) \propto \begin{cases} \mathrm{SFR}_{\mathrm{delayed}}, & t < t_{\mathrm{burst}} \\ \mathrm{SFR}_{\mathrm{delayed}} + e^{-t/\tau_{\mathrm{burst}}}, & t > t_{\mathrm{burst}} \end{cases} \tag{2.6}$$

      which is then normalized in such a way that a fraction f_{burst} of the total stellar mass of the galaxy is formed during the burst.

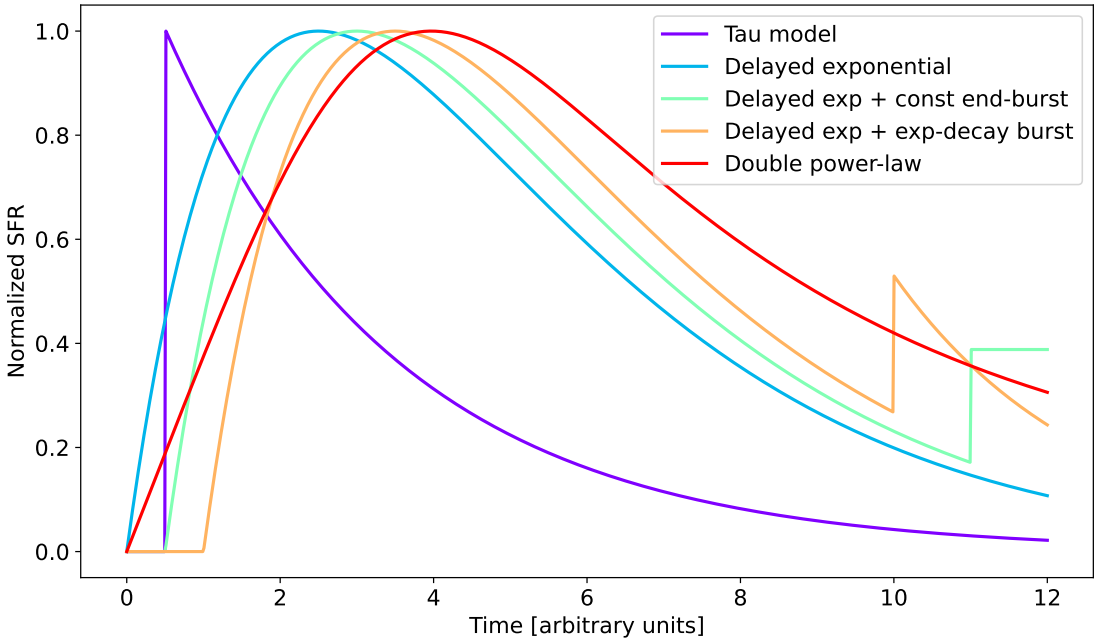

Figure 2.2: A simple comparison of the shapes of the parametric SFHs described in the text. The three delayed exponential SFHs are shifted in time for clarity. Parameters used: τ-model: $\tau = 3$ (Arbitrary units); Delayed exponential: $\tau = 2.5$; Delayed exponential with constant burst/quench: $\tau = 2.5$, $r_{\rm SFR} = 2$; Delayed exponential with exponential declining burst: $\tau = 2.5$. $\tau_{\rm burst} = 2$, $f_{\rm burst} = 0.05$; DPL: $\tau = 5$, $\alpha = 2$, $\beta = 1$.

  - **Double Power-Law** - In these models the two phases (rising SFR and declining SFR) are described by two different power-laws. This introduces one additional parameter.

$$\mathrm{SFR}(t) \propto \left[\left(\frac{t}{\tau}\right)^{\alpha} + \left(\frac{t}{\tau}\right)^{\beta} \right]^{-1} \tag{2.7}$$

  These are only a few examples of the most widely adopted forms of SFH but other more extreme variants exist such as a constant SFH or an exponentially rising model. A diagram showing the differences in the shapes of the different parametric models is shown in Figure. 2.2. For a more detailed review see Carnall et al. (2019b).

- **Non-parametric models** are models that do not parametrize the SFH in some easy way but instead try to mimic the real SFH of a galaxy. These models have been more and more common, especially in the high redshifts, as they are more flexible and more realistic than parametric models, however, they can be more computationally intense. In this type of model the SFR is inferred for a number of time bins that can be spaced differently (e.g flat binning or logarithmic binning). Then the SFR between the bin edges is either assumed to be constant, as in the non-parametric models used in this work, or used to reconstruct a smooth curve (e.g. using Gaussian processes as in Iyer et al. (2019)). Another approach to non-parametric models is to bin the SFH in mass fraction bins: the total mass of the galaxy is split in N equal mass bins and the time for forming each one is then inferred meaning that the time

bins of the model are now flexible. This is the approach in Iyer et al. (2019). Another notable difference can be the choice of priors that govern how the mass (or SFR) is distributed in each time bin (e.g, flat prior, continuity prior, Dirichlet, etc.). For a detailed review see (Leja et al., 2019).

Initial Mass Function (IMF)

The IMF is a function that describes the initial distribution of masses of a co-eval stellar population, and it is an important component of any stellar population model. The IMF is especially important for the low end of the mass distribution of stars as these sources contribute to the stellar mass and SFR of a galaxy but are not directly seen as they are outshined by brighter sources. There are multiple variations of this empirical result and in this subsection I will mention only the most widely used forms.

- **Salpeter IMF** (Salpeter, 1955). This is the first empirically inferred form of the IMF and it is a simple power law:

$$\xi(M) \propto M^{-2.35}, \tag{2.8}$$

  where $\xi(M)$ is the number of stars per stellar mass and M is the stellar mass. This IMF is mostly accurate at intermediate and high masses but over predicts the number of low mass stars.

- **Kroupa IMF** (Kroupa, 2001). This form of the IMF solves the issue of over predicting low mass stars as it introduces a piecewise power-law with a different slope for different mass ranges:

$$\xi(M) \propto \begin{cases} M^{-0.3}, & 0.01 \leq M/M_{\odot} < 0.08 \\ M^{-1.3}, & 0.08 \leq M/M_{\odot} < 0.5 \\ M^{-2.3}, & M/M_{\odot} \geq 0.5 \end{cases} \tag{2.9}$$

- **Chabrier IMF** (Chabrier, 2003). This form of the IMF is still a power-law above $1M_{\odot}$ but at the low end takes a lognormal form.

$$\xi(M) \propto \begin{cases} \frac{1}{M} \exp\left[-\frac{(\log M - \log M_c)^2}{2\sigma^2}\right], & M \leq 1M_{\odot} \\ M^{-2.3}, & M > 1M_{\odot} \end{cases} \tag{2.10}$$

  where $M_C \approx 0.08M_{\odot}$ is the "characteristic mass" where the distribution peaks and $\sigma \approx 0.69$. The described case is for populations of individual stars but Chabrier (2003) provided an expression for populations of binaries where the values for M_C and σ differ.

A comparison of the three described IMFs is shown in Figure. 2.3.

Stellar Population Synthesis models

Stellar population synthesis models are used to generate the SED of a simple stellar population (SSP) – a description of the combined spectra of all stars in a population of a given age and metallicity, distributed in mass according to the IMF. There are different ways to construct such models and here I will shortly present a few of the most widely used ones.

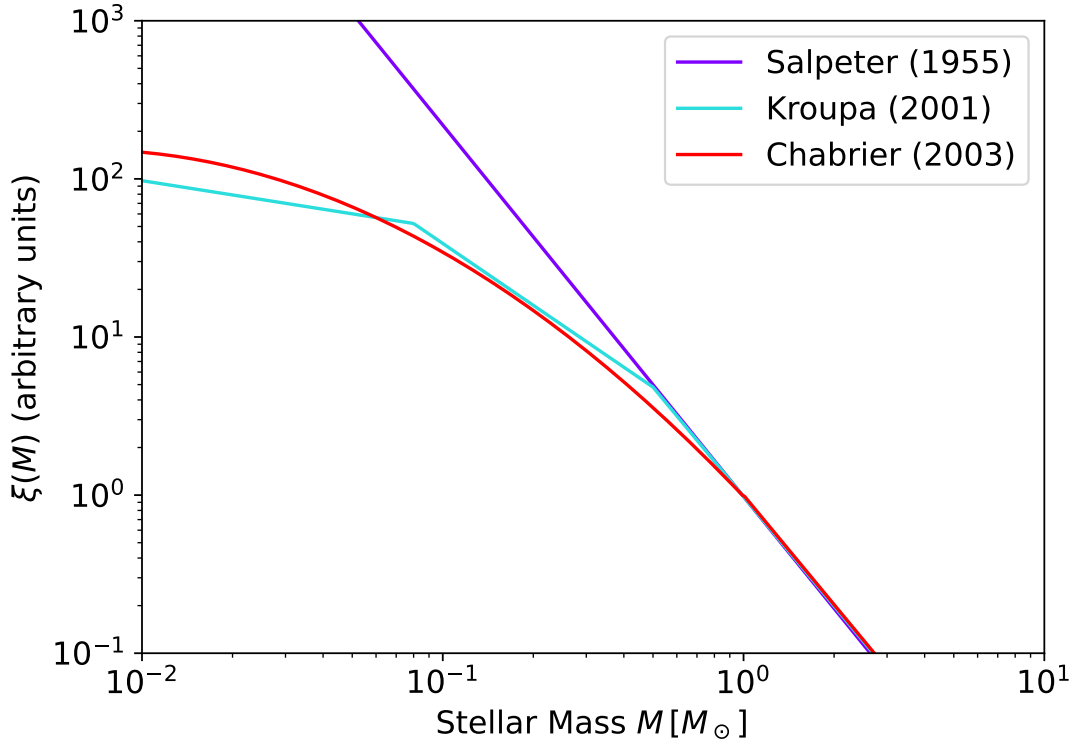

Figure 2.3: A plot representing the major differences between the different IMF shapes. The three presented IMFs have a slightly different slope at high masses but the major deviations between them occur bellow 1 $M_\odot$.

- **The Bruzual and Charlot (2003)** models are often regarded as the standard or baseline models due to their extensive usage in the literature. They provide stellar population spectra over a wide range of ages, from 1×10^5 yr to 2×10^{10} yr, with a high spectral resolution from 320 nm to 950 nm, and at a lower spectral resolution over a broader wavelength range from 9.1 nm to 160 µm. They provide models for 6 metallicities ranging from $Z = 0.0001$ to $Z = 0.05$ and for the IMF of Salpeter (1955) and Chabrier (2003). This broad parameter space makes the models highly versatile for modeling diverse galaxy populations across a wide range of redshifts.

- **The Charlot and Bruzual (2019)** stellar populations are an evolution of the Bruzual and Charlot (2003) models (Gutkin, Charlot, and Bruzual, 2016; Plat et al., 2019; Sánchez et al., 2022). They include updated treatments for hot massive stars and Asymptotic Giant Branch (AGB) stars, along with a much finer metallicity sampling of 15 values, ranging from $Z = 0.0001$ to $Z = 0.06$.

- **The Binary Population and Spectral Synthesis code (BPASS)** (version 2.2) models (Eldridge and Stanway, 2009; Eldridge et al., 2017; Stanway and Eldridge, 2018) are a bigger departure from the other two models as they include the effects of binary evolution. Multiple studies have shown that binary interactions play a significant role across a range of stellar types and environments (Eldridge et al., 2017, and references therein).

2.2.2 Nebular emission

This component is necessary to describe the emission of the ionized gas in a galaxy. Young stars are born in cold gas clouds and are very effective at ionizing the gas in the nebula that surrounds them leading to what we call "nebular emission". This emission is the result of multiple processes – e.g. free-free, free-bound, and two-photon processes lead to a nebular continuum, while the nebular emission lines are a result of various Hydrogen and metal recombination lines.

2.2.3 Dust

The dust content of a galaxy affects their SED heavily as it scatters, absorbs, and re-emits light from stars in a wavelength-dependent way. High dust content makes galaxies redder as the absorption is related to the size of the dust grains and smaller grains, absorbing the radiation at shorter wavelengths, are more common (Iyer et al., 2025). This strong impact implies that improper modelling of the dust component of a source can have serious consequences for the obtained SED, and therefore, physical properties. In particular, the UV radiation from young stars is absorbed and re-emitted into the IR by dust, making it necessary to consider for any SFR estimate. The dust attenuation is commonly described by $A(\lambda)$ which is the difference in magnitudes between the intrinsic flux of a source and the observed flux as a function of wavelength. There are many different attenuation laws describing the wavelength dependence of the dust attenuation. Here we will briefly discuss some common ones.

- **The Calzetti attenuation law** (Calzetti et al., 2000). It is an empirical relation that was developed for low-redshift starburst galaxies but has been widely used for modelling high redshift sources.
- **The Noll et al. (2009) and Salim, Boquien, and Lee (2018)** curves. Often, a modification of the Calzetti attenuation curve can be used. These sorts of curves have a lot more flexibility and most notably introduce an (optional) UV bump (Fitzpatrick, n.d.).
- **The Charlot and Fall attenuation law** (Charlot and Fall, 2000). In this model the light from younger stars are attenuated by both the birth clouds (BC) that surround them and the diffuse ISM of the galaxy. Older stellar populations are attenuated only by the diffuse ISM. These two different attenuation components are both parametrized as power laws – $A(\lambda) \propto \lambda^{\delta}$, where λ is the rest-frame wavelength and δ is the slope.

A comparison of the described attenuation curves is shown in Figure. 2.4.

2.2.4 AGN

When an AGN is present in a galaxy it can have a varying impact from completely dominating the radiation in extreme case such as quasars to being barely detectable amongst the other emission sources in the object at some wavelengths (e.g., obscured or low-luminosity AGN). AGN emission is governed by many different processes and at a vast range of frequencies:

- They have a corona of hot electrons that emits X-ray radiation due to inverse Compton scattering of UV photons from the accretion disk.

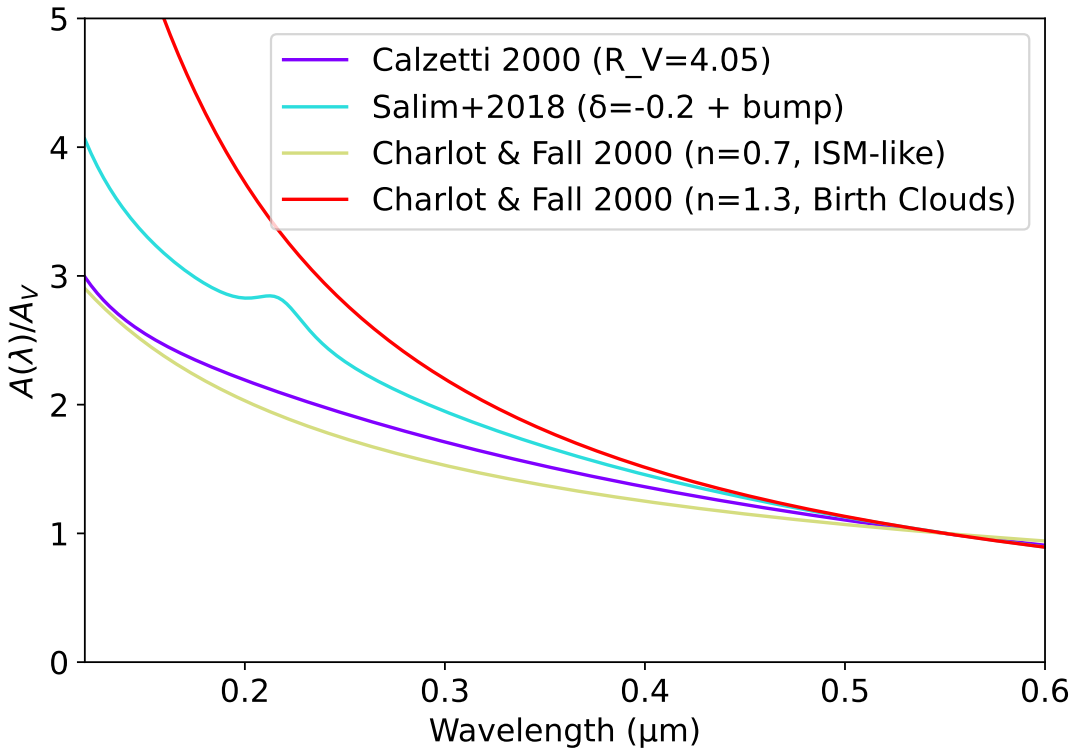

Figure 2.4: A diagram illustrating the different shapes and slopes of the attenuation curves described in the text.

- They emit in UV and optical due to the thermal radiation from their accretion disk. In this regime AGN also exhibit emission lines (both broad and narrow) from the clouds of ionized gas at varying distances from the accretion disc (from ~ 1 pc to hundreds of parsecs).
- In the NIR and MIR regimes the emission is due to the AGN torus. This is a structure made of dust that absorbs and scatters the radiation from the accretion disc.
- In the radio part of the spectrum the AGN emission is mostly the result of synchrotron radiation due to the interaction of relativistic electrons with the AGN's magnetic field. This can be the result of a few different phenomena, most notably radio jets.

For this work the concern was the rest-frame UV and optical AGN emission. It can be modelled by different AGN models e.g. Fritz, Franceschini, and Hatziminaoglou (2006) and Stalevski et al. (2016).

2.3 Fitting methods

One widespread technique of fitting synthetic spectra to real data makes use of grid-based χ^2 minimization. χ^2 is calculated as follows:

$$\chi^2(\theta) = \sum_{i=1}^{N} \left(\frac{F_i^{\mathrm{obs}} - aF_i^{\mathrm{mod}}(\theta)}{\sigma_i} \right)^2, \tag{2.11}$$

where F_i^{obs} is the observed flux in a given band, $F_i^{\text{mod}}(\theta)$ is the model flux, given some physical parameters θ, in the same band, σ_i is the uncertainty on the observation, a is a scale factor, and N is the number of bands. The way $F^{\text{mod}}(\theta)$ is calculated for each band is by convolving the synthetic SED with the transmission curves of the filter. This is done for every band and χ^2 is calculated for every possible synthetic spectra. The minimal value of χ^2, in principle, gives the synthetic SED that fits the data the best.

This approach is however overly simplistic and usually does not produce reliable results by itself. A more robust and common option is to use the Bayesian inference method where full probability distribution functions (PDFs) for each parameter are constructed. This is done by still calculating the χ^2 for each model but instead of simply picking the SED where χ^2 is minimized, this is used to estimate the likelihood of this SED (or the likelihood each SED model would produce the real data).

$$\omega_i = \exp\left(\frac{\chi_i^2}{2}\right), \tag{2.12}$$

where w_i is the weight of each model. Then a PDF is built using the weights of each model for each separate parameter. Then, the PDF can be studied in different ways the simplest of which is to assume it being Gaussian and taking its mean and standard deviation as an estimate of the corresponding physical property and its uncertainty, respectively. However, often this assumption is not good and other values can be used, e.g the median for the properties and the 16th and 84th percentiles for the lower and upper uncertainties.

These are the methods used by CIGALE, the code used for this work, but other methods based in Bayesian statistics also exist. Building a grid of all models is perhaps the most straightforward way but it and can get incredibly computationally intense as the dimensionality of the parameter space increases. An example of another very popular approach is sampling the parameter space using nested sampling (Skilling, 2006), e.g. as done in the fitting code named Bagpipes (Carnall et al., 2018; Carnall et al., 2019a). In this approach a set of samples of parameters is drawn from a continuous parameter space using the priors defined by the user, the SEDs corresponding to the drawn parameters are computed and compared to the data by estimating the corresponding likelihoods and the sample with lowest likelihood is removed. In the next iterative step the next sample is drawn from a restricted region in the prior distribution. This process is repeated ideally until convergence.

2.4 Code Investigating GALaxy Emission (CIGALE)

The particular SED fitting software used in this work is the Code Investigating GALaxy Emission, CIGALE (Boquien et al., 2019). It is a highly flexible code for SED fitting from the FUV all the way to the radio regime and it is written in python. It is modular meaning that it is easy to add and edit different modules (this was useful for this work in the case for the explored non-parametric SFH models that needed to be added and edited; see Chapter 3). CIGALE employs the

principle of energy balance – the energy absorbed by the dust of a galaxy in the UV to NIR is then re-emitted in the mid- and far-IR. CIGALE provides modules to model all important components of a galaxy SED – different SFHs including Ciesla, Elbaz, and Fensch (2017), stellar populations including Bruzual and Charlot (2003), Plat et al. (2019), Eldridge et al. (2017), and Maraston (2005), ionized gas (Inoue, 2011), dust attenuation (Calzetti et al., 2000; Charlot and Fall, 2000), dust re-emission (e.g. Draine et al. (2007), Casey (2012), and Dale et al. (2014)), and AGN (Fritz, Franceschini, and Hatziminaoglou, 2006; Dale et al., 2014; Stalevski et al., 2016).

CIGALE computes the physical properties of the sources in the following way:

1. For every possible combination of the input parameters, the galaxy physical properties are computed alongside the model fluxes this SED would produce.

2. All models are compared with the real data and the likelihoods for each model are estimated

3. The likelihoods are used to construct the PDFs of the physical properties and estimate their values and uncertainties.

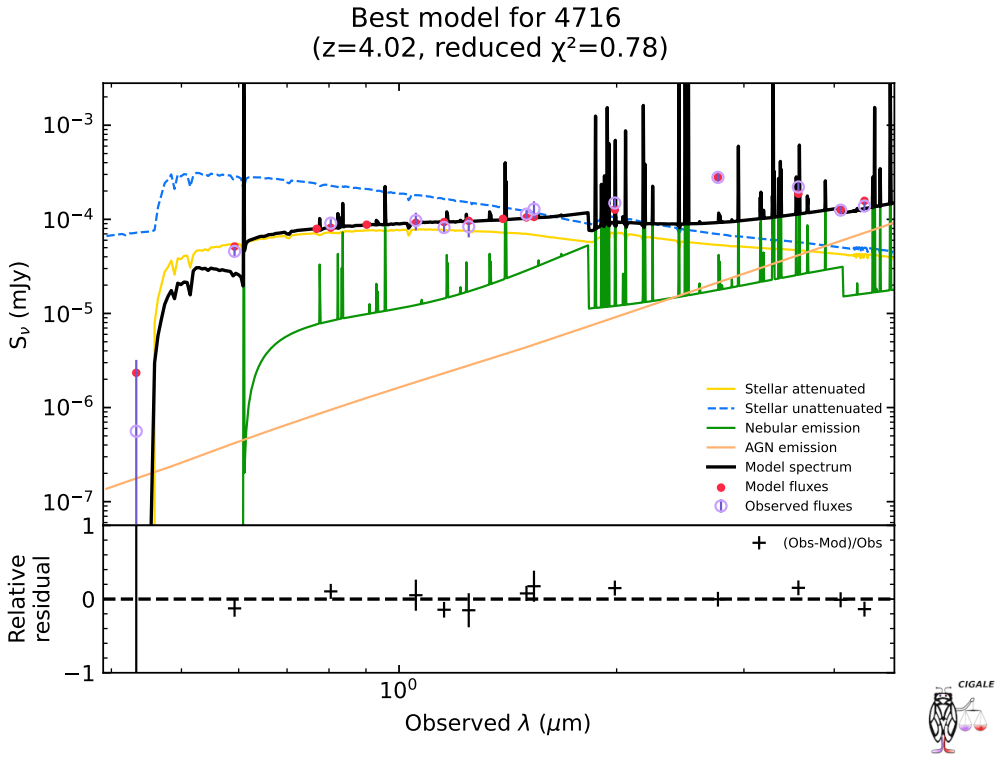

Figure 2.5: An example best SED generated with CIGALE for one of the objects modeled for this work with all components individually plotted.

The outputs of the software can be very flexible depending on user preference. The minimal output is a catalog with the obtained physical properties and model fluxes both from the best fit SED and after the Bayesian analysis. The list of physical properties to be saved can be edited by the user and minimized to save on computational time. Another flexible feature CIGALE has is to generate upon request different plots, most notably plots of the best fit SEDs for each source and

the PDFs of the physical properties but also e.g, the transmission curves of the filters used. An example of the best SED output for one of the sources in this work is shown in Figure 2.5. Another CIGALE feature that was of importance for this work is to do the Bayesian analysis on the physical properties directly in log-space.

Chapter 3

Data and Methods

In this chapter I present the dataset, the selection criteria used, the final sample, the chosen SED fitting setup, and the different procedures used to obtain the SFMS.

3.1 Dataset

In this thesis I used the ASTRODEEP-JWST catalogues, developed by the research group I joined. The dataset includes composite photometric catalogs based on data from eight deep-sky JWST observational programs: CEERS, DDT2756, GLASS-JWST, GO3990, JADES, NGDEEP, PRIMER, and UNCOVER. It includes data in 16 bands: eight from HST (ACS F435W, F606W, F775W and F814W; HST WFC3 F105W, F125W, F140W and F160W) and eight from JWST (NIRCam F090W, F115W, F150W, F200W, F277W, F356W, F410M, and F444W). These pass-bands span a wavelength range from 0.44 µm to 4.44 µm.

While the ASTRODEEP-JWST dataset is described in detail in Merlin et al. (2024), I summarize here the main steps.

The catalogs contain a total of 531,173 detected sources and covers and area of $\simeq$ 0.2 sq. degrees. The detection criteria was a 2σ detection in a stack of the F356W and F444W images. The software SExtractor was used for the source extraction. For the photometric measurements, the images were point spread function(PSF)-matched, meaning they were smoothed to the same resolution as the detection image. After that, the fluxes are determined by doing aperture photometry. The resulting dataset includes targets in seven different sky fields, an overview of which is shown in Table 3.1, including the area of each field, their depths, and the number of sources at $z > 4$ and in the final sample.

The AGN sample used in this work was directly taken from the ASTRODEEP-JWST catalogs. Sources were flagged as AGN based on their spectroscopic features according to the catalogs available in the literature, on their X-ray emission considering all sources with 2–10 keV luminosity larger than 10^{42} erg/s, or identified as AGN by the authors of the literature they used (see Merlin et al., 2024, and references therein). The sample used in this work, after all selection criteria described in the following sections, includes a total of 72 AGN.

A sample of 341 Little Red Dots (LRDs) was taken from Kocevski et al. (2023). The LRDs' SEDs were fitted but they were excluded from the main analysis of the

SFMS due to their still unknown nature.

One of the seven fields in the catalogs (Abell 2744) is a field that captures an area around the $z \sim 0.3$ galaxy cluster of the same name. This means that all sources that I observe behind the cluster are gravitationally lensed and that had to be taken into account in the estimation of their physical properties. The way I achieved this was by modelling the SEDs of those galaxies as observed and later applying a correction to take into account the amplified light, using the amplification factors from Bergamini et al. (2023).

3.2 Sample selection

I apply some simple selection criteria initially, namely I remove sources with less than 3σ significance in the detection band (F356W + F444W) and bad photometry measurements using the flags in the catalogs (I removed sources that lack more than 4 JWST bands, sources close to the border, saturated in detection, spurious, or having bad measurements in the two detections bands as well as sources flagged in the catalogs as bad after visual inspection.). The flags are described in Table 5 in Merlin et al. (2024).

3.2.1 Detection completeness limits

Detection completeness is related to the fact that at faint magnitudes not every single object with that brightness is detected. Having a good completeness of our sample is important as to do an unbiased study, a full sampling of all kinds of objects is necessary. The completeness curves for each of the seven fields in our sample are shown in Fig.4 of Merlin et al. (2024). For a detection limit of our work I chose 90%. To achieve this I used the tables, used to generate the plots in the paper. These tables include the magnitudes for which the completeness goes from one to zero in 19 discrete steps for every field. To determine the magnitude, at which there is 90% completeness for every field, I linearly interpolate between the values in the tables.

3.2.2 Finding reliable photometric redshifts

One fundamental problem in extragalactic studies is the correct determination of the redshifts of a large number of sources. The ASTRODEEP-JWST catalogs include photometric redshifts (inferred through SED fitting) for all galaxies as well as the spectroscopic redshifts of a very limited amount of sources. In this work, in order to obtain results for as large of a sample as possible I have to use mostly sources that have only a photometric redshift. This strategy, however, comes with its issues as, while overall the photometric redshifts in the catalogs are reliable (Fig. 10 in Merlin et al., 2024), this is not always the case. One significant effect of this is the appearance of unnatural peaks in the redshift distribution of galaxies. This issue is the most prominent in the PRIMER-COSMOS field, likely due to lower quality photometry. The effect is shown clearly in Fig. 3.1 where the redshift distribution of the sample before and after our P(z) selection criteria can be clearly seen. In the left panel there are two clear features around $z = 6$ and $z = 8$ wheres in the right panel both of those peaks are significantly decreased.
In order to select only sources with reliable enough photometric redshifts after extensive testing I devised a selection criteria related to the probability distribution

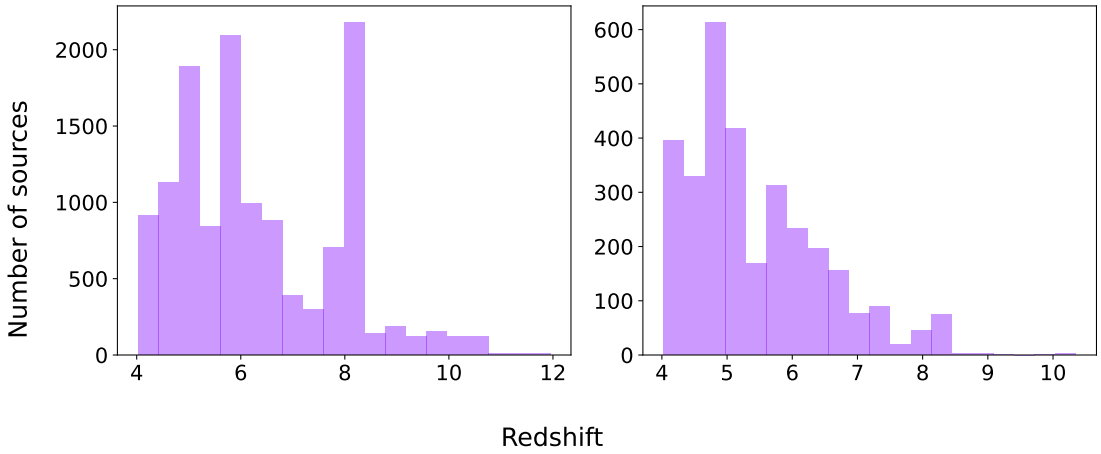

Figure 3.1: The redshift distribution of our sample in the PRIMER-COSMOS field. *Left:* after applying all selection criteria except the P(z) criteria. *Right:* Final sample with all criteria applied.

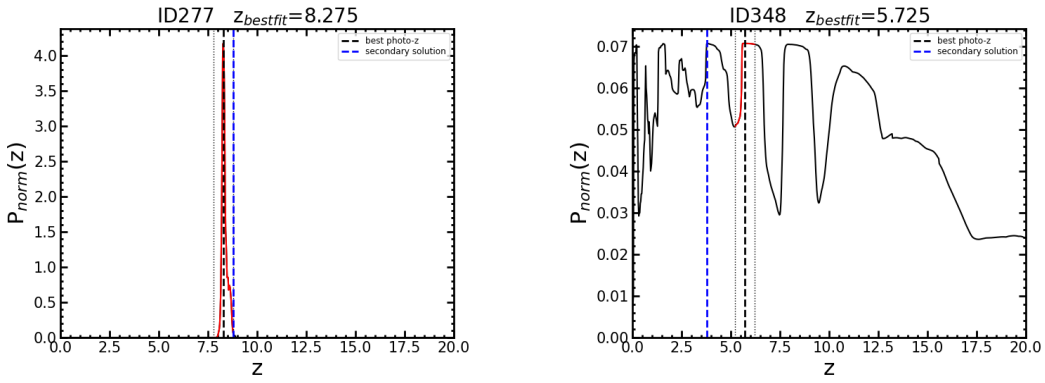

Figure 3.2: Examples of P(z) plots from the PRIMER-COSMOS field

of the photometric redshifts (i.e. the probability of the solution at each redshift). The criteria I incorporated was an attempt to remove sources with very degenerate photometric redshift solutions (as shown in the right panel of Fig. 3.2). In an ideal case, the P(z) distribution I am looking for should look like the example in the left panel of Fig. 3.2. There, a probability distribution with only one sharp peak that contains most of the probability in a small range around the peak is shown. The criteria used is based on two properties of the P(z) distribution:

1. $\mathrm{P_{int}}$ - the integrated probability in a range of ± 0.5 around the best fit redshift $z^\star$ ($\mathrm{P_{int}} = \int_{z^\star-0.5}^{z^\star+0.5} P(z)dz$)

2. $\mathrm{P_{pk2}}/\ \mathrm{P_{pk1}}$ - the ratio of the probability associated with the second best solution to the probability of the best-fit solution.

I tested what values for these two parameters provide a good compromise between retaining a good completeness of our sample while removing as many interlopers as possible. To do this I took a subsample of galaxies with known spectroscopic redshift and checked the amount of correctly and incorrectly rejected sources based on different values for $\mathrm{P_{int}}$ and $\mathrm{P_{pk2}}/\ \mathrm{P_{pk1}}$. I considered sources with

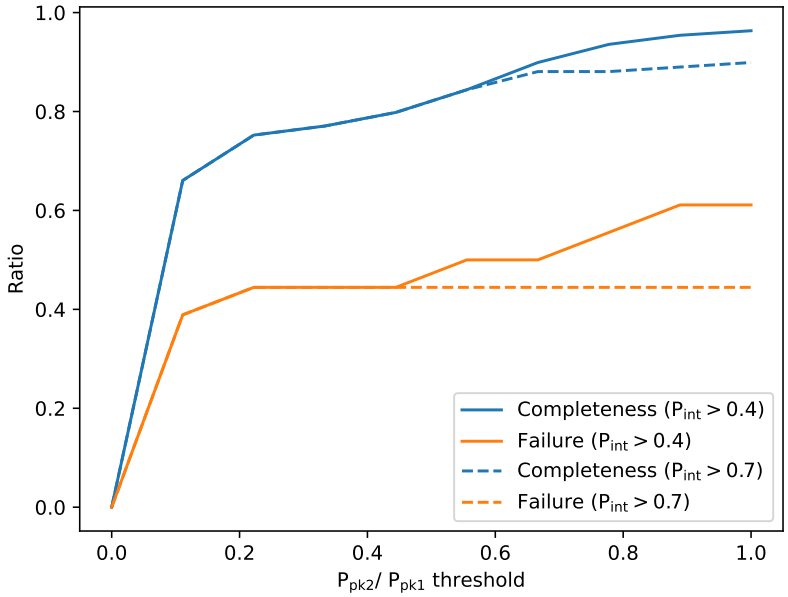

Figure 3.3: Plot showcasing the testing of our P(z) criteria for galaxies at $z > 4$in the COSMOS field. The solid lines represent the completeness and failure proportions for a range of different P_{pk2}/ P_{pk1} thresholds and $P_{int} > 0.4$. The dashed lines are the same but for $P_{int} > 0.7$.

$\left|\frac{z_{spec}-z_{phot}}{1+z_{spec}}\right| < 0.15$ as "good" photometric redshifts. I then plot two criteria for different values of both parameters - completeness and failure. The completeness shows us the proportion of galaxies having "good" photometric redshifts that are selected with given P_{int} and P_{pk2}/ P_{pk1}. The failure category encapsulates the proportion of galaxies that have "bad" photometric redshifts but were still selected using the respective criteria. In Fig. 3.3 I show the completeness and failure curves for a range of different P_{pk2}/ P_{pk1} thresholds and for two different P_{int} values. The galaxies for which I have spectroscopic confirmations largely had "good" photometric redshifts limiting the statistical weight of this test. I used the galaxies in the PRIMER-COSMOS field as it was the most problematic field that showed some very prominent peaks in the photometric redshifts distribution. Finally, for the selection of my final sample I decided on the following P(z) criteria:

1. $P_{int} > 0.7$
2. $P_{pk2}/ P_{pk1} < 0.5$

meaning I require the P(z) distribution to contain at least 70% of the probability in a region within ± 0.5 of the best fit photometric redshift and the second highest peak in the distribution to have no more than half of the probability of the first one. These criteria ensure a $\sim 80\%$ completeness and a fraction of outliers of $\sim$40%. Additionally, I impose a reduced $\chi^2 < 10$ criteria on the photometric redshift. In the last two columns of Table 3.1 the total number of sources at $z > 4$ and the number of sources in the final sample for each field are shown. The P(z) criteria imposed is the largest contributor to the cuts that is also very strongly field dependent (e.g. in both PRIMER fields the fraction of rejected sources to sources in the final sample is much larger than for the JADES fields).

Field	Area [sq. arcmin]	Depth [mag]	$N_{z>4}$	N_{final}
JADES-GS	84.5	28.27	1780	1342
JADES-GN	83.0	28.19	2005	1216
ABELL2744	45.7	28.84	3581	1247
NGDEEP	9.5	30.01	1538	505
CEERS	94.6	29.03	9640	2474
PRIMER-COSMOS	141.8	28.78	20639	3558
PRIMER-UDS	251.2	28.33	12169	3071

Table 3.1: A summary of basic statistics about each field. Depth here corresponds to the 90% detection completeness limit. N_{final} is the number of sources in each field left after all selection procedures.

3.2.3 The final sample

Stars were also removed using a combined criteria of SNR > 30 in the detection band and a stellarity index > 0.95.

I also limit this work in the redshift range $4 < z < 12$. The lower limit here speaks to the relative lack of SFMS studies in the higher redshift range. I therefore chose to focus on the higher end of the redshift distribution of sources for this work. The upper limit stems from the fact that after applying all of our selection criteria only 4 sources above redshift 12 are selected making any SFMS fits above this limit unreliable.

A histogram of the redshift distribution of the final sample is shown in Fig. 3.4, where I am left with 12 514 galaxies.

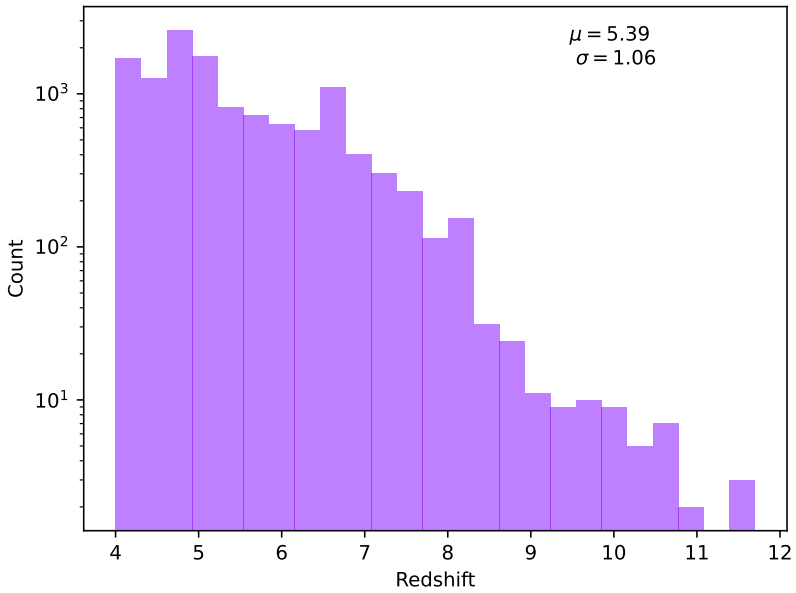

Figure 3.4: Redshift distribution of the sources in our final sample. The total number of galaxies is 12 514.

3.3 SED fitting of our sample

To infer the galaxy physical properties (namely the SFR and stellar mass), I fit the photometry with the CIGALE code.

The redshifts for the fitting were fixed, using the spectroscopic value if available, and the photometric one otherwise. For both properties I considered the Bayesian (likelihood weighted) value, calculated directly in log space by CIGALE (see Chapter 2). For the SFR estimates I considered the value averaged over the last 100 Myrs. Table 3.2 shows a summary of the parameter space used for the fitting, described below.

3.3.1 Star Formation History assumptions

I test 4 different SFH assumptions on one of the 7 fields - JADES-GS and compare how they affect the main sequence and its parameterization. The choice of field was made due to the fact that JADES-GS represents a good compromise between depth and area. The SFHs I chose were split in two broad categories - 2 parametric and 2 non-parametric ones.

The 4 modules used were:

1. `sfhdelayedbq` - This module implements a parametric SFH that takes the form of a delayed exponential with added flexibility for a short burst or quench episode with constant SFR. The SFR in this case takes the form from Equation 2.5. Here, the e-folding time (`tau_main` ($\tau_{\rm main}$)), the age of the burst/quench episode (`age_bq` (t_0)), the burst/quench fraction (`r_sfr` ($r_{\rm SFR}$)), and the age of the main stellar population (`age_main` (t)) are the free parameters.

2. `sfhdelayed` - This module also uses a delayed exponential for the parametrization of the SFH. I also add a short additional bust (with the same parametrization) to it. The SFR in this case takes the form from Equation 2.6, where the intensity of the burst is determined by the `f_burst` parameter that provides the fraction of stellar mass produced in the burst episode. Therefore, there are the $\rm SFR_{delayed}$ free parameters from before (except r_SFR) plus the age of the burst episode (`age_burst`(t_0)), the e-folding time for the burst component (`tau_burst`($\tau_{\rm burst}$)), and `f_burst`.

3. `sfhNlevels_flat` - This is a non-parametric SFH module. The SFH in this case is retrieved by calculating the SFR in linearly spaced bins in time and a flat prior. In this case the parameters to input are the age of the oldest stellar population (`age_main`), the age of the most recent bin (`age_1st bin`), the number of bins to calculate the SFR in (`N_bins`), and the seeds from which to generate the SFHs that are later fitted (`N_SFH`).

4. sfhNlevels_flat_log - A nonparametric model similar to `sfhNlevels_flat` but in this case the bins are logarithmically spaced in time.

For the `age_main` parameter in all runs I elected to have it go from 100 Myrs to 1500 Myrs in steps of 100 Myrs. This corresponds roughly to the age of the universe at the lowest and largest redshifts in our sample. However, I fix the age of each

	Module	Parameter	Value
SFH modules	sfhdelayedbq	tau_main	100, 300, 500, 700, 900, 1100, 1300
		age_main	from 100 Myrs to 1500 Myrs with a 100 Myrs step
		age_bq	10, 25, 50, 75, 100
		r_sfr	0.25, 0.5, 0.75, 1.0, 1.5, 2.0, 5.0, 10.0, 100.0, 1000.0
	sfhdelayed	tau_main	100, 300, 500, 700, 900, 1100, 1300
		age_main	from 100 Myrs to 1500 Myrs with a 100 Myrs step
		tau_burst	10, 25, 50
		age_burst	5, 10
		f_burst	0.0, 0.1, 0.2, 0.3, 0.4, 0.5
	sfhNlevels_flat	age	from 100 Myrs to 1500 Myrs with a 100 Myrs step
		age_1stbin	30
		sfr_max	500
		N_bins	10
		N_SFH	500 evenly spaced values from 0 to 500
Common modules	bc03	imf	1 (Chabrier)
		metallicity	0.0004, 0.004, 0.02
		separation_age	10
	nebular	logU	-1.0, -2.0, -3.0
		zgas	0.002, 0.004, 0.02
	dustatt_modified_CF00	Av_ISM	24 linearly spaced values from 0.0 to 3.0 mag
		mu	0.2, 0.3, 0.4, 0.5
		slope_ISM	-0.7
		slope_BC	-1.3
	redshifting	redshift	—
AGN component	skirtor2016	i	30, 70
		disk_type	2
		delta	0, 1*
		fracAGN	0.1, 0.3, 0.5, 0.7, 0.9
		lambda_fracAGN	0.4/0.4

Table 3.2: Parameters used for our CIGALE runs. The common modules were always kept the same, while for our SFH assumptions tests we used the three different SFH modules shown in the table and a fourth SFH model – a modified version of `sfhNlevels_flat` that uses the same input parameters but spaces the bins logarithmically in time – `sfhNlevels_flat_log`. For our main results over all fields we used the sfhdelayedbq module. The AGN component was used only on the confirmed AGN sources. The parameters denoted with * correspond to our ADAF and thin disk runs respectively. For each individual run the parameter was kept fixed (i.e. either fitting only ADAF or only a think disc) but both of the values were used for different runs. For the `nebular` and `skirtor2016` components, all parameters omited from this table were kept fixed at the default values.

galaxy at a maximum of 100 Myrs younger than the age of the universe at its measured redshift to avoid degeneracies in the fitting.

3.3.2 Stellar population

The stellar population Bruzual and Charlot (2003) (module `bc03`) was used in this work with a Chabrier IMF(`imf`)(Chabrier, 2003), and a range of metallicities $Z = 0.0004, 0.004, 0.02$ - 2%, 20%, and 100% of the solar metallicity respectively.

3.3.3 Nebular emission

In the nebular emission module I vary only two parameters: the ionization parameter (`logU`), and the `metallicity` (Z). For the former I use `logU` $= -1.0, -2.0, -3.0$ to give our grid flexibility in the level of ionization. For the metallicity I choose values similar to those for the stellar population - $Z = 0.002, 0.004, 0.02$.

3.3.4 Dust attenuation

I adopt the Charlot and Fall, 2000 model (module `dustatt_modified_CF00`) as described in Chapter 2.

This module has two free parameters:

- `Av_ISM`: the V-band attenuation in the ISM.
- `mu`: the ratio of the V-band attenuation in the ISM to the total V-band attenuation.

The parameter μ describes the distribution of the dust in the galaxy: 0 if the dust is fully concentrated in star-forming regions, 1 if it is evenly spread across the galaxy. The physical properties of galaxies are sensitive to the dust content, so for both parameter I input a wide range of values.

3.3.5 Fitting the AGN component

I tested how the position of AGN on the SFR-M$_\star$ changes depending on the way their SED fitting is performed. I specifically tested how their position would potentially affect the SFMS if they are undetected and therefore modeled as regular galaxies. In order to quantify this difference I fit our AGN in three different ways - without an AGN component, and with an AGN component – once with ADAF (advection dominated accretion flow) and once with a thin disk. Thin discs are very effective at radiating away the heat generated due to viscous stress in the accretion disc, letting them stay cool and geometrically thin. This is not the case for ADAF where the radiative efficiency is low, meaning that the disc retains heat, the ions reach near virial temperatures and the geometry of the gas changes to near spherical rather then a disc. In this scenario, a large portion of the energy from the viscous stress is advected towards the black hole rather than radiated, making the AGN one of a lower luminosity (Narayan et al., 1998). These two accretion models are typical of luminous (thin disc) and underluminous (ADAF) AGN.

When fitting with the AGN component I provided a range of values for only two parameters: the inclination (`i`) and the AGN fraction (`fracAGN`). The rest of the

parameters stayed fixed. The AGN fraction is the fraction of AGN IR luminosity to total IR luminosity at a given rest-frame wavelength (in this work – 4000 Å).

3.4 Mass completeness

To fit the SFMS I need to first acquire the mass completeness limits of the sample. This means that I need to have an estimate down to what mass the full SFR distribution is sampled.

At the lower mass end of the sample, only the most star forming galaxies are detected. This is not solved by our detection completeness cut because of the intrinsic scatter in the mass-to-light ratio, meaning that a magnitude cut cannot uniquely be translated in a mass cut. This is an issue since in such a case only the upper envelope of the SFMS is sampled. This would not only drive the fit, but also affect the average obtained scatter. Therefore, it is necessary to estimate for the mass completeness limit and consider only sources above it for deriving the SFMS parameters. The mass completeness limits are different in each field, since they have different depths, and in each redshift bin, as increasing the distance the ability to sample the faintest galaxies is limited and the mass completeness limit increases.

To obtain the mass completeness limits in redshift bins in each field I used the prescription used in Pozzetti et al. (2010). The method is straightforward and easy to implement. It is done a a few steps:

1. I calculate a"limiting mass" - $\mathcal{M}_{\rm lim}$ for all galaxies in the sample. This corresponds to scaling all masses down to the mass each galaxy would have if its flux was at the limiting magnitude. The way that this is calculated is as follows:
$$\mathcal{M}_{\rm lim} = M_{\star} + 0.4 * (m_{\rm det} - m_{\rm detcomp}), \tag{3.1}$$
where $M_{\star}$ is the obtained mass of the respective galaxy, $m_{\rm det}$ is the magnitude of the source in the detection band, and $m_{\rm detcomp}$ is the detection completeness magnitude.

2. I get the 20% faintest galaxies in the sample and look at the distribution of their $\mathcal{M}_{\rm lim}$. This choice is made as to select only galaxies with typical $\mathcal{M}/L$ ratios near the detection limit. This is to avoid using the reddest and brightest galaxies with highest $\mathcal{M}/L$ ratios as they do not contribute significantly near the detection limit and their inclusion would make for overly conservative cuts (Popesso et al., 2023).

3. For the mass completeness in the respective field and redshift bin I choose the threshold below which 90% of the "limiting masses" lie, by only considering the 20% faintest galaxies subsample.

The results I obtain for each field and redshift bin are shown in Fig. 3.5, alongside all "raw" stellar masses and the 20% faintest sources (in the respective redshift bin), scaled to their "limiting mass". In the upper panel of Fig. 3.6 I show the mass completeness limits of all fields plotted against the redshift for the `delayedbq` SFH module, used for the bulk of this work. In the lower panel the mass completeness only for the JADES-GS field using all 4 different SFH assumptions is shown. The

trends seen in Fig. 3.6 and 3.5 are expected: the mass completeness threshold generally increases with redshift and deeper fields have a lower mass completeness limits overall (e.g., in NGDEEP). In some cases, these general trends are affected by small number statistics, especially in the highest redshift bin where the number of sources is low in most fields.

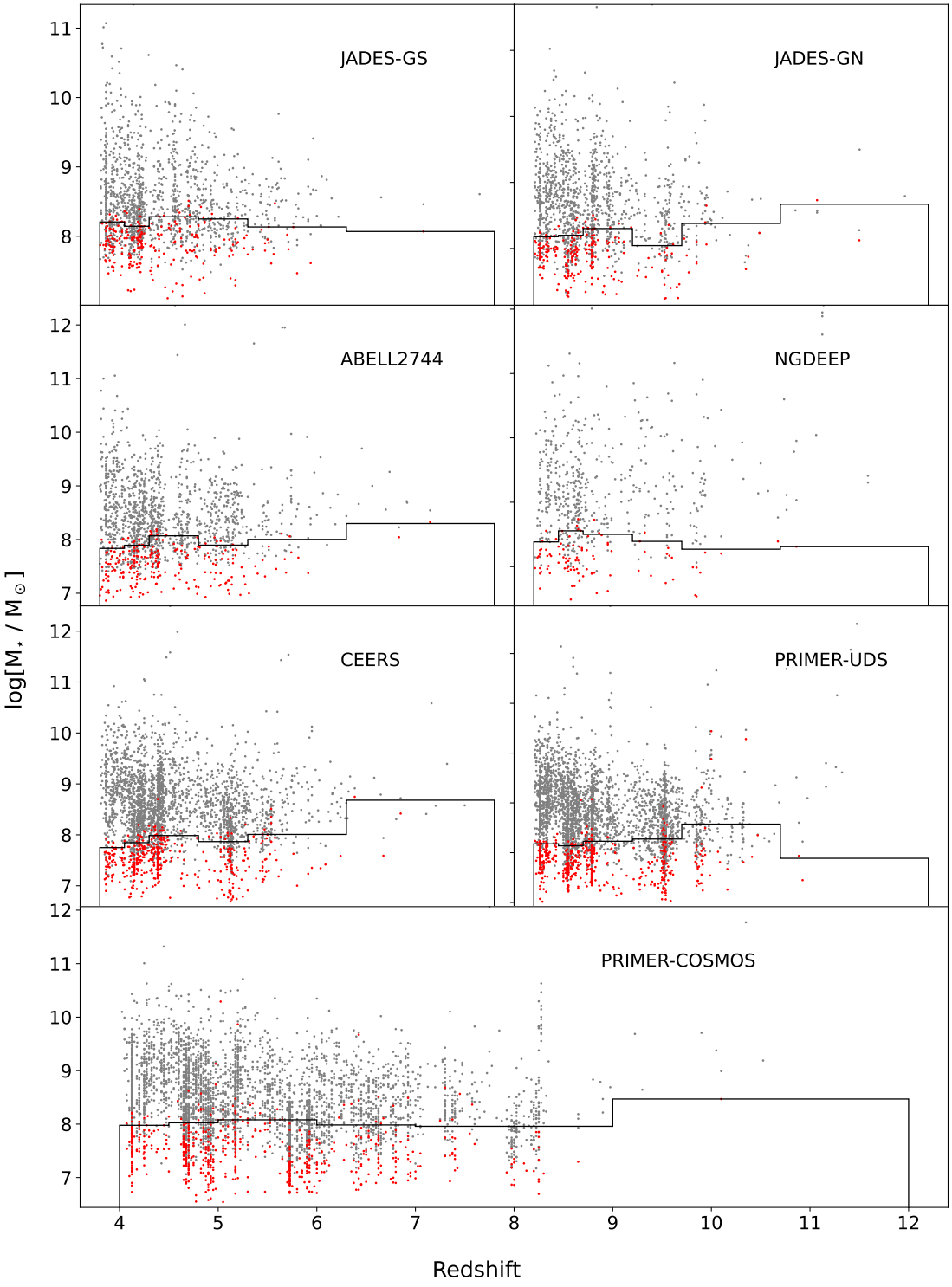

Figure 3.5: Mass completeness limits in each of the 7 JWST fields in each redshift bin (solid lines). The gray points are the original masses of all objects. The red points are the limiting masses of the 20% faintest galaxies

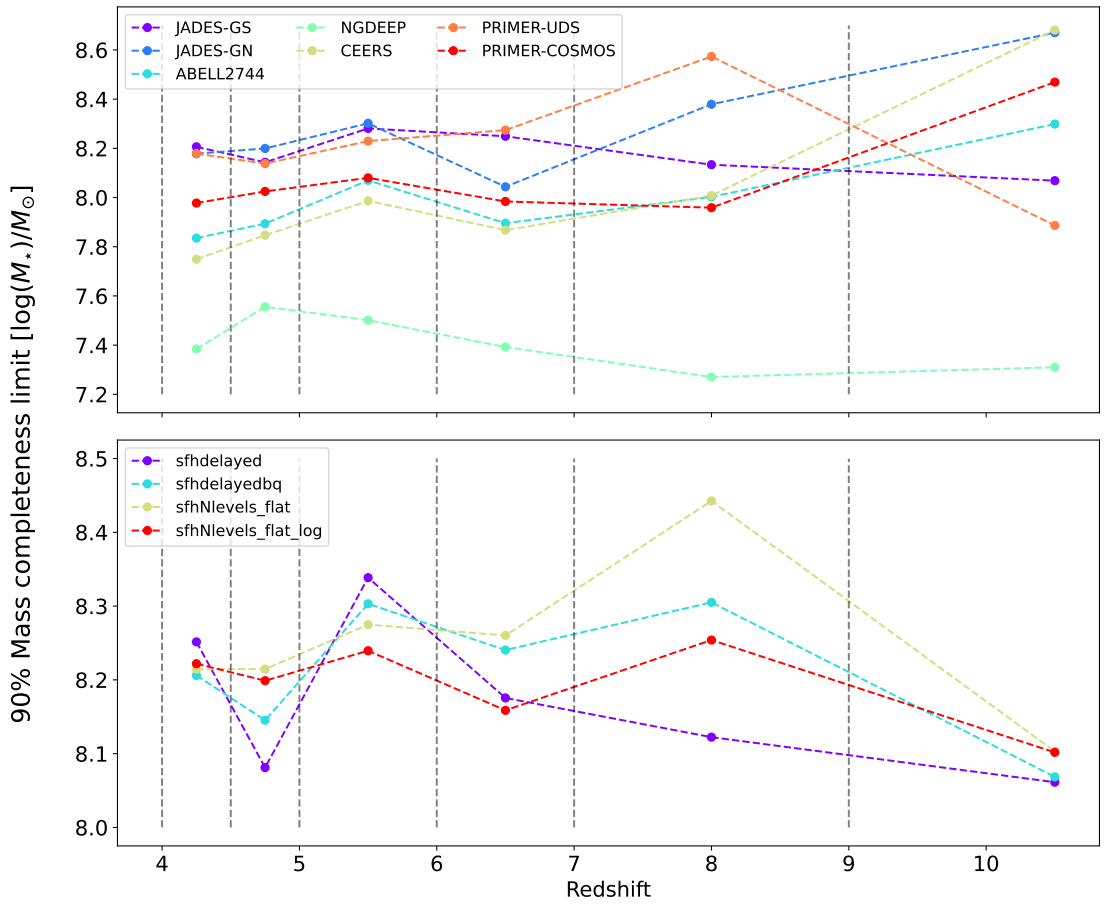

Figure 3.6: *Top:* Mass completeness for each field plotted against redshift, using the `delayedbq` SFH module. *Bottom:* Mass completeness for the four tested SFHs in the JADES-GS field.

3.5 Fitting the SFMS

In order to fit the SFMS I combined the data from all 7 fields and used only sources above the mass completeness limit for each field and redshift bin. When the data for all seven fields is combined I have 10 015 sources in total above the mass completeness limits. For the fitting of the SFMS I also removed the 72 AGN and the 341 LRDs (even though their SEDs are still fitted and they are presented on the plots).

3.5.1 Fitting in redshift bins

I parametrize the SFMS as in Equation 1.1 but the intercept is evaluated at the median stellar mass for the sample – $10^{8.54} M_{\odot}$. I weigh all points with their respective y-axis uncertainties. I neglect the uncertainties on the derived stellar masses so I can perform a regular least squares fitting.

To reduce the effects of outliers (e.g, quiescent galaxies, especially in the lower redshifts) on the inferred SFMS, I introduce sigma clipping of our sample. The procedure is as follows:

1. Perform an initial fit over all data points above the mass completeness limits. In this stage I weigh all points equally, irrespective of their uncertainties as to avoid a small number of galaxies with spuriously small uncertainties driving the fit.

2. I sigma clip the data around the initial fit, using a 3σ threshold, meaning that all sources whose distance from the first fit is more that three times the sigma of the sample around the fit are removed.

3. I finally fit the sigma clipped data points using the standard procedure described above.

The uncertainties of the parameters of the fit (slope and intercept) are then determined by assuming the slope and the intercept are independent and taking the square root of the respective element of the covariance matrix that is one of the outputs of the scipy.optimize_curve procedure. The scatter is obtained by splitting the data in narrow stellar mass bins ($\Delta M_\star = 10^{0.2} M\odot$) and the standard deviation of the SFR in the bin is taken. Then, the scatters in all bins are averaged to obtain the average scatter around the SFMS. This method was chosen, as opposed to calculating the scatter around the best fit line, as it is independent of the fit itself.

3.5.2 Time dependent fit

I also test another parametrization of the SFMS: Equation 1.2, as described in Chapter 1. This corresponds to Equation 10 in Popesso et al. (2023). This form of the SFMS lets us fit all of the data at the same time instead of splitting it into different bins. Another important feature of this parametrization is the inclusion of turnover of the SFMS at higher masses, an effect well observed, especially at lower redshifts (Popesso et al., 2023). The procedure I use in this case is very similar as before: I take all data (above the mass completeness limits) and perform a regular least squares regression, while weighing all points with their log[SFR] uncertainties. For the mass completeness limit estimates I still use the same redshift bins as before.

Chapter 4

Results

In this chapter I present the various results in this thesis: the effects of the different SFH assumption on the SFMS, the derived SFMS in each individual field in different redshift bins, and the SFMS for the whole sample fit with two different parameterizations.

For all of the results in this thesis, the SFR averaged over the last 100 Myrs (SFR_{100}) was used. This was due to our dataset not being sensitive enough to variations in the SFR on shorter timescales (discussed in Chapter 1), making the evaluation of the instantaneous SFR very uncertain. Using the same reasoning, the lack of starburst galaxies in the following results can also be explained.

4.1 Impact of Star Formation History assumptions

The assumed functional form of the SFH is one of the key elements going into SED fitting, as described in detail in Chapter 2. I modelled the sample of galaxies in the JADES-GS field with the four different SFH modules described in Chapter 2 and Chapter 3:

- `sfhdelayedbq` - a delayed exponential model with a short constant burst or quench episode.
- `sfhdelayed` - a delayed exponential model with an additional exponentially declining burst phase.
- `sfhNlevels_flat` - a non-parametric model with flat priors and linear binning in time.
- `sfhNlevels_flat_log` - a non-parametric model with flat priors and logarithmic binning in time.

I show the results in the following two figures: Fig. 4.1 and Fig. A.2. The results from the two parametric SFH forms are shown in Fig. 4.1, while the results form the two non-parametric models can be seen in Fig. A.2. In the case of this test we limit the sample to redshift $4 < z < 9$ as for an individual field there is a very low number of sources in the highest redshift bin ($9 < z < 12$), insufficient to obtain reasonable fits of the SFMS.

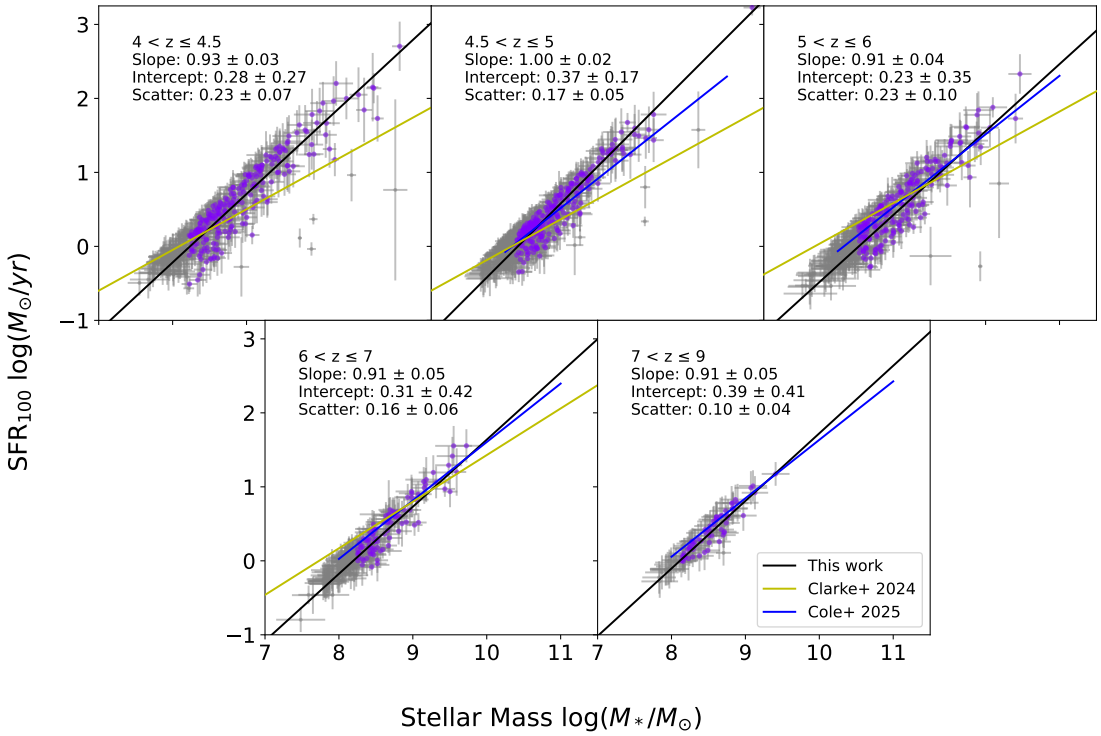

Figure 4.1: SFR-M$_\star$ diagrams obtained from fitting the sources in the JADES-GS field with the `sfhdelayedq` SFH module. The diagrams show the derived SFMS in 5 redshift bins spanning from $z = 4$ to $z = 9$. The purple points show the points used for the SFMS fitting, while the gray points show sources that were either bellow the mass completeness limit or were rejected during the sigma clipping procedure. The black solid line is this work's fit to the data. The two color solid lines are comparisons with the literature - Cole et al. (2025) (blue) and Clarke et al. (2024) (yellow). The intercept is evaluated at the median mass of the sample – $10^{8.54}$ M$_\odot$.

Plots, summarizing the results of this test, are shown in Fig.4.2. There I show the comparisons between the derived SFMS properties for the different SFH assumptions in four redshift bins up to $z = 9$. In the case of the intercept and the scatter of the SFMS all SFH models are consistent with each other within the error bars for the whole redshift range.

For the scatter, this result is somewhat in contradiction with findings from literature (Ciesla, Elbaz, and Fensch, 2017; Carnall et al., 2019b; Carvajal-Bohorquez et al., 2025, and references therein) where authors find that the assumed SFH shape, and specifically the burstiness of the SFH, can significantly impact the resulting SFMS scatter. This can be explained in part by the fact that we use the SFR$_{100}$ indicator and in part by the fact that lower scatters are expected from parametric models with no flexibility relating to recent bursts but all four models tested in this work provide such flexibility. The scatters obtained from all SFH models in this work are fully consistent with the scatters from Cole et al. (2025) and inconsistent with the results from Clarke et al. (2024). These two works are among the first SFMS results obtained with JWST data which is why they are used as the first point of comparison for results in this thesis. In those two papers they use a non-parametric SFH from Iyer et al. (2019) in Cole et al. (2025) and a parametric delayed exponential model in Clarke et al. (2024).

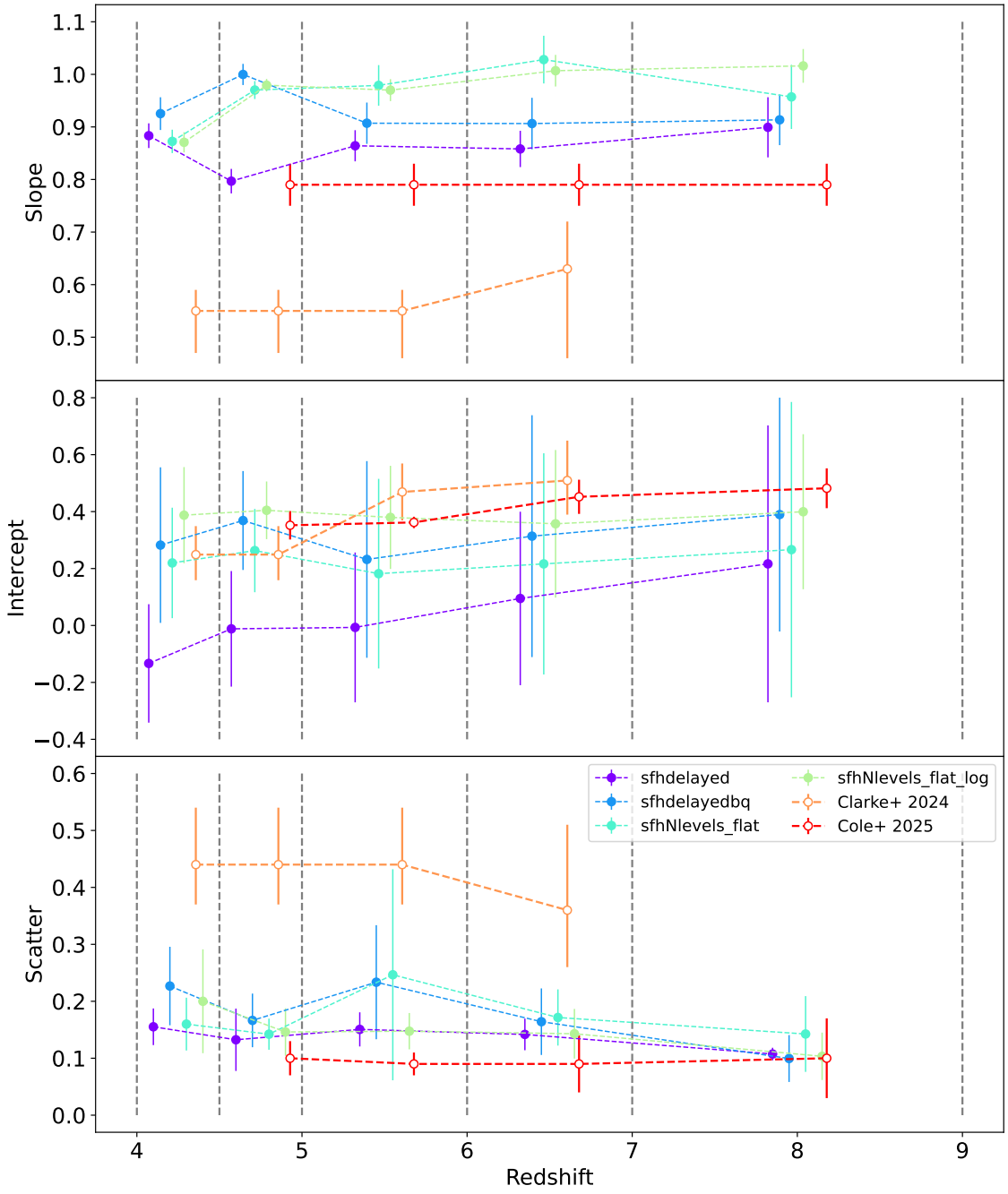

Figure 4.2: Evolution with redshift of the MS parameters using different SFH assumptions in JADES-GS (solid symbols). Open symbols show recent results from the literature. The points correspond to the values in the respective redshift bin and are shifted in redshift for clarity. Bin edges are shown with dashed grey lines. The intercept is evaluated at the median mass of the sample – $10^{8.54}$ $M_{\odot}$.

This is to be expected since Clarke et al. (2024) use the instantaneous SFR rather than SFR_{100}. This effect is also seen in the two sets of results in Cole et al. (2025) where they obtain notably larger scatters when they average the SFR on a shorter timescale (SFR_{10}). In both Cole et al. (2025) and Clarke et al. (2024) they use SED fitting as a way to infer the physical properties of the galaxies. In Clarke et al. (2024) they compare these results with other SFR tracers as well but in this thesis I only consider their results based on SED fitting, for consistency with our method.

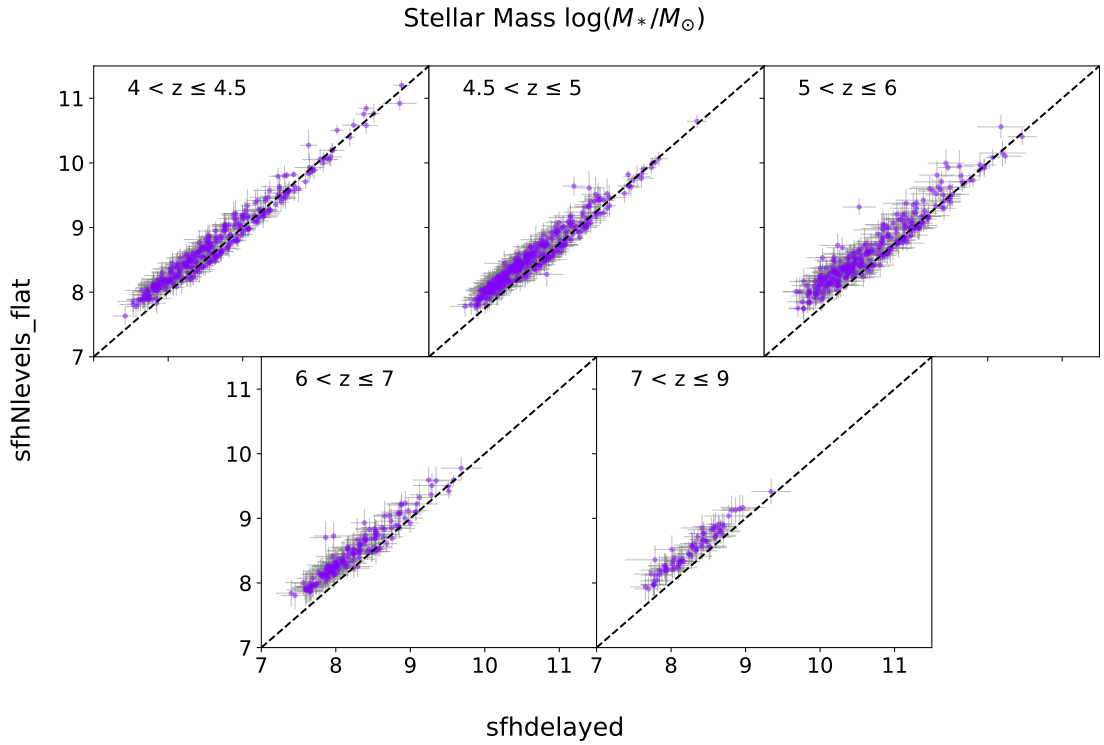

Figure 4.3: Direct comparisons for the inferred stellar masses in the JADES-GS field with two different SFH assumptions – `sfhNlevels_flat` and `sfhdelayed`.

For the slope of the main sequence, above redshift $z = 5$ there is a clear grouping of the parametric and non-parametric models where the two non-parametric models show a larger SFMS slope compared to what is obtained from parametric models. This effect is further examined in Figure 4.3 and Figure 4.4 where the comparisons between the stellar masses and the SFRs of two of the four models are directly compared. When comparing the properties directly, the non-parametric model (`sfhNlevels_flat`) seems to produce higher masses compared to the parametric model (`sfhdelayed`) mostly at the lower end of the mass distribution but the two models are consistent at higher masses, explaining the steeper slope for the non-parametric model. This is unsurprising as the effect has been studied before (e.g. Leja et al., 2022). All other combinations of comparisons are shown in Appendix B.

The slope from the `sfhdelayed` SFH model is marginally consistent with the results from Cole et al. (2025) (when comparing with their results with the SFR_{100} indicator) at all redshifts whereas there are significant differences between Cole et al. (2025) and the other SFH assumptions. The results from Clarke et al. (2024) are notably inconsistent with the results in this work possibly because they use the instantaneous SFR, rather than SFR_{100}.

4.2 The SFMS in the seven different fields

In Figure 4.1, I show the SFR-$M_\star$ diagram with the fit of the SFMS. The same plots for the other six fields are shown in Appendix C. These results were obtained after

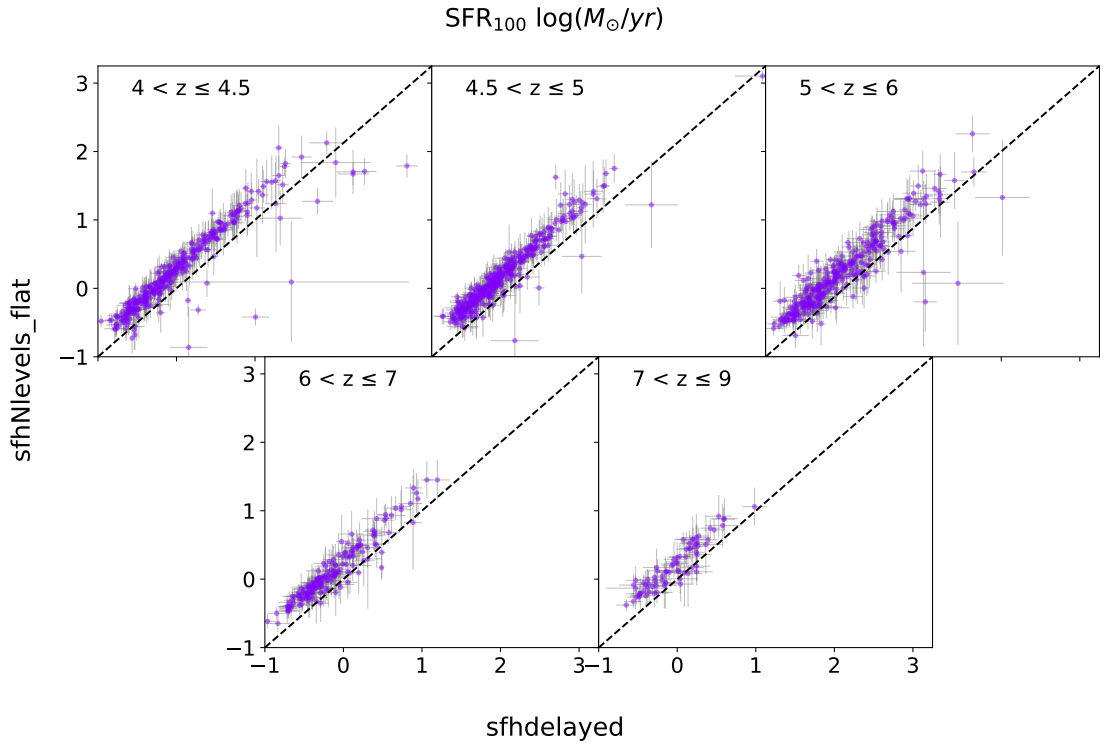

Figure 4.4: Same as in Figure 4.3 but for the inferred SFR.

SED fitting the whole sample, as described in Chapter 3, with the `sfhdelayedbq` SFH module. The motivation behind looking into the SFMS of each field separately is to try and gain some qualitative insight into the cosmic variance. A clearer comparisons of the respective SFMS parameters in each field are shown in Fig. 4.5. As before, the intercept and the scatter are found to be largely within the error bars both for the different fields and for the full range of redshifts. This is not the situation for the slope of the main sequence where at all redshifts there are significant differences between fields. These differences might be the result of multiple factors. The different fields probe different parts of the SFMS as, for example, NGDEEP and ABELL 2477 have much lower mass completeness limits than the other fields (NGDEEP as it is deepest field, and ABELL 2477 because gravitational lensing allows the detection of lower mass sources, whose light is amplified above the magnitude limit). On the opposite end, very massive galaxies are rarer, meaning that in small fields there is a lack of statistics at the high mass end of the SFMS. For this reason, in the main result of this thesis I combine the sources from all fields to achieve a larger and more representative sample.

The results were also compared to the values found in Cole et al. (2025) and Clarke et al. (2024) and I find that the intercept is consistent with these studies at all redshifts and in all fields, however I find significantly larger slopes in all cases. The slopes i find are however consistent with other works (e.g., Santini et al., 2017, and references therein). In the comparison with Clarke et al. (2024) we also have to keep in mind the difference in the SFR estimator considered (SFR vs SFR$_{100}$). Both Cole et al. (2025) and Clarke et al. (2024) use data from the CEERS program. In Clarke et al. (2024) they also include data from the JADES program.

Overall, for the intercept and scatter estimates the statistical uncertainties play an overwhelming role, wheres for the slope I find that the cosmic variance can

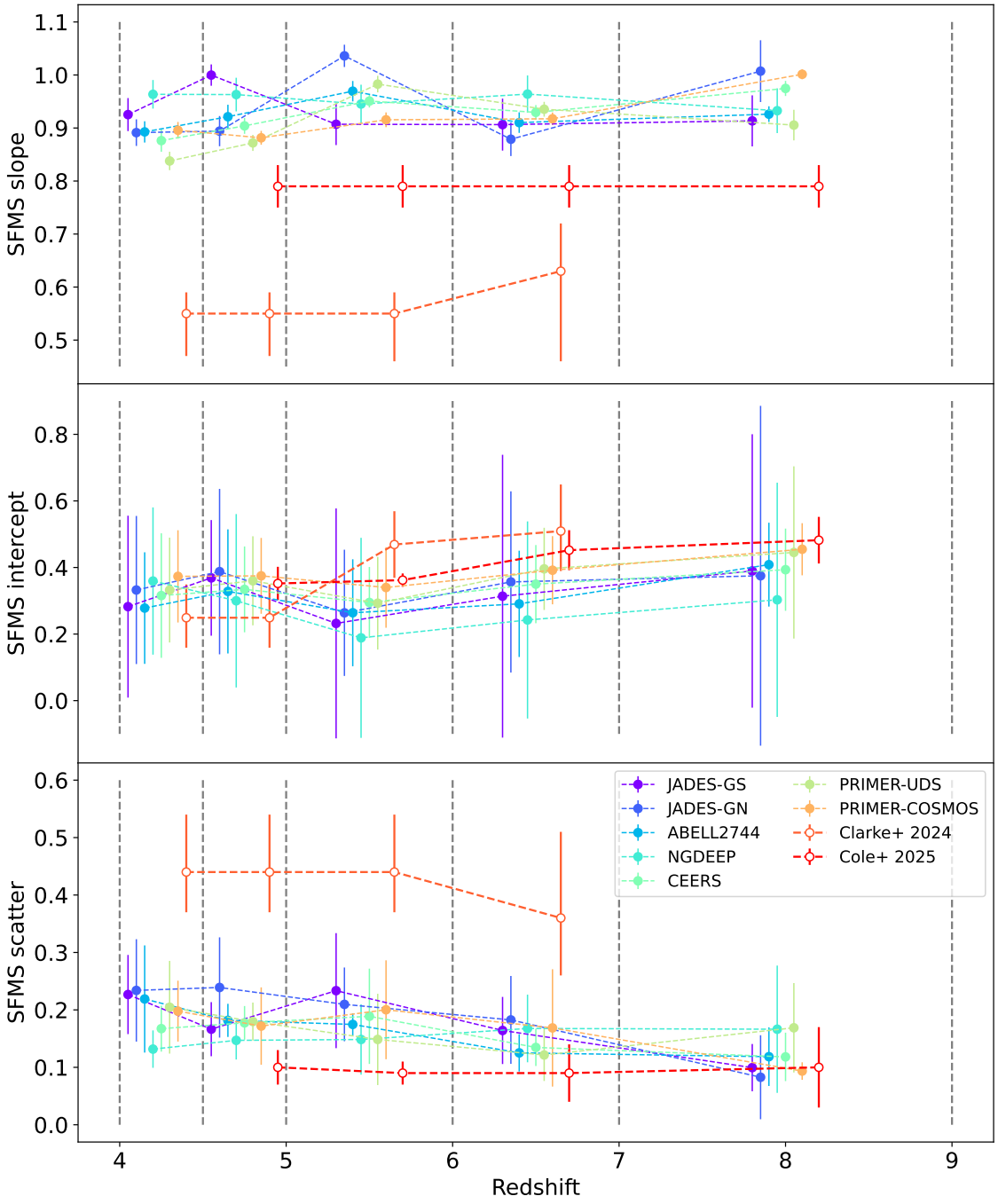

Figure 4.5: The evolution with redshift of the slope, intercept, and scatter of the SFMS in all 7 fields (solid symbols). Open symbols show recent results from the literature. The points represent the values in the respective redshift bin and are shifted in redshift for clarity. The bin edges are indicated with dashed gray lines. The intercept is evaluated at the median mass of the sample – $10^{8.54}$ $M_{\odot}$.

introduce differences of up to ~ 15 %. The results for the slope can vary significantly between fields, especially at lower redshifts. In the high redshifts, the statistical uncertainties grow larger and the differences between fields become less pronounced.

	$4 < z \leq 4.5$	$4.5 < z \leq 5$	$5 < z \leq 6$	$6 < z \leq 7$	$7 < z \leq 9$	$9 < z \leq 12$
Slope	0.89 ± 0.01	0.92 ± 0.01	0.97 ± 0.01	0.96 ± 0.01	0.97 ± 0.01	0.96 ± 0.02
Intercept	0.32 ± 0.06	0.35 ± 0.05	0.30 ± 0.06	0.36 ± 0.05	0.41 ± 0.06	0.38 ± 0.20
Scatter	0.22 ± 0.09	0.19 ± 0.07	0.19 ± 0.07	0.13 ± 0.04	0.12 ± 0.03	0.13 ± 0.06

Table 4.1: Summary of the parameters of the SFMS from the fits over the whole sample in all seven fields in six redshift bins spanning from $z = 4$ to $z = 12$. The intercept is evaluated at the median mass of the sample – $10^{8.54}$ $M_{\odot}$.

4.3 The MS for the whole sample

The main results of this thesis, however, center around fitting the SFMS over the whole sample of galaxies in all seven fields. This way we can achieve significantly better statistics and can even provide a somewhat meaningful fit in one more redshift bin ($9 < z \leq 12$). This was done in two ways: first I discuss fitting a line in log space in each redshift bin separately and then fitting a time-dependent parametrization of the SFMS using all data points at the same time (Both methods are discussed in Section 3.5).

4.3.1 Fits in redshift bins

For this purpose I split the data in six redshift bins and combine all galaxies form all fields, taking into account the appropriate mass completeness limits of each field and redshift bin. These results are shown in Fig. 4.6. The AGN and LRDs in the sample are also over plotted on this figure but were not used for the SFMS fit. All data points were obtained by SED fitting the sources with a `delayedbq` SFH and no AGN component. The parameters of the derived fits are shown in Table 4.1 and Figure 4.7 where they are also compared with the parameters obtained by Clarke et al. (2024) and Cole et al. (2025).

Similarly to my results in Section 4.2, the slope for the whole sample is also significantly larger than the slopes obtained by Clarke et al. (2024) and Cole et al. (2025) (albeit much closer to slopes from other studies (e.g, Speagle et al., 2014; Santini et al., 2017, and references therein)). This is even more pronounced in this case as the uncertainty on the derived parameters decrease for the fits over the whole sample, as the statistics improve greatly when the seven fields are combined. The slope derived in this work follows a trend of mild increase at lower redshifts and settles to a constant value after $z \sim 5$.

The obtained intercept and scatter in this thesis are both consistent with a flat trend and are mostly consistent with literature. The notable difference in the scatter between this work and Clarke et al. (2024) can be the result of the different timescale over which we average the SFR, as discussed in Section 4.2.

4.3.2 Time dependent fit of the MS

A straight line in log-log space is not the only possible parametrization of the SFMS. As described in Chapter 1, one alternative is the form used in Equation 10 in Popesso et al. (2023). There are two separate ways in which this parametrization differs from the one used in previous sections:

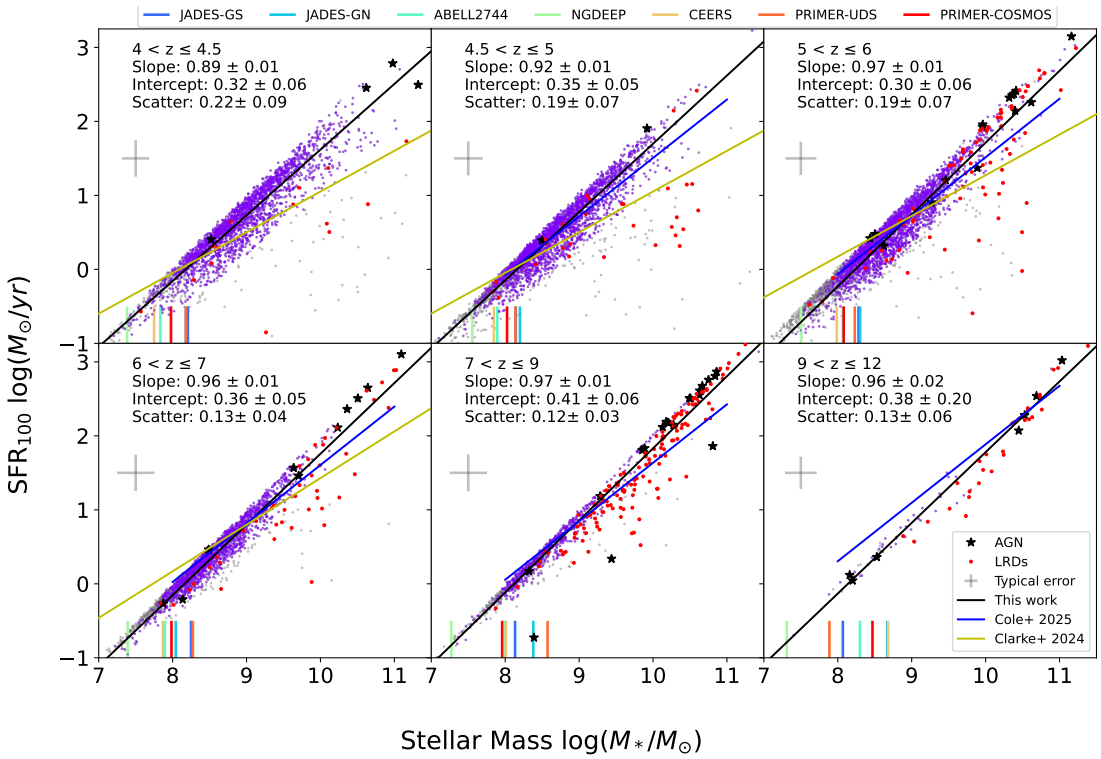

Figure 4.6: SFMS fits in each redshift bin for the full sample of galaxies, including AGN and LRDs. The SED fitting for the AGN and LRDs was done in the exact same way as for the rest of the sources (no AGN component). The AGN and LRDs were not included in the SFMS fitting procedure. The purple points represent the sources used for the fitting while the gray points are galaxies that either fell bellow the mass completeness limit or were excluded during the sigma clipping procedure. The small vertical lines represent the 90% mass completeness limits for each field and redshift bin. The black solid line is my fit to the data. The two colored solid lines are comparisons with the literature - Cole et al. (2025) (blue) and Clarke et al. (2024) (yellow). The intercept is evaluated at the median mass of the sample – $10^{8.54}$ $M_{\odot}$.

1. It fits all of the data together in SFR-$M_{\star}$-cosmic time space.

2. It allows for a turnover in the SFMS.

In Fig. 4.8, I show the time dependent fit over this dataset. The derived fit parameters are shown in Table 4.2. In the plot, the fit at the middle point of every redshift bin is shown. It matches near identically to the linear fits in redshift bins (also shown in the figure).

In the intermediate masses, a good agreement between my fit and the fit derived in Popesso et al. (2023) is present. In the low masses a possible reason for the disagreement might be the lack of sampling in Popesso et al. (2023). This study uses pre-JWST data meaning they do not sample the low mass end of the SFMS and in these regions their fit is extrapolated.

In the high mass end, I find no evidence of a turn-over in this work's data. This could be related to the relative lack of sources at higher masses in the data since the total area of the sky being sampled is $\simeq 0.2$ sq. degrees making it hard to probe the high

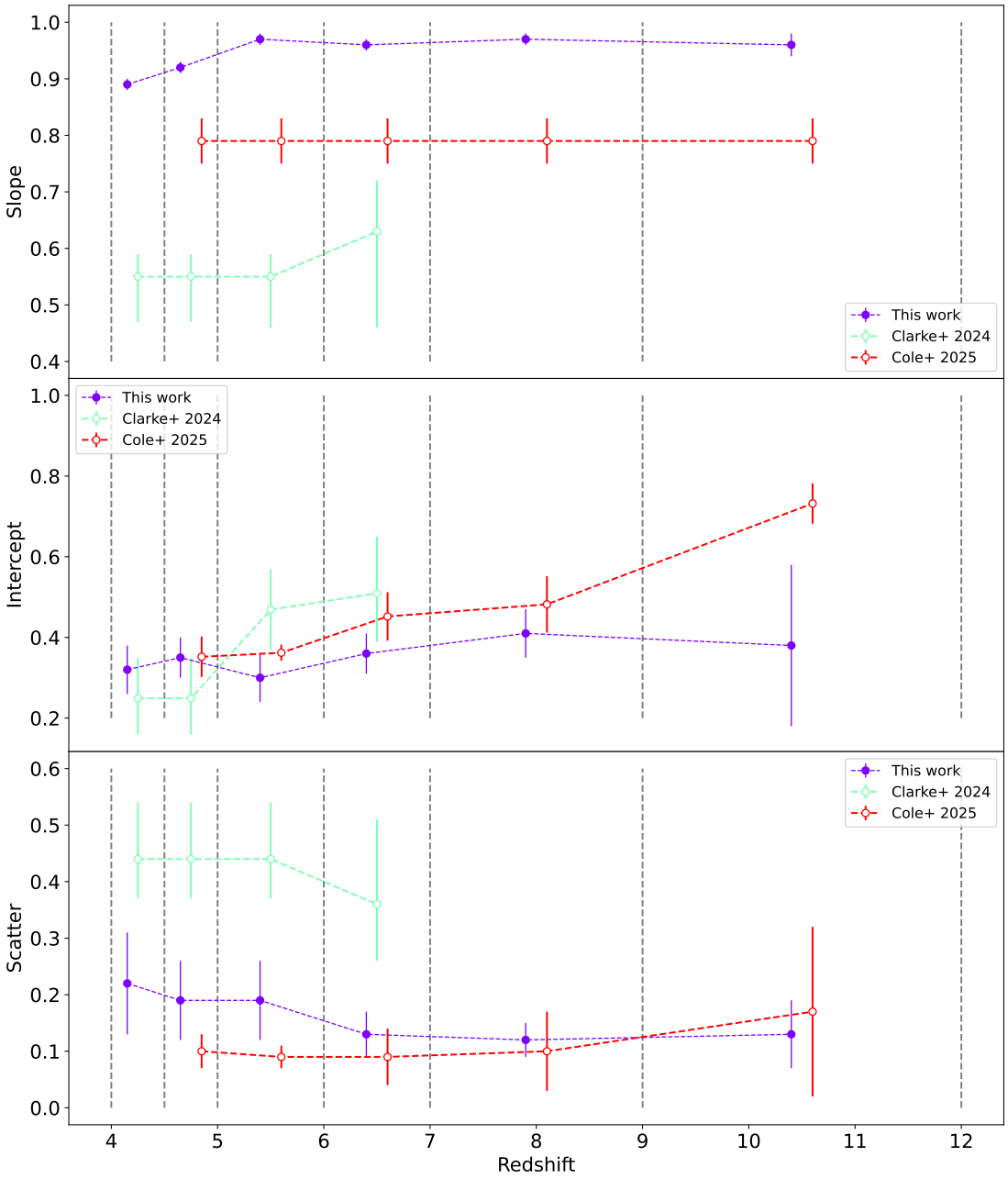

Figure 4.7: Comparisons between the derived parameters of the linear fit in this work with values from literature when the full sample of galaxies in all seven fields is used. The intercept is evaluated at the median mass of the sample – $10^{8.54}$ $M_{\odot}$.

Parameter	Derived value
a_0	0.9 ± 0.1
a_1	-0.11 ± 0.02
b_0	-8.1 ± 0.3
b_1	0.97 ± 0.06
b_2	0.003 ± 0.004

Table 4.2: Parameters of the derived fit of Equation 1.2, corresponding to Equation 10 from Popesso et al. (2023) and discussed in detail in Chapter 1.

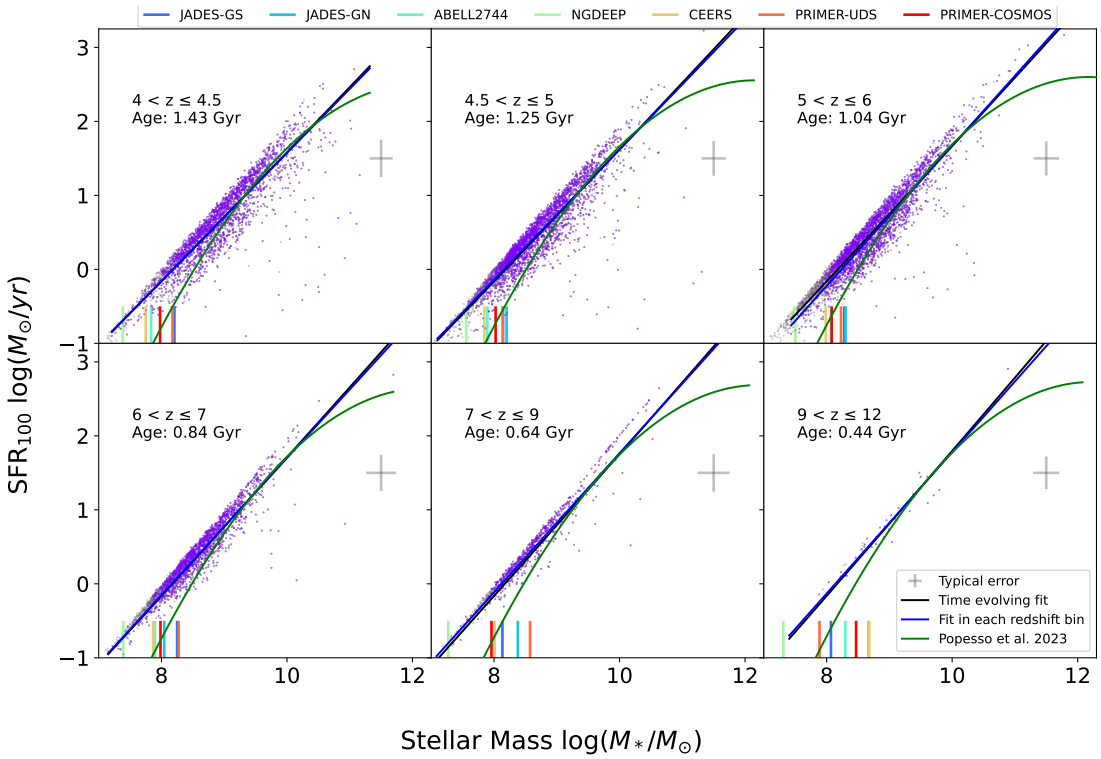

Figure 4.8: Time dependent SFMS fits, plotted at the middle point redshift for each bin. The fits in redshift bins from this work are also superimposed, as well as the SFMS from Popesso et al. (2023), for comparison. The small vertical lines represent the 90% mass completeness limits for each field and redshift bin.

mass end of the SFMS (as massive sources are in general rarer and larger observed areas are needed to sample them). Another possible explanation would be that the data analyzed by Popesso et al. (2023) is predominantly at lower redshifts where the turn-over is more prevalent (as discussed in Chapter 1). Their data does not go beyond $z \sim 6$ so in the higher redshift bins in this thesis it is, again, extrapolated.

4.4 Fitting the AGN

One important thing to consider is the possible effects of AGN on the stellar mass and SFR estimates, and therefore, on the inferred SFMS. In order to test this, the sample of known AGN was fit using three different assumptions:

- SED fitting was performed as for any other galaxy - no AGN component
- SED fitting included an AGN component with the parameters described in Table 3.2 and a thin disk.
- SED fitting included an AGN component with the parameters described in Table 3.2 but with ADAF.

The differences between these different methods were then evaluated and the comparison plots are shown in Fig. 4.9. In the figure I show the differences in the obtained $M_\star$ and SFR_{100} with all three methods. The percentage of sources for which the produced values for $M_\star$ and SFR are inconsistent between models are

shown in Table 4.3. The low amount of inconsistent sources between the thin disc model and the no AGN fits indicates that the fitting procedure tends to favor low AGN fraction models even when an AGN component with a thin disc is included. When the ADAF model is being fitted, the SED of more sources favor the inclusion of an AGN, marginally affecting the estimates of the physical properties.

The position in comparison to the SFMS for the AGN after deriving their properties in the described three different ways is shown in Figure 4.10. Almost all AGN stay on the SFMS within the uncertainties no matter how their SEDs are modelled, implying that the shape of the SFMS does not change significantly between these three different fitting approaches. The SFR and stellar mass of the AGN tend to differ similarly between models, as seen in Figure 4.9, moving them mainly along the SFMS (which in this work has a slope close to unity).

	$M_\star$	SFR
Thin disc - no AGN	25%	14%
Thin disc - ADAF	53%	40%
ADAF - no AGN	65%	40%

Table 4.3: The percentage of sources that were found to produce values inconsistent between different AGN models (or no AGN model) for the respective physical properties.

A limitation of this analysis, however, was imposed by the lack of emission lines in the AGN module used in CIGALE. In the rest-frame wavelengths covered by the data in this work, emission lines from a potential AGN would be expected (e.g. Balmer lines) but at this stage CIGALE produced only continuum emission for the AGN component. For this reason the data used in this thesis, alongside the models, were insufficient to constrain the fits of the AGN.

Due to this limitation, no meaningful conclusions can be drawn in effects of an AGN on the SFMS, nor can their position on an SFR-$M_\star$ be extensively studied. More robust datasets or more elaborate models are required to draw stronger conclusions.

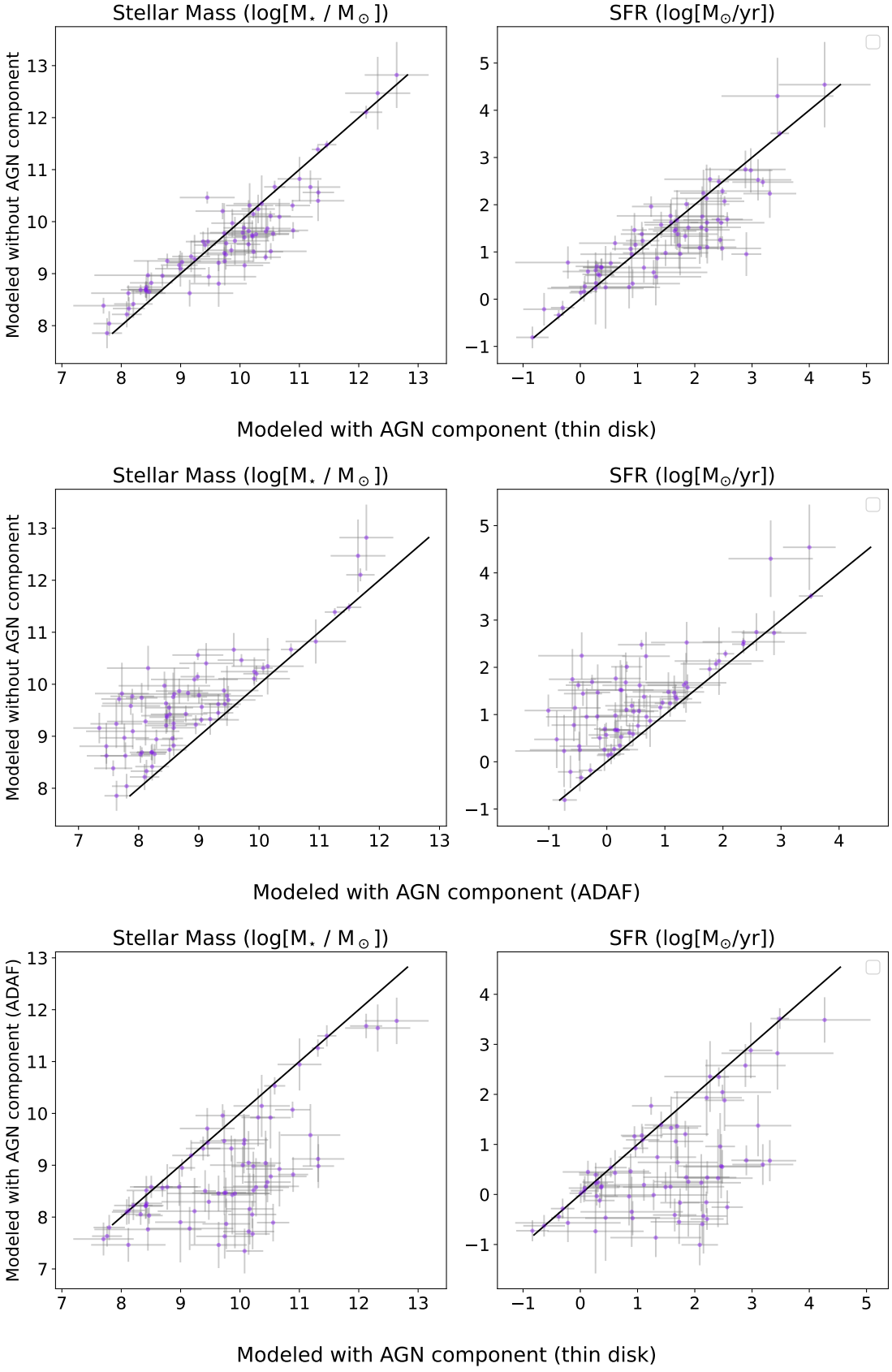

Figure 4.9: Comparisons of the inferred physical properties ($M_\star$ and SFR_{100}) between all three variations of the SED fitting for the AGN sample. The black solid line represents the 1:1 line.

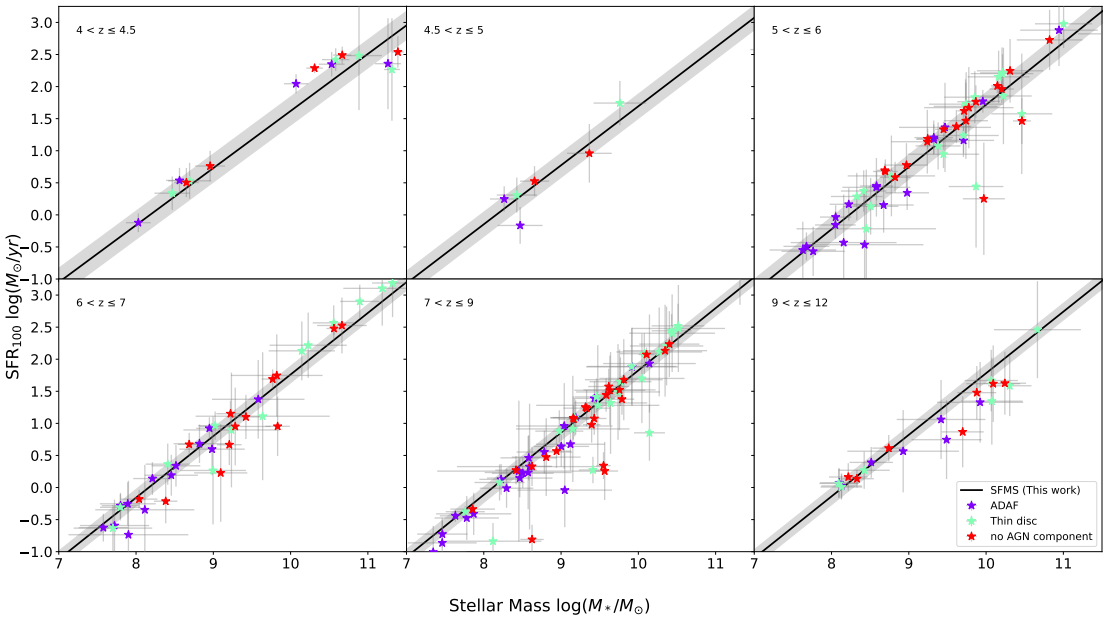

Figure 4.10: SFR-M$_\star$ plots with the sample of AGN. The properties of every AGN have been inferred by SED fitting in the three different ways described in the text. The SFMS obtained and described in Section 4.3.1 is over-plotted for comparison. The shaded region shows the scatter of the SFMS rather than the uncertainties on the fit.

Conclusions

In this thesis I set to examine the redshift evolution of the so-called Star Forming Main Sequence from JWST deep fields. I used the SED fitting technique to infer the physical properties of a large sample of galaxies in seven different fields from composite data from the JWST and HST. I used the SED fitting code CIGALE and examined a few key questions:

- How does the assumption on the form of the star formation history affect the derived physical parameters and therefore the obtained SFMS?
- How does the SFMS and its parameters evolve from $z = 4$ to $z = 12$?
- What can (and cannot) be concluded on the position of AGN on the SFR-$M_\star$ diagram from the available data?

As a result, I present fits of the SFMS using four different SFH models and their comparisons in the JADES-GS field, fits of the SFMS in each of the seven individual fields, and fits of the SFMS of the whole combined sample of 10 015 galaxies split in 6 redshift bins. I also present my estimates of the 90% mass completeness limits for each field and preliminary tests on the effects of AGN on the inferred physical properties through SED fitting.

I find that the star formation histories tested in this thesis have a significant impact only on the slope of the SFMS, where the non-parametric models produce larger slopes. For the two other parameters of the SFMS fit, i.e. the intercept and the scatter, the differences between the SFH assumptions are within the uncertainties on the fits.

The intercept and scatter of the SFMS showed consistency between the different studied redshift bins. The slope derived in this work slightly increases from $z \sim 4$ to $z \sim 5 - 6$, and then settles to a constant value around unity.

The study of the AGN in the sample showed inconclusive results in terms of the position of the AGN on the SFMS and requires more elaborate fitting procedures and robust datasets to reach meaningful conclusions.

This work can be greatly expanded and improved in the future in a few key ways:

- The fitting procedure for the SFMS can be greatly improved by implementing a Markov Chain Monte Carlo approach. Using this method, the uncertainties in the SFR and stellar mass can both be considered and the intrinsic scatter of the SFMS can be included as a free parameter of the fit. This approach is used in Santini et al. (2017), Clarke et al. (2024), and Cole et al. (2025) to name a few.

- The analysis can be expanded to lower redshifts to build a full and consistent picture of the SFMS evolution through cosmic time from local galaxies to the most distant observable sources with current technology.
- The study of the AGN and LRDs can be greatly expanded, e.g by considering other models when fitting their SEDs.

Bibliography

Begelman, Mitchell C. and Jason Dexter (July 2025). *Little Red Dots As Late-stage Quasi-stars*. ADS Bibcode: 2025arXiv250709085B. DOI: 10.48550/arXiv.2507.09085. URL: https://ui.adsabs.harvard.edu/abs/2025arXiv250709085B (visited on 09/11/2025).

Bergamini, Pietro et al. (July 2023). "The GLASS-JWST Early Release Science Program. III. Strong-lensing Model of Abell 2744 and Its Infalling Regions". In: *The Astrophysical Journal* 952. ADS Bibcode: 2023ApJ...952...84B, p. 84. ISSN: 0004-637X. DOI: 10.3847/1538-4357/acd643. URL: https://ui.adsabs.harvard.edu/abs/2023ApJ...952...84B (visited on 09/09/2025).

Boquien, M. et al. (Feb. 2019). "CIGALE: a python Code Investigating GALaxy Emission". In: *åp* 622. _eprint: 1811.03094, A103. DOI: 10.1051/0004-6361/201834156.

Brinchmann, J. et al. (July 2004). "The physical properties of star-forming galaxies in the low-redshift Universe". In: *Monthly Notices of the Royal Astronomical Society* 351. ADS Bibcode: 2004MNRAS.351.1151B, pp. 1151–1179. ISSN: 0035-8711. DOI: 10.1111/j.1365-2966.2004.07881.x. URL: https://ui.adsabs.harvard.edu/abs/2004MNRAS.351.1151B (visited on 09/08/2025).

Bruzual, G. and S. Charlot (Oct. 2003). "Stellar population synthesis at the resolution of 2003". In: *mnras* 344.4. _eprint: astro-ph/0309134, pp. 1000–1028. DOI: 10.1046/j.1365-8711.2003.06897.x.

Calzetti, Daniela et al. (Apr. 2000). "The Dust Content and Opacity of Actively Star-forming Galaxies". In: *apj* 533.2. _eprint: astro-ph/9911459, pp. 682–695. DOI: 10.1086/308692.

Carnall, A. C. et al. (Nov. 2018). "Inferring the star formation histories of massive quiescent galaxies with BAGPIPES: evidence for multiple quenching mechanisms". In: *Monthly Notices of the Royal Astronomical Society* 480. ADS Bibcode: 2018MNRAS.480.4379C, pp. 4379–4401. ISSN: 0035-8711. DOI: 10.1093/mnras/sty2169. URL: https://ui.adsabs.harvard.edu/abs/2018MNRAS.480.4379C (visited on 09/09/2025).

Carnall, A. C. et al. (Nov. 2019a). "The VANDELS survey: the star-formation histories of massive quiescent galaxies at 1.0 ¡ z ¡ 1.3". In: *Monthly Notices of the Royal Astronomical Society* 490. ADS Bibcode: 2019MNRAS.490..417C, pp. 417–439. ISSN: 0035-8711. DOI: 10.1093/mnras/stz2544. URL: https://ui.adsabs.harvard.edu/abs/2019MNRAS.490..417C (visited on 09/09/2025).

Carnall, Adam C. et al. (Mar. 2019b). "How to Measure Galaxy Star Formation Histories. I. Parametric Models". In: *The Astrophysical Journal* 873.1. Publisher: The American Astronomical Society, p. 44. DOI: 10.3847/1538-4357/ab04a2. URL: https://dx.doi.org/10.3847/1538-4357/ab04a2.

Carvajal-Bohorquez, C. et al. (July 2025). *Stochastic star formation activity of galaxies within the first billion years probed by JWST*. ADS Bibcode:

2025arXiv250713160C. DOI: 10.48550/arXiv.2507.13160. URL: https://ui.adsabs.harvard.edu/abs/2025arXiv250713160C (visited on 09/14/2025).

Casey, Caitlin M. (Oct. 2012). "Far-infrared spectral energy distribution fitting for galaxies near and far". In: *Monthly Notices of the Royal Astronomical Society* 425. ADS Bibcode: 2012MNRAS.425.3094C, pp. 3094–3103. ISSN: 0035-8711. DOI: 10.1111/j.1365-2966.2012.21455.x. URL: https://ui.adsabs.harvard.edu/abs/2012MNRAS.425.3094C (visited on 08/31/2025).

Chabrier, Gilles (July 2003). "Galactic Stellar and Substellar Initial Mass Function". In: *pasp* 115.809. _eprint: astro-ph/0304382, pp. 763–795. DOI: 10.1086/376392.

Charlot, Stéphane and S. Michael Fall (Aug. 2000). "A Simple Model for the Absorption of Starlight by Dust in Galaxies". In: *apj* 539.2. _eprint: astro-ph/0003128, pp. 718–731. DOI: 10.1086/309250.

Ciesla, L., D. Elbaz, and J. Fensch (Dec. 2017). "The SFR-M_\ensuremath* main sequence archetypal star-formation history and analytical models". In: *åp* 608. _eprint: 1706.08531, A41. DOI: 10.1051/0004-6361/201731036.

Clarke, Leonardo et al. (Dec. 2024). "The Star-forming Main Sequence in JADES and CEERS at z ¿ 1.4: Investigating the Burstiness of Star Formation". In: *Astrophysical Journal* 977.1. _eprint: 2406.05178, p. 133. DOI: 10.3847/1538-4357/ad8ba4.

Cole, Justin W. et al. (Feb. 2025). "CEERS: Increasing Scatter along the Star-forming Main Sequence Indicates Early Galaxies Form in Bursts". In: *Astrophysical Journal* 979.2. _eprint: 2312.10152, p. 193. DOI: 10.3847/1538-4357/ad9a6a.

Daddi, E. et al. (Nov. 2007). "Multiwavelength Study of Massive Galaxies at z\raisebox-0.5ex\textasciitilde2. II. Widespread Compton-thick Active Galactic Nuclei and the Concurrent Growth of Black Holes and Bulges". In: *apj* 670.1. _eprint: 0705.2832, pp. 173–189. DOI: 10.1086/521820.

Dale, Daniel A. et al. (Mar. 2014). "A Two-parameter Model for the Infrared/Submillimeter/Radio Spectral Energy Distributions of Galaxies and Active Galactic Nuclei". In: *The Astrophysical Journal* 784. ADS Bibcode: 2014ApJ...784...83D, p. 83. ISSN: 0004-637X. DOI: 10.1088/0004-637X/784/1/83. URL: https://ui.adsabs.harvard.edu/abs/2014ApJ...784...83D (visited on 08/31/2025).

Draine, B. T. et al. (July 2007). "Dust Masses, PAH Abundances, and Starlight Intensities in the SINGS Galaxy Sample". In: *The Astrophysical Journal* 663. ADS Bibcode: 2007ApJ...663..866D, pp. 866–894. ISSN: 0004-637X. DOI: 10.1086/518306. URL: https://ui.adsabs.harvard.edu/abs/2007ApJ...663..866D (visited on 08/31/2025).

Elbaz, D. et al. (June 2007). "The reversal of the star formation-density relation in the distant universe". In: *åp* 468.1. _eprint: astro-ph/0703653, pp. 33–48. DOI: 10.1051/0004-6361:20077525.

Eldridge, J. J. et al. (Nov. 2017). "Binary Population and Spectral Synthesis Version 2.1: Construction, Observational Verification, and New Results". In: *Publications of the Astron. Soc. of Australia* 34. _eprint: 1710.02154, e058. DOI: 10.1017/pasa.2017.51.

Eldridge, John J. and Elizabeth R. Stanway (Nov. 2009). "Spectral population synthesis including massive binaries". In: *mnras* 400.2. _eprint: https://academic.oup.com/mnras/article-pdf/400/2/1019/3344317/mnras0400-1019.pdf, pp. 1019–1028. ISSN: 0035-8711. DOI: 10.1111/j.1365-2966.2009.15514.x. URL: https://doi.org/10.1111/j.1365-2966.2009.15514.x.

Fitzpatrick, Edward L (n.d.). "AN ANALYSIS OF THE SHAPES OF ULTRAVIOLET EXTINCTION CURVES. I. THE 2175 Â BUMP". en. In: *ApJ. . .* ().

Fritz, J., A. Franceschini, and E. Hatziminaoglou (Mar. 2006). "Revisiting the infrared spectra of active galactic nuclei with a new torus emission model". In: *Monthly Notices of the Royal Astronomical Society* 366. ADS Bibcode: 2006MNRAS.366..767F, pp. 767–786. ISSN: 0035-8711. DOI: 10.1111/j.1365-2966.2006.09866.x. URL: https://ui.adsabs.harvard.edu/abs/2006MNRAS.366..767F (visited on 08/31/2025).

Gutkin, Julia, Stéphane Charlot, and Gustavo Bruzual (Oct. 2016). "Modelling the nebular emission from primeval to present-day star-forming galaxies". In: *mnras* 462.2. _eprint: 1607.06086, pp. 1757–1774. DOI: 10.1093/mnras/stw1716.

Harikane, Yuichi et al. (Dec. 2023). "A JWST/NIRSpec First Census of Broad-line AGNs at z = 4-7: Detection of 10 Faint AGNs with M BH 106-108 M and Their Host Galaxy Properties". In: *The Astrophysical Journal* 959. ADS Bibcode: 2023ApJ...959...39H, p. 39. ISSN: 0004-637X. DOI: 10.3847/1538-4357/ad029e. URL: https://ui.adsabs.harvard.edu/abs/2023ApJ...959...39H (visited on 09/11/2025).

Hubble, E. P. (Dec. 1925). "NGC 6822, a remote stellar system." In: *The Astrophysical Journal* 62. ADS Bibcode: 1925ApJ....62..409H, pp. 409–433. ISSN: 0004-637X. DOI: 10.1086/142943. URL: https://ui.adsabs.harvard.edu/abs/1925ApJ....62..409H (visited on 09/04/2025).

Inayoshi, Kohei (July 2025). "Little Red Dots as the Very First Activity of Black Hole Growth". In: *The Astrophysical Journal* 988. ADS Bibcode: 2025ApJ...988L..22I, p. L22. ISSN: 0004-637X. DOI: 10.3847/2041-8213/adea66. URL: https://ui.adsabs.harvard.edu/abs/2025ApJ...988L..22I (visited on 09/11/2025).

Inoue, Akio K. (Aug. 2011). "Rest-frame ultraviolet-to-optical spectral characteristics of extremely metal-poor and metal-free galaxies". In: *Monthly Notices of the Royal Astronomical Society* 415. ADS Bibcode: 2011MNRAS.415.2920I, pp. 2920–2931. ISSN: 0035-8711. DOI: 10.1111/j.1365-2966.2011.18906.x. URL: https://ui.adsabs.harvard.edu/abs/2011MNRAS.415.2920I (visited on 08/31/2025).

Iyer, Kartheik G. et al. (July 2019). "Nonparametric Star Formation History Reconstruction with Gaussian Processes. I. Counting Major Episodes of Star Formation". In: *The Astrophysical Journal* 879. ADS Bibcode: 2019ApJ...879..116I, p. 116. ISSN: 0004-637X. DOI: 10.3847/1538-4357/ab2052. URL: https://ui.adsabs.harvard.edu/abs/2019ApJ...879..116I (visited on 09/01/2025).

Iyer, Kartheik G. et al. (Feb. 2025). *The Spectral Energy Distributions of Galaxies*. arXiv:2502.17680 [astro-ph]. DOI: 10.48550/arXiv.2502.17680. URL: http://arxiv.org/abs/2502.17680 (visited on 08/24/2025).

Katsianis, Antonios et al. (2016). "The evolution of the star formation rate function and cosmic star formation rate density of galaxies at $z \sim 1-4$". In: Publisher: arXiv Version Number: 1. DOI: 10.48550/ARXIV.1610.03441. URL: https://arxiv.org/abs/1610.03441 (visited on 09/08/2025).

Kocevski, Dale et al. (Jan. 2025a). "JWST's Little Red Dots and the Rise of Obscured AGN at z¿5". In: vol. 245. ADS Bibcode: 2025AAS...24513907K, p. 139.07. URL: https://ui.adsabs.harvard.edu/abs/2025AAS...24513907K (visited on 09/11/2025).

Kocevski, Dale D. et al. (Sept. 2023). "Hidden Little Monsters: Spectroscopic Identification of Low-mass, Broad-line AGNs at z ¿ 5 with CEERS". In: *The As-*

trophysical Journal 954. ADS Bibcode: 2023ApJ...954L...4K, p. L4. ISSN: 0004-637X. DOI: 10.3847/2041-8213/ace5a0. URL: https://ui.adsabs.harvard.edu/abs/2023ApJ...954L...4K (visited on 09/11/2025).

Kocevski, Dale D. et al. (June 2025b). "The Rise of Faint, Red Active Galactic Nuclei at z ¿ 4: A Sample of Little Red Dots in the JWST Extragalactic Legacy Fields". In: *The Astrophysical Journal* 986. ADS Bibcode: 2025ApJ...986..126K, p. 126. ISSN: 0004-637X. DOI: 10.3847/1538-4357/adbc7d. URL: https://ui.adsabs.harvard.edu/abs/2025ApJ...986..126K (visited on 09/11/2025).

Kormendy, John and Luis C. Ho (Aug. 2013). "Coevolution (Or Not) of Supermassive Black Holes and Host Galaxies". In: *Annu. Rev. Astron. Astrophys.* 51.1. arXiv:1304.7762 [astro-ph], pp. 511–653. ISSN: 0066-4146, 1545-4282. DOI: 10.1146/annurev-astro-082708-101811. URL: http://arxiv.org/abs/1304.7762 (visited on 09/08/2025).

Kroupa, Pavel (Apr. 2001). "On the variation of the initial mass function". In: *mnras* 322.2. _eprint: astro-ph/0009005, pp. 231–246. DOI: 10.1046/j.1365-8711.2001.04022.x.

Labbe, I. et al. (May 2005). "IRAC Mid-Infrared Imaging of the Hubble Deep Field South: Star Formation Histories and Stellar Masses of Red Galaxies at z¿2". In: *ApJ* 624.2. arXiv:astro-ph/0504219, pp. L81–L84. ISSN: 0004-637X, 1538-4357. DOI: 10.1086/430700. URL: http://arxiv.org/abs/astro-ph/0504219 (visited on 09/03/2025).

Labbé, Ivo et al. (Apr. 2023). "A population of red candidate massive galaxies 600 Myr after the Big Bang". In: *Nature* 616. ADS Bibcode: 2023Natur.616..266L, pp. 266–269. ISSN: 0028-0836. DOI: 10.1038/s41586-023-05786-2. URL: https://ui.adsabs.harvard.edu/abs/2023Natur.616..266L (visited on 09/12/2025).

Leavitt, Henrietta S. and Edward C. Pickering (Mar. 1912). "Periods of 25 Variable Stars in the Small Magellanic Cloud." In: *Harvard College Observatory Circular* 173. ADS Bibcode: 1912HarCi.173....1L, pp. 1–3. URL: https://ui.adsabs.harvard.edu/abs/1912HarCi.173....1L (visited on 09/04/2025).

Lee, Nicholas et al. (Mar. 2015). "A Turnover in the Galaxy Main Sequence of Star Formation at M * ˜ 1010 M for Redshifts z ¡ 1.3". In: *The Astrophysical Journal* 801. ADS Bibcode: 2015ApJ...801...80L, p. 80. ISSN: 0004-637X. DOI: 10.1088/0004-637X/801/2/80. URL: https://ui.adsabs.harvard.edu/abs/2015ApJ...801...80L (visited on 09/09/2025).

Leja, Joel et al. (Apr. 2019). "How to Measure Galaxy Star Formation Histories. II. Nonparametric Models". In: *The Astrophysical Journal* 876.1. Publisher: The American Astronomical Society, p. 3. DOI: 10.3847/1538-4357/ab133c. URL: https://dx.doi.org/10.3847/1538-4357/ab133c.

Leja, Joel et al. (Sept. 2022). "A New Census of the 0.2 ¡ z ¡ 3.0 Universe. II. The Star-forming Sequence". In: *The Astrophysical Journal* 936. ADS Bibcode: 2022ApJ...936..165L, p. 165. ISSN: 0004-637X. DOI: 10.3847/1538-4357/ac887d. URL: https://ui.adsabs.harvard.edu/abs/2022ApJ...936..165L (visited on 09/16/2025).

Madau, Piero and Mark Dickinson (Aug. 2014). "Cosmic Star Formation History". In: *Annu. Rev. Astron. Astrophys.* 52.1. arXiv:1403.0007 [astro-ph], pp. 415–486. ISSN: 0066-4146, 1545-4282. DOI: 10.1146/annurev-astro-081811-125615. URL: http://arxiv.org/abs/1403.0007 (visited on 09/04/2025).

Magnelli, B. et al. (Jan. 2014). "The evolution of the dust temperatures of galaxies in the SFR-M plane up to z 2". In: *Astronomy and Astrophysics* 561. ADS Bibcode:

2014A&A...561A..86M, A86. ISSN: 0004-6361. DOI: 10.1051/0004-6361/201322217. URL: https://ui.adsabs.harvard.edu/abs/2014A&A...561A..86M (visited on 09/08/2025).

Maraston, Claudia (Sept. 2005). "Evolutionary population synthesis: models, analysis of the ingredients and application to high-z galaxies". In: *Monthly Notices of the Royal Astronomical Society* 362. ADS Bibcode: 2005MNRAS.362..799M, pp. 799–825. ISSN: 0035-8711. DOI: 10.1111/j.1365-2966.2005.09270.x. URL: https://ui.adsabs.harvard.edu/abs/2005MNRAS.362..799M (visited on 08/31/2025).

Matthee, Jorryt et al. (Mar. 2024). "Little Red Dots: An Abundant Population of Faint Active Galactic Nuclei at z 5 Revealed by the EIGER and FRESCO JWST Surveys". In: *The Astrophysical Journal* 963. ADS Bibcode: 2024ApJ...963..129M, p. 129. ISSN: 0004-637X. DOI: 10.3847/1538-4357/ad2345. URL: https://ui.adsabs.harvard.edu/abs/2024ApJ...963..129M (visited on 09/11/2025).

Merlin, E. et al. (Nov. 2024). "ASTRODEEP-JWST: NIRCam-HST multi-band photometry and redshifts for half a million sources in six extragalactic deep fields". In: *åp* 691. _eprint: 2409.00169, A240. DOI: 10.1051/0004-6361/202451409.

Mo, Houjun, Frank C. van den Bosch, and Simon White (May 2010). *Galaxy Formation and Evolution*. Publication Title: Galaxy Formation and Evolution ADS Bibcode: 2010gfe..book.....M. DOI: 10.1017/CBO9780511807244. URL: https://ui.adsabs.harvard.edu/abs/2010gfe..book.....M (visited on 09/15/2025).

Mountrichas, George (Apr. 2023). "The co-evolution of supermassive black holes and galaxies in luminous AGN over a wide range of redshift". en. In: *A&A* 672, A98. ISSN: 0004-6361, 1432-0746. DOI: 10.1051/0004-6361/202345924. URL: https://www.aanda.org/10.1051/0004-6361/202345924 (visited on 09/08/2025).

Nandal, Devesh and Abraham Loeb (July 2025). *Supermassive Stars Match the Spectral Signatures of JWST's Little Red Dots*. ADS Bibcode: 2025arXiv250712618N. DOI: 10.48550/arXiv.2507.12618. URL: https://ui.adsabs.harvard.edu/abs/2025arXiv250712618N (visited on 09/10/2025).

Narayan, Ramesh et al. (Jan. 1998). "Advection-dominated accretion model of Sagittarius A*: evidence for a black hole at the Galactic center." In: *The Astrophysical Journal* 492. ADS Bibcode: 1998ApJ...492..554N, pp. 554–568. ISSN: 0004-637X. DOI: 10.1086/305070. URL: https://ui.adsabs.harvard.edu/abs/1998ApJ...492..554N (visited on 09/09/2025).

Noeske, K. G. et al. (May 2007). "Star Formation in AEGIS Field Galaxies since z=1.1: The Dominance of Gradually Declining Star Formation, and the Main Sequence of Star-forming Galaxies". In: *apjl* 660.1. _eprint: astro-ph/0701924, pp. L43–L46. DOI: 10.1086/517926.

Noll, S. et al. (Dec. 2009). "Analysis of galaxy spectral energy distributions from far-UV to far-IR with CIGALE: studying a SINGS test sample". en. In: *A&A* 507.3, pp. 1793–1813. ISSN: 0004-6361, 1432-0746. DOI: 10.1051/0004-6361/200912497. URL: http://www.aanda.org/10.1051/0004-6361/200912497 (visited on 08/31/2025).

Peng, Y., R. Maiolino, and R. Cochrane (May 2015). "Strangulation as the primary mechanism for shutting down star formation in galaxies". In: *Nature* 521. ADS Bibcode: 2015Natur.521..192P, pp. 192–195. ISSN: 0028-0836. DOI: 10.1038/na

ture14439. URL: https://ui.adsabs.harvard.edu/abs/2015Natur.521..192P (visited on 09/15/2025).
Plat, A. et al. (Nov. 2019). "Constraints on the production and escape of ionizing radiation from the emission-line spectra of metal-poor star-forming galaxies". In: *mnras* 490.1. _eprint: 1909.07386, pp. 978–1009. DOI: 10.1093/mnras/stz2616.
Popesso, P. et al. (Feb. 2023). "The main sequence of star-forming galaxies across cosmic times". In: *mnras* 519.1. _eprint: 2203.10487, pp. 1526–1544. DOI: 10.1093/mnras/stac3214.
Pozzetti, L. et al. (Nov. 2010). "zCOSMOS - 10k-bright spectroscopic sample. The bimodality in the galaxy stellar mass function: exploring its evolution with redshift". In: *åp* 523. _eprint: 0907.5416, A13. DOI: 10.1051/0004-6361/200913020.
Rieke, Marcia J. et al. (Feb. 2023). "Performance of NIRCam on JWST in Flight". In: *Publications of the Astronomical Society of the Pacific* 135. ADS Bibcode: 2023PASP..135b8001R, p. 028001. ISSN: 0004-6280. DOI: 10.1088/1538-3873/acac53. URL: https://ui.adsabs.harvard.edu/abs/2023PASP..135b8001R (visited on 09/15/2025).
Rodighiero, G. et al. (Oct. 2011). "The Lesser Role of Starbursts in Star Formation at z = 2". In: *The Astrophysical Journal* 739. ADS Bibcode: 2011ApJ...739L..40R, p. L40. ISSN: 0004-637X. DOI: 10.1088/2041-8205/739/2/L40. URL: https://ui.adsabs.harvard.edu/abs/2011ApJ...739L..40R (visited on 09/08/2025).
Rodighiero, G. et al. (Feb. 2015). "Relationship between Star Formation Rate and Black Hole Accretion At Z = 2: the Different Contributions in Quiescent, Normal, and Starburst Galaxies". In: *The Astrophysical Journal* 800. ADS Bibcode: 2015ApJ...800L..10R, p. L10. ISSN: 0004-637X. DOI: 10.1088/2041-8205/800/1/L10. URL: https://ui.adsabs.harvard.edu/abs/2015ApJ...800L..10R (visited on 09/08/2025).
Salim, Samir, Médéric Boquien, and Janice C. Lee (May 2018). "Dust Attenuation Curves in the Local Universe: Demographics and New Laws for Star-forming Galaxies and High-redshift Analogs". In: *apj* 859.1. _eprint: 1804.05850, p. 11. DOI: 10.3847/1538-4357/aabf3c.
Salpeter, Edwin E. (Jan. 1955). "The Luminosity Function and Stellar Evolution." In: *apj* 121, p. 161. DOI: 10.1086/145971.
Sánchez, S. F. et al. (Oct. 2022). "SDSS-IV MaNGA: pyPipe3D Analysis Release for 10,000 Galaxies". In: *apjs* 262.2. _eprint: 2206.07062, p. 36. DOI: 10.3847/1538-4365/ac7b8f.
Santini, Paola et al. (Sept. 2017). "The Star Formation Main Sequence in the Hubble Space Telescope Frontier Fields". In: *apj* 847.1. _eprint: 1706.07059, p. 76. DOI: 10.3847/1538-4357/aa8874.
Schreiber, C. et al. (Mar. 2017). "The ALMA Redshift 4 Survey (AR4S). I. The massive end of the z = 4 main sequence of galaxies". In: *åp* 599. _eprint: 1606.06252, A134. DOI: 10.1051/0004-6361/201629155.
Shapley, H. (Dec. 1918). "Studies based on the colors and magnitudes in stellar clusters. VIII. The luminosities and distances of 139 Cepheid variables." In: *The Astrophysical Journal* 48. ADS Bibcode: 1918ApJ....48..279S, pp. 279–294. ISSN: 0004-637X. DOI: 10.1086/142435. URL: https://ui.adsabs.harvard.edu/abs/1918ApJ....48..279S (visited on 09/04/2025).
Shivaei, Irene et al. (Dec. 2015). "The MOSDEF Survey: Dissecting the Star Formation Rate versus Stellar Mass Relation Using H and H Emission Lines at z 2". In: *The Astrophysical Journal* 815. ADS Bibcode: 2015ApJ...815...98S, p. 98.

ISSN: 0004-637X. DOI: 10.1088/0004-637X/815/2/98. URL: https://ui.adsabs.harvard.edu/abs/2015ApJ...815...98S (visited on 09/03/2025).
Skilling, John (Dec. 2006). "Nested sampling for general Bayesian computation". In: *Bayesian Analysis* 1.4. Publisher: International Society for Bayesian Analysis, pp. 833–859. ISSN: 1936-0975, 1931-6690. DOI: 10.1214/06-BA127. URL: https://projecteuclid.org/journals/bayesian-analysis/volume-1/issue-4/Nested-sampling-for-general-Bayesian-computation/10.1214/06-BA127.full (visited on 09/09/2025).
Speagle, J. S. et al. (Oct. 2014). "A Highly Consistent Framework for the Evolution of the Star-Forming "Main Sequence" from z ˜ 0-6". In: *The Astrophysical Journal Supplement Series* 214. ADS Bibcode: 2014ApJS..214...15S, p. 15. ISSN: 0067-0049. DOI: 10.1088/0067-0049/214/2/15. URL: https://ui.adsabs.harvard.edu/abs/2014ApJS..214...15S (visited on 09/03/2025).
Stalevski, Marko et al. (May 2016). "The dust covering factor in active galactic nuclei". In: *Monthly Notices of the Royal Astronomical Society* 458. ADS Bibcode: 2016MNRAS.458.2288S, pp. 2288–2302. ISSN: 0035-8711. DOI: 10.1093/mnras/stw444. URL: https://ui.adsabs.harvard.edu/abs/2016MNRAS.458.2288S (visited on 08/31/2025).
Stanway, E. R. and J. J. Eldridge (Sept. 2018). "Re-evaluating old stellar populations". In: *mnras* 479.1. _eprint: 1805.08784, pp. 75–93. DOI: 10.1093/mnras/sty1353.
Tomczak, Adam R. et al. (Feb. 2016). "The SFR-M* Relation and Empirical Star-Formation Histories from ZFOURGE* at 0.5 ¡ z ¡ 4". In: *The Astrophysical Journal* 817. ADS Bibcode: 2016ApJ...817..118T, p. 118. ISSN: 0004-637X. DOI: 10.3847/0004-637X/817/2/118. URL: https://ui.adsabs.harvard.edu/abs/2016ApJ...817..118T (visited on 09/09/2025).
Topping, Michael W. et al. (Sept. 2021). "The MOSDEF survey: the mass-metallicity relationship and the existence of the FMR at z 1.5". In: *Monthly Notices of the Royal Astronomical Society* 506. ADS Bibcode: 2021MNRAS.506.1237T, pp. 1237–1249. ISSN: 0035-8711. DOI: 10.1093/mnras/stab1793. URL: https://ui.adsabs.harvard.edu/abs/2021MNRAS.506.1237T (visited on 09/03/2025).
Werner, M. W. et al. (Sept. 2004). "The Spitzer Space Telescope Mission". In: *The Astrophysical Journal Supplement Series* 154. ADS Bibcode: 2004ApJS..154....1W, pp. 1–9. ISSN: 0067-0049. DOI: 10.1086/422992. URL: https://ui.adsabs.harvard.edu/abs/2004ApJS..154....1W (visited on 09/15/2025).
Whitaker, Katherine E. et al. (Nov. 2014). "Constraining the Low-mass Slope of the Star Formation Sequence at 0.5 ¡ z ¡ 2.5". In: *The Astrophysical Journal* 795. ADS Bibcode: 2014ApJ...795..104W, p. 104. ISSN: 0004-637X. DOI: 10.1088/0004-637X/795/2/104. URL: https://ui.adsabs.harvard.edu/abs/2014ApJ...795..104W (visited on 09/08/2025).
Williams, Rik J. et al. (Feb. 2009). "Detection of Quiescent Galaxies in a Bicolor Sequence from Z = 0-2". In: *The Astrophysical Journal* 691. ADS Bibcode: 2009ApJ...691.1879W, pp. 1879–1895. ISSN: 0004-637X. DOI: 10.1088/0004-637X/691/2/1879. URL: https://ui.adsabs.harvard.edu/abs/2009ApJ...691.1879W (visited on 09/03/2025).
Wuyts, Stijn et al. (Jan. 2007). "What do we learn from IRAC observations of galaxies at 2 ¡ z ¡ 3.5?" In: *ApJ* 655.1. arXiv:astro-ph/0609548, pp. 51–65. ISSN:

0004-637X, 1538-4357. DOI: 10.1086/509708. URL: http://arxiv.org/abs/astro-ph/0609548 (visited on 09/03/2025).

Acknowledgments

Bozhidara Stoyanova acknowledges support through an Erasmus Mundus Joint Master (EMJM) scholarship Co-funded by the European Union in the framework of the Erasmus+, Erasmus Mundus Joint Master in Astrophysics and Space Science – MASS. Views and opinions expressed are however those of the author(s) only and do not necessarily reflect those of the European Union or granting authority European Education and Culture Executive Agency (EACEA). Neither the European Union nor the granting authority can be held responsible for them.

I also am very thankful to my amazing supervisors – Dr. Paola Santini, Prof. Médéric Boquien, and Prof. Francesco Tombesi – that patiently answered every question, gave very insightful critiques and comments, and genuinely taught me a lot.

A special "Thank you!" is also in order for Lorenzo Napolitano for letting me use his desk and broken chair for three full months (the scarcest resources in all of Rome)! I am also very grateful for the whole extragalactic group at the INAF Osservatorio Astronomico di Roma for all the coffees, the interesting conversations, and the generally welcoming attitude that made all Cotral rides to the observatory worth it.

One of the most challenging things I experienced in these past two years was the intense and often confusing bureaucracy, so I would like to, again, thank my supervisors for bearing with me even when things were confusing, and especially to Dr. Adalia Caroli and the project office for being always so quick to respond and very helpful.

I am very thankful for all my friends and family at home for always making sure I have an anchor and a real home (not just a house) to come back to.

But maybe most of all I want to acknowledge my dear friends in MASS that made this experience worth every second. For being incredible study partners, fun company and just an overall bunch of incredible individuals. I want to thank especially Jerónimo Calderón Gómez, Pablo Drake Hernández, Daisy Bergin, Thara Rubí Caba Pineda, Natalia Alvarez Baena, Francesca Borġ, Shoaib Shamsi and indeed everyone in the whole cohort. Thank you guys, I will miss you a whole lot!

Appendix A

Different SFH modules in the JADES-GS field

Plots for the SFR-M$_\star$ diagrams of the JADES-GS field with the other three SFH modules, not shown directly in the main text. Plots include the respective SFMS fits and comparisons with literature.

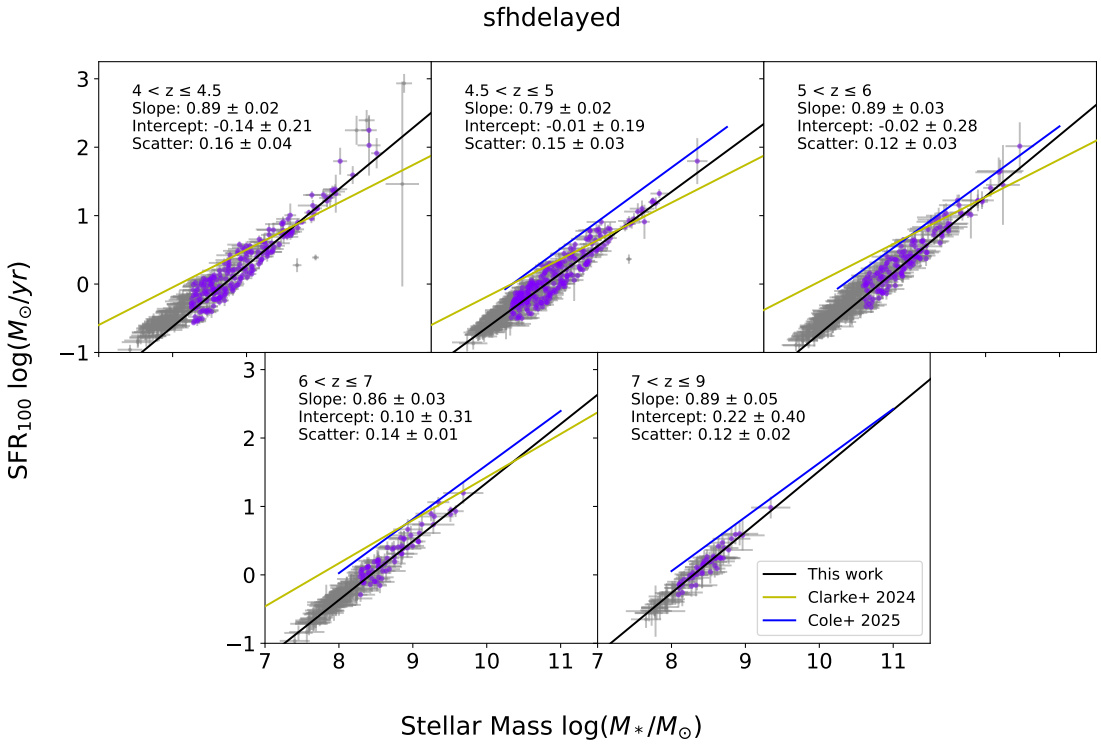

Figure A.1: As Fig. 4.1 but for `sfhdelayed` SFH model.

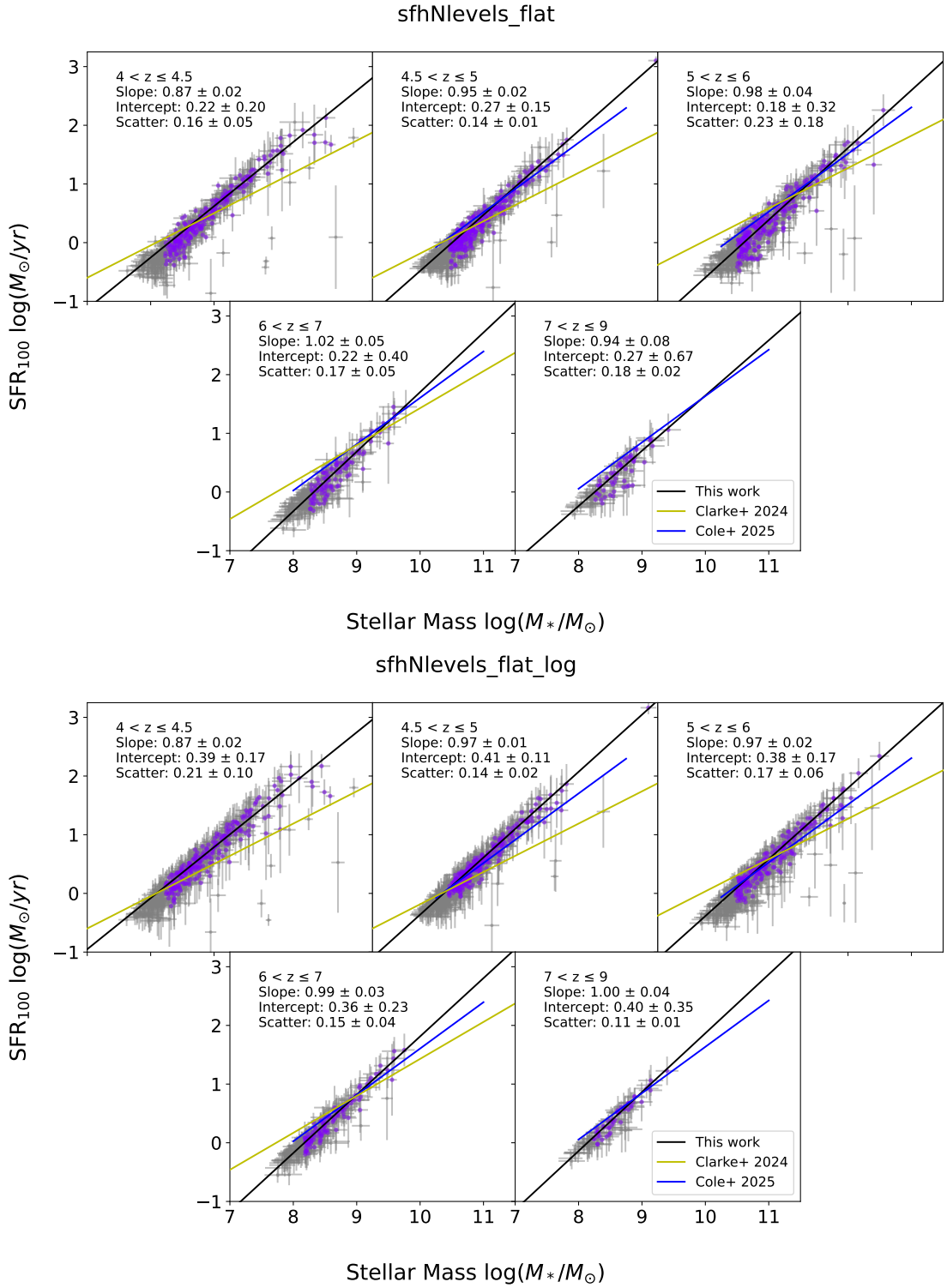

Figure A.2: As Fig. 4.1 but for `sfhNlevels_flat` SFH (*top*) and `sfhNlevels_flat_log` SFH (*bottom*).

Appendix B

Direct comparisons between SFR and $M_\star$ with different SFH

Plots of direct comparisons between the stellar masses and SFRs determined in the JADES-GS field with the different SFH modules. Plots comparing all combinations in all redshift bins considered are shown in the following Figures B.1, B.2, B.3, B.4, and B.5.

In these plots it is shown that the `sfhdelayed` module produces systematically lower SFR_{100} estimates, explaining the marginally lower intercept seen in the SFMS derived with this module, shown in Section 4.1, although those differences are not significant enough to produce differences larger than the uncertainties.

The two non-parametric models are shown to be very consistent with each other in Figure B.5, although for the estimates of the SFR the model with logarithmic binning in time gives slightly lower values (again, mostly within the uncertainties).

For the other comparisons between a non-parametric and a parametric model (as in Figures B.2, B.3, and B.4), the same effect as described in Section 4.1 and shown in Figure 4.3 is noticeable, albeit negligibly small in some cases (as in Figure B.4).

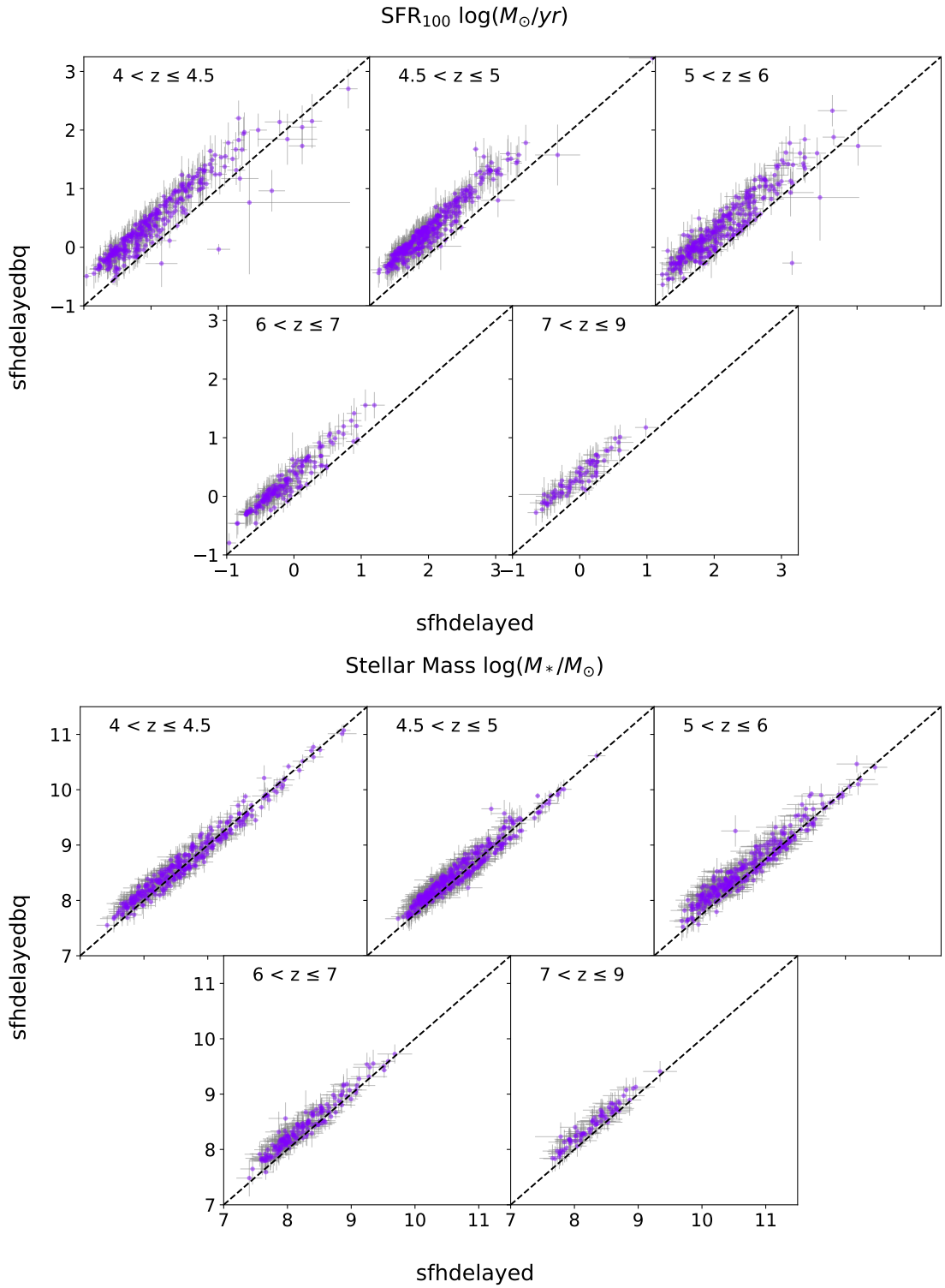

Figure B.1: As in Figures 4.3 and 4.4 for the `sfhdelayed` and `sfhdelayedbq` SFH modules.

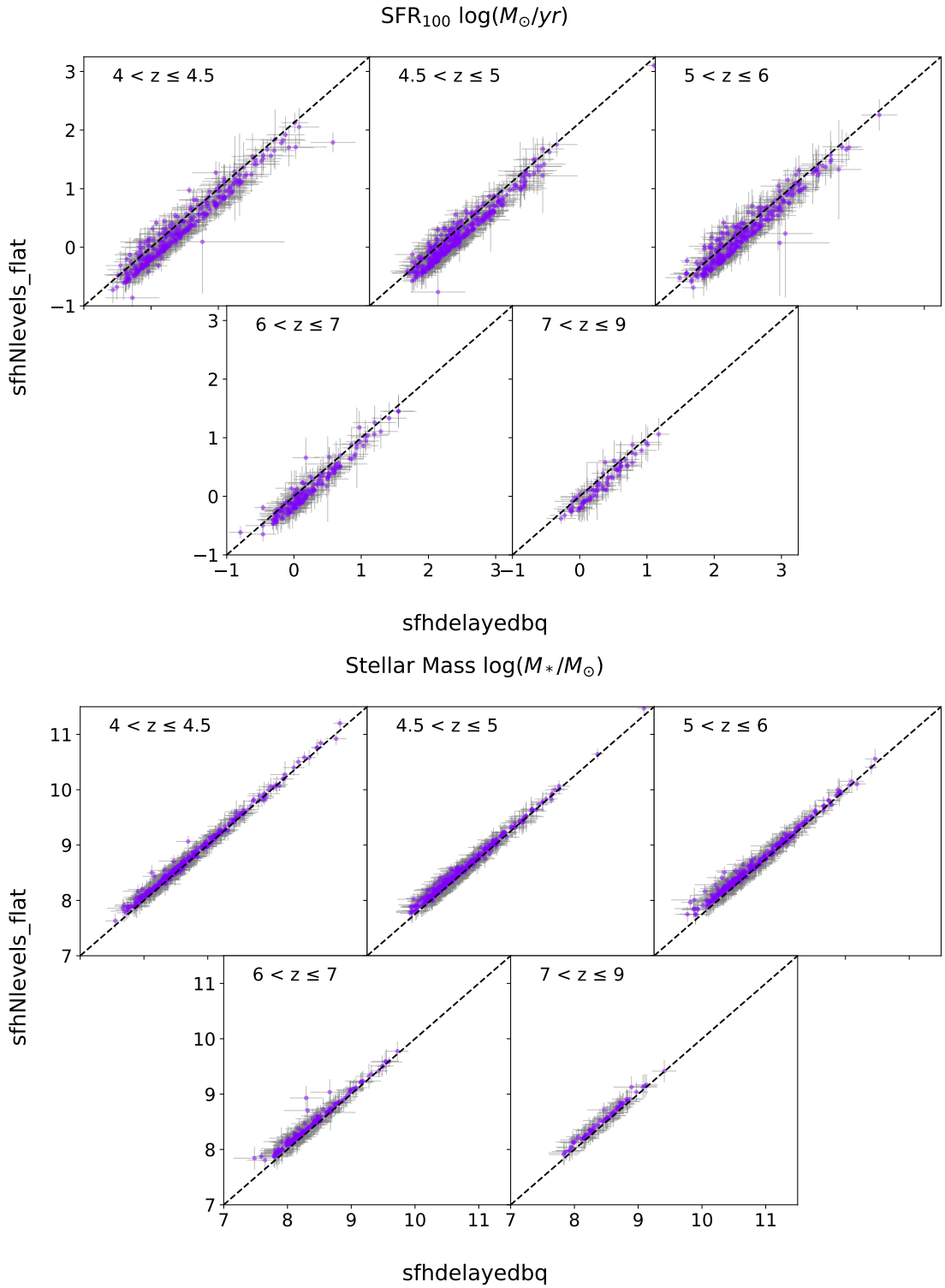

Figure B.2: As in Figures 4.3 and 4.4 for the `sfhNlevels_flat` and `sfhdelayedbq` SFH modules.

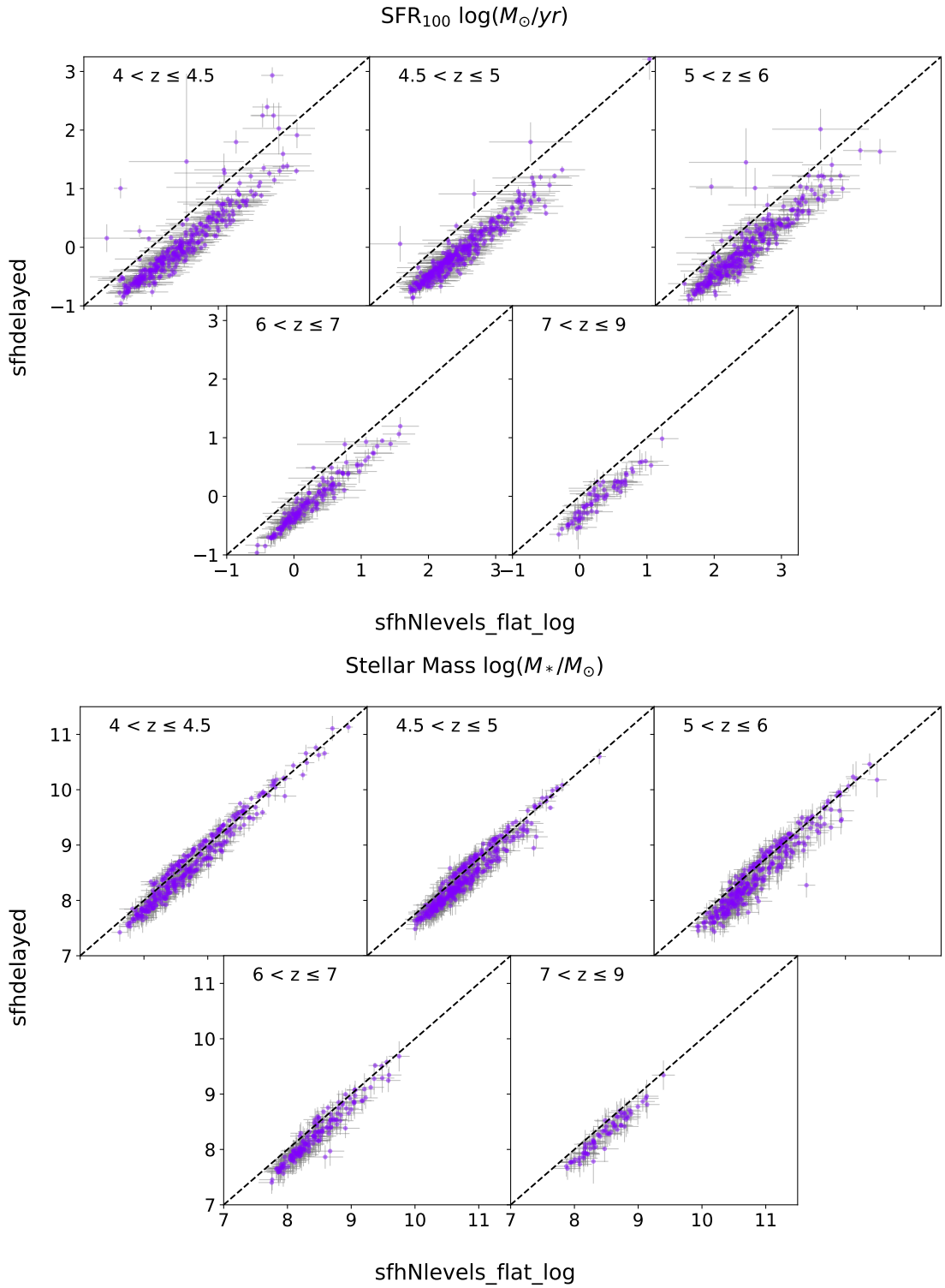

Figure B.3: As in Figures 4.3 and 4.4 for the `sfhNlevels_flat_log` and `sfhdelayed` SFH modules.

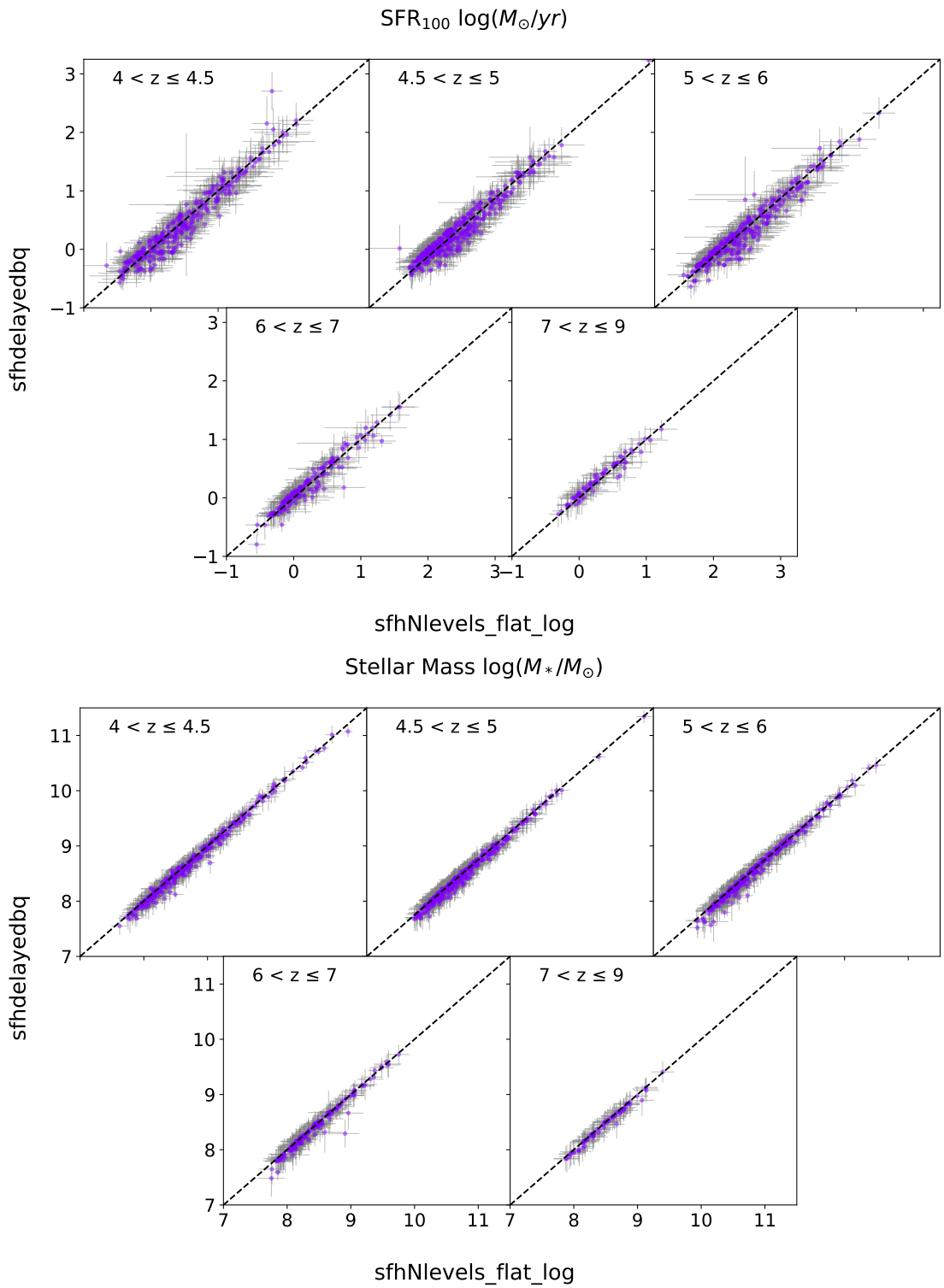

Figure B.4: As in Figures 4.3 and 4.4 for the `sfhNlevels_flat_log` and `sfhdelayedbq` SFH modules.

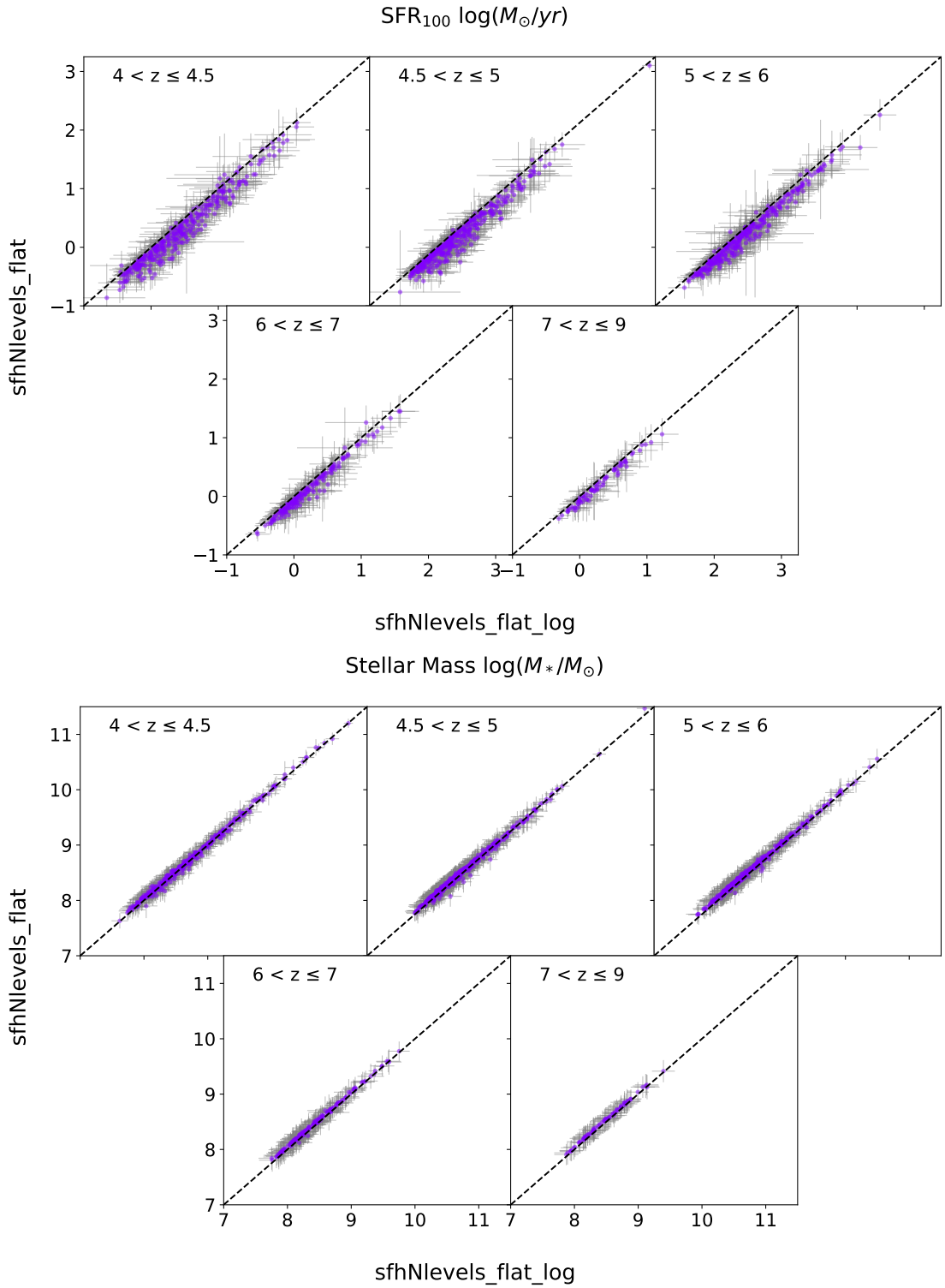

Figure B.5: As in Figures 4.3 and 4.4 for the `sfhNlevels_flat_log` and `sfhNlevels_flat` SFH modules.

Appendix C

The SFMS in each field

SFR-M$_\star$ plots for each field with the `sfhdelayedbq` SFH module with the respective SFMS fits.

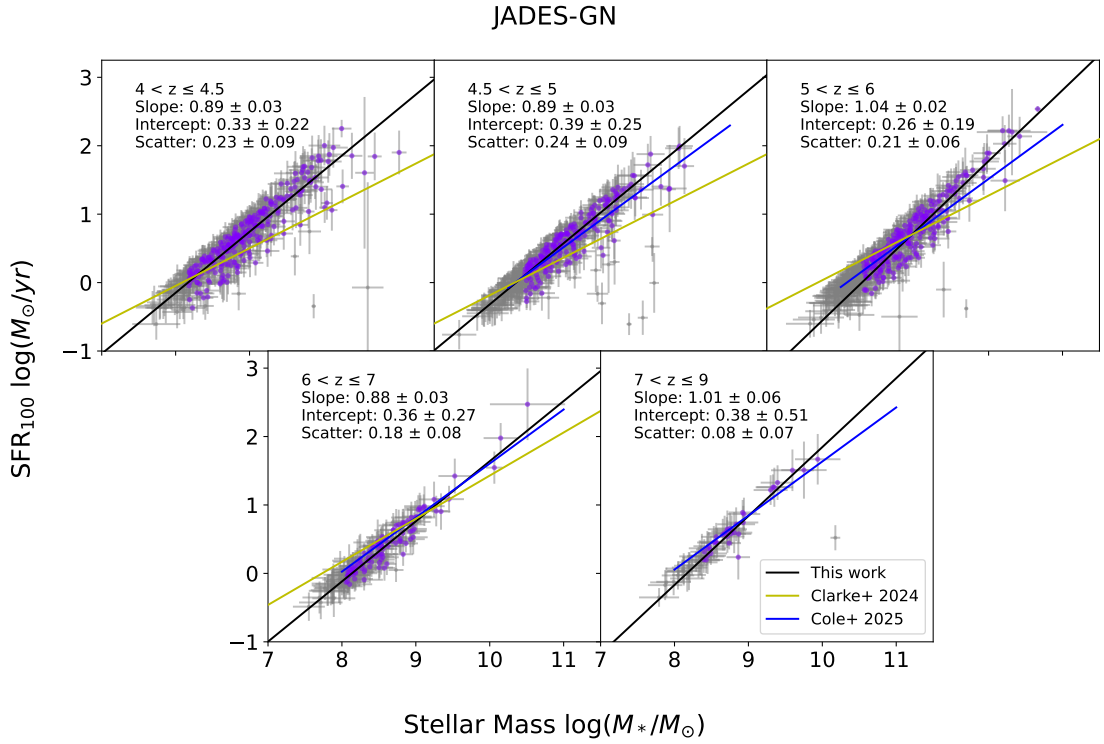

Figure C.1: SFR-M$_\star$ diagram obtained from fitting the sources with the `sfhdelayedbq` SFH in the JADES-GN field. The diagrams show the derived SFMS in 5 redshift bins spanning from $z = 4$ to $z = 10$. The purple points show the points used for the SFMS fitting, while the gray points show sources that were either below the mass completeness limit or were rejected during the sigma clipping procedure. The black solid line is my fit to the data. The two color solid lines are comparisons with the literature - Cole et al. (2025) (blue) and Clarke et al. (2024) (yellow). The intercept is evaluated at the median mass of the sample – $10^{8.54}$ M$_\odot$.

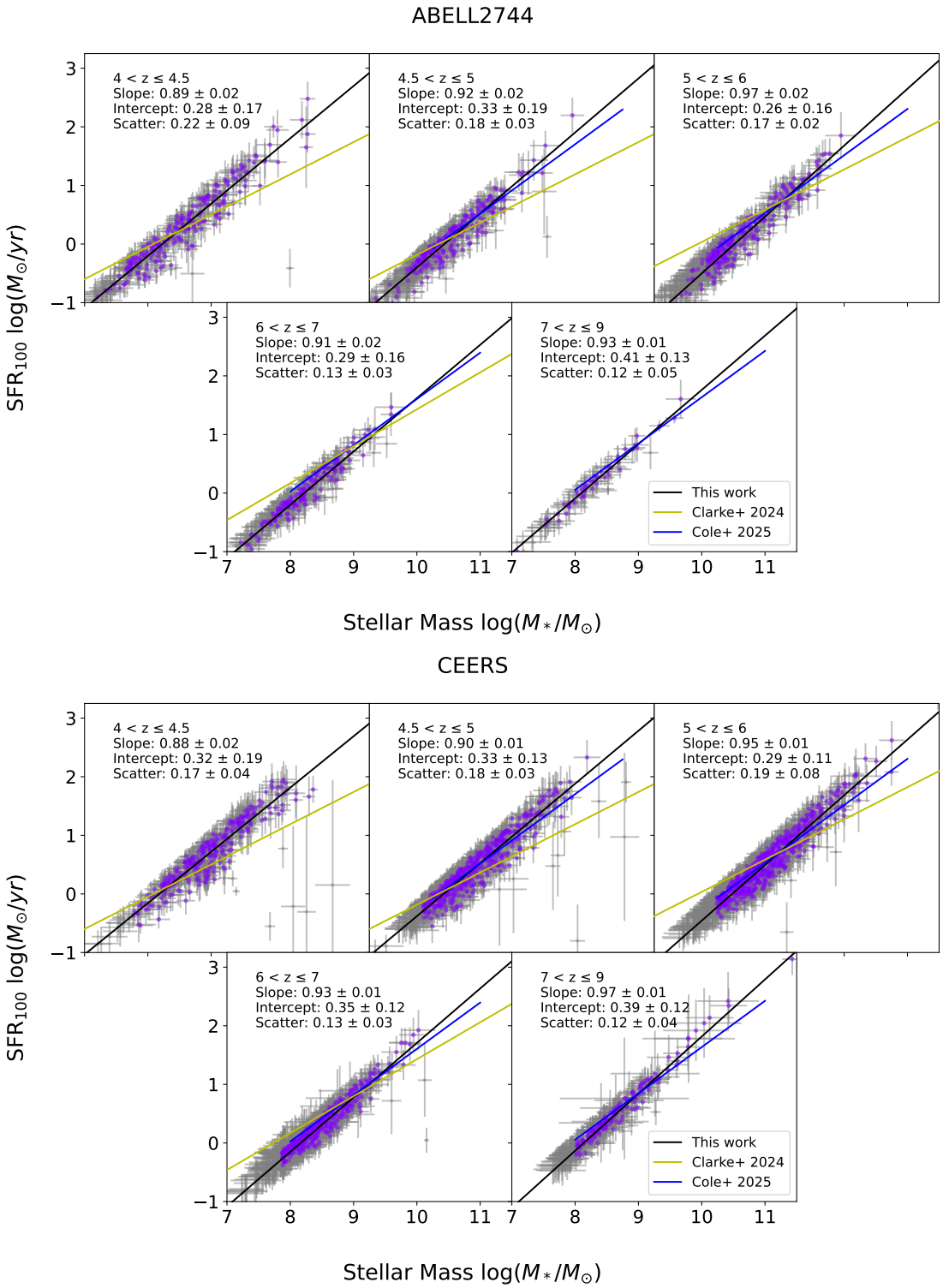

Figure C.2: Same as in Figure C.1 but for the Abell 2744 field (*top*) and the CEERS field (*bottom*).

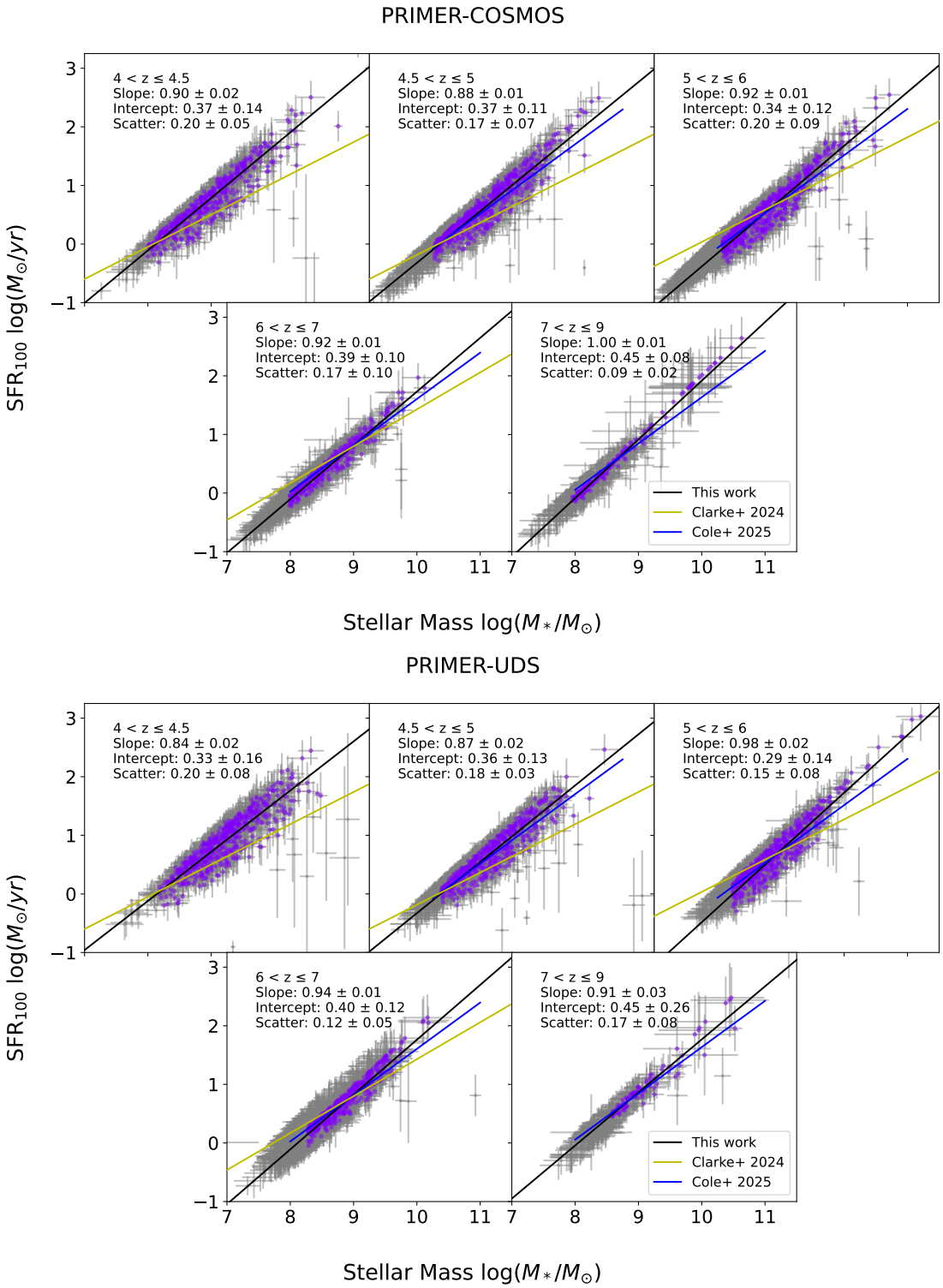

Figure C.3: As Figure C.1 but for *Top:* PRIMER-COSMOS. *Bottom:* PRIMER-UDS.

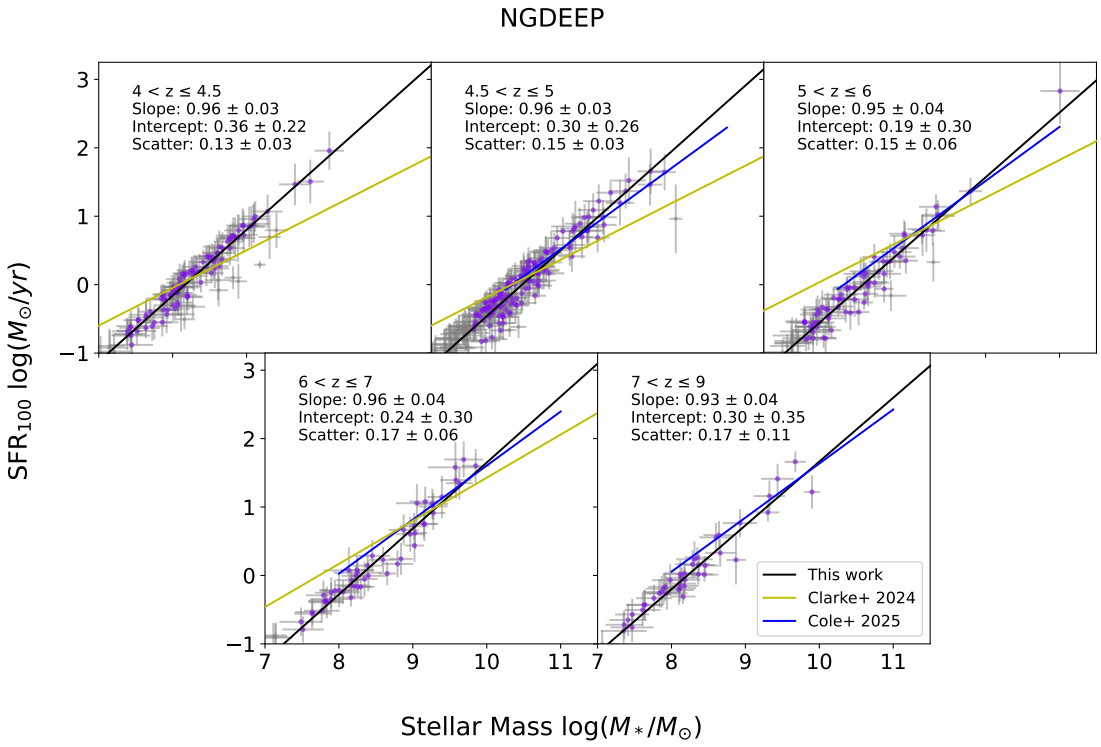

Figure C.4: As Figure C.1 but for the NGDEEP field.